Optical Coherence Tomography and Nanoparticles with Concave Surfaces: from the following of nanoparticles growth kinetics to their use as contrast agent

Yenisey del Rocío

Ponce de León Villanueva

July, 2014

Optical Coherence Tomography and Nanoparticles with Concave Surfaces: From the following of nanoparticles growth kinetics to their use as contrast agent

By

Yenisey del Rocío Ponce de León Villanueva

Thesis

Submitted in partial fulfillment of the requirements for the degree of Doctor in Science (optics) at the Centro de Investigaciones en Óptica, A.C.

Advisors:

Dr. Juan Luis Pichardo Molina
Dr. Noé Alcalá Ochoa

León, Gto., México July, 2014

Tomografía de Coherencia Óptica y Nanopartículas con Superficies Cóncavas: del seguimiento de la cinética de crecimiento de nanopartículas a su uso como agente de contraste

Tesis que presenta

Yenisey del Rocío Ponce de León Villanueva

Como requerimiento parcial para la obtención del grado de Doctor en Ciencias (Óptica) en el Centro de Investigaciones en Óptica, A.C.

Asesores:

Dr. Juan Luis Pichardo Molina

Dr. Noé Alcalá Ochoa

León, Gto., México Julio, 2014

To my love JCGG

and my family

Acknowledgements

I would like to thank all the persons that supported me in some way to get my doctoral degree. To my advisors, Dr. Juan Luis Pichardo Molina and Dr. Noé Alcalá Ochoa, for their guidance and patience during this period, for the knowledge and experience shared that helped me to be former as a researcher. To Martín Olmos and Enrique Noé for the support in the laboratories and their friendship. To my partners and friends with whom I shared experiences and work time, Laura Aparicio, Gilberto Moreno, Pablo Cardoso, Jorge Alberto López,. To Dr. Mario Rodríguez and Dra. Rosario Galindo for their valuable help. To my friends, who have stayed by my side in difficult moments equally as in the good times, Araceli, Citlalli, Xiomara, Mariana, Enif and Javier. To all the members of the GPOM group. To my first advisor in my way of learning optics, Dr. Mauricio Ortiz, and my master degree advisor José Luis Maldonado, from whom I learned too much and contributed to get my final goal of getting my doctoral degree. To my evaluation committee Dr. Abundio Dávila, Dr. Jorge Castro, and Dr. Oracio Barbosa for their valuable comments which allow me to improve this thesis. To my family for their unconditional support; and to my little family JCGG for his support, patience, company and for the years shared.

Abstract

The Optical Coherence Tomography (OCT) technique is an imaging modality that performs tomographic images with high resolutions (1-15μm) and high depth penetration capacity (12mm). It uses NIR light and is called the optical analogous of ultrasound. Its potential is based on the fact that is able to imaging transparent and highly scattering tissue samples, deeper and with better resolution than other techniques. However, tissues are optically inhomogeneous and the resulting scattering limits resolution and imaging depth; mainly in non transparent media.

During the last decade, nanoparticles (NPs) have had a great impact on applications in different areas; one of them in the biomedical field as contrast agents, markers, sensors, etc. Nevertheless, most of the time the syntheses are not ideal, since they do not present high yield production and monodispersivity. In order to get a good synthesis, an understanding of the process that governs the NP growth is needed.

In this thesis an analysis of the growth kinetics of concave nanocubes by means of the Optical Coherence Tomography (OCT) technique is reported. In order to corroborate the viability of the OCT technique, UV-Vis spectroscopy and dynamic light scattering (DLS) experiments were also carried out. The results of the three techniques are very similar, confirming that OCT is a feasible technique to follow the NP growth kinetics. Furthermore, OCT shows the advantage over the UV-Vis spectroscopy technique that OCT is able to detect low concentrations of NPs, making it able to follow the synthesis since the beginning; and the monitoring is not affected by small variations in concentration. Additionally, the combination of these techniques allows getting complementary information of the synthesis without the need of expensive and sophisticated equipment. Moreover, to our knowledge, this is the first time that OCT is used to follow the NP growth kinetics.

As was mentioned above, NPs are commonly used as contrast agent. In this thesis, is also reported the use of branched NPs as contrast agent in OCT imaging. Branched NPs, spheres, and rods were analyzed in water to show that branched NPs generate better contrast, even when they

are diluted. Later, branched NPs were introduced in a tissue phantom, from which the contrast enhancement was calculated respect to an area of the tissue phantom without NPs. The results show that even when the mean peak of the plasmon band of NPs (750 nm) is far away of the central wavelength of the OCT system (1325 nm), branched NPs yielded a contrast enhancement of 3.17 dB; which confirms that branched NPs are good contrast agent for OCT imaging. Additionally, the other peaks in the UV-NIR spectrum of the NPs suggest that branched NPs can be used for others OCT systems which central wavelength is below 1300 nm. In addition, if NPs are functionalized many other advanced analysis can be performed to prove their potential to finally be used for biomedical imaging.

List of Publications

I **Y. R. Ponce-de-Leon** ; J. A. Lopez-Rios ; J. L. Pichardo-Molina and N. Alcalá Ochoa, "Optical coherence tomography image enhancement by using gold nanoparticles", Proc. SPIE 8011, 22nd Congress of the International Commission for Optics: Light for the Development of the World, 80118W (November 02, 2011); doi:10.1117/12.902773; http://dx.doi.org/10.1117/12.902773

II **Y. Ponce de Leon**, J. L. Pichardo-Molina, N. Alcala-Ochoa, and J. A. Lopez-Rios, "Gold nanoparticles for improving contrast in Optical Coherence Tomography images," in Biomedical Optics and 3-D Imaging, OSA Technical Digest (Optical Society of America, 2012), paper BTu3A.97, http://dx.doi.org/10.1364/BIOMED.2012.BTu3A.97

III **Y. Ponce de León**, J. L. Pichardo-Molina, N. Alcalá Ochoa, and D. Luna-Moreno, "Contrast Enhancement of Optical Coherence Tomography Images Using Branched Gold Nanoparticles," Journal of Nanomaterials, vol. 2012, Article ID 571015, 9 pages, 2012. doi:10.1155/2012/571015, http://dx.doi.org/10.1155/2012/571015

IV **Y. Ponce de León**, J. L. Pichardo-Molina, N. Alcalá Ochoa, "Growth Kinetics of Concave Nanocubes Studied by Optical Coherence Tomography," Plasmonics, 2014, doi:10.1007/s11468-014-9696-1

List of Figures

List of Tables

Table

Contents

CHAPTER 1

Introduction

Imaging highly scattering tissues at a considerable depth with high resolutions, has been one of the major challenges in biomedical imaging. Currently, there exist different commercial standard imaging modalities such as ultrasound or microscopy that are able to provide depth resolved images of tissues; however, although ultrasound has a high depth capacity (~10cm), it is limited in axial resolution (~150µm); on the other hand microscopic techniques have high lateral resolution (1µm) but are limited in depth to a few hundreds of micrometers.

In 1991, a new imaging modality, which possess high axial and lateral resolutions (1-15µm) along with high depth capacity (12mm) to imaging transparent and highly scattering samples, was proposed by Huang et al. in the article untitled Optical Coherence Tomography [1]. The proposed OCT technique was an extension of the previous low coherence interferometry or reflectometry systems [2] which perform imaging in depth giving a longitudinal or axial scan of the sample. Meanwhile in an OCT system multiple longitudinal scans are performed at a series of lateral locations to obtain a two dimensional (tomographic) image of the sample which represents the backscattered or backreflected light as depth function. This mode of operation is analogous to ultrasound B-mode, and the basic principle is the same; it consist in measure the magnitude and echo time delays of sound waves in ultrasound and light waves in OCT. The sectioning capability of the OCT systems is similar to that of confocal microscopy; however, in OCT the axial resolution does not depend on the numerical aperture as in confocal microscopy; furthermore, in OCT lateral and axial resolutions are independent. This characteristic is useful for imaging deep tissues. In the first article of OCT [1], a human retina and a human coronary artery, both ex vivo, were examined to show the capabilities of the OCT technique for imaging transparent and highly scattering tissues. The central wavelength of the system was 830nm and it had an axial resolution of 17µm.

Since this first report, the main applications have been given in the ophthalmology and cardiovascular medical areas, which nowadays are in clinical practice.

The first OCT system, based on time domain detection, proved to be efficient for imaging transparent and highly scattering tissues; however, imaging speeds limited its utility for imaging in real time. In 1995 Fercher and coworkers [3] proposed the idea that it is also possible to perform detection in the Fourier domain by measuring the interference spectrum; and by 2003, three different groups [4-6] demonstrated that Fourier domain detection has a powerful sensitivity advantage over time domain detection, since Fourier domain essentially measures all of the echoes of light simultaneously, increasing the sensitivity and imaging speeds around 50 to 100 times. Almost parallel to the Fourier domain OCT system, another system in the Fourier domain but with a swept source was demonstrated in 1997 by Chinn et al. [7] and Golubovic et al. [8], although their performance was limited due to the laser technology in that time. It was until 2005 that the potential that this system offers was demonstrated, achieving record imaging speeds by using a novel swept laser technology [9].

The improvement of OCT systems has been one of the principal areas of research since its apparition [10]; consisting, among others, in the development and improvements of light sources [11, 12], handheld instruments [13, 14], probes [15, 16], or a combination of OCT with other technologies [17, 18]. All this new technology around OCT systems has resulted in a vast quantity of applications as well as a rapid growth in the market.

Basically time domain, spectral/Fourier domain, and swept source/Fourier domain are the types of OCT systems that exist based on the working principle; however, along the time other extensions of the technique have been developed. The most important have been Doppler OCT [19], and Polarization-Sensitive OCT (PS-OCT) [20]. Additionally, in order to imaging internal organs, OCT systems have been coupled with instruments such as, catheters or endoscopes.

The potential of the OCT technique consist in its capacity of imaging in situ, without contact and with high axial resolution and high depth penetration capacity in both, transparent and highly scattering media, like tissues. Nevertheless, tissues are optically inhomogeneous due to microscopic variations of the refractive index; it results in multiple scattering, limiting the image

axial resolution and depth. To overcome this difficulty a great variety of contrast agents or clearances have been used, such as molecular, dyes, or glucose. But among other disadvantages, they are expensive and present poor contrast enhancement. During the last decade, nanoparticles (NPs), mainly metallic, have been used in a wide variety of applications that goes from technological to biomedical, among them for contrast enhancement, because they present interesting optical properties such as highly scattering due to the property of localized surface plasmon resonance (LSPR), one of its advantages over other contrast agents is that by controlling their size, morphology, and composition, they can be tuned to be used for a specific application, including those in the NIR region.

In order to use NPs for applications, a good control over monodispersivity of size and morphology is desired as well as a high yield production. To get this goal is important to know the growth kinetics of NPs to determine the parameters that govern and affect the growth, and thus, be able to establish the chemical route to follow.

Metallic NPs are ideal to work with the OCT technique, principally those with concave surfaces due to the high scattering that they present [21, 22]. They can be easily detected with the OCT technique since OCT works by detecting backscattered or backreflected light. Taking this into account, two main objectives were set out and performed for this thesis. The first one was to prove that OCT is a viable technique to follow the growth kinetics of NPs. The second one was to show that NPs with concave surfaces, specifically branched NPs, are good to be used as contrast agent in OCT.

These two lines of investigation are very promising. The following of NPs growth kinetics with the OCT technique is the first time that is proposed and carried out. The way by means of which OCT can provide information about growth kinetics, is by recording a B-scan image at regular time intervals; to then, select an area of each image and calculate their contrast enhancement respect to a sample of ultrapure water; and by plotting the contrast enhancement as function of time, a growth kinetic plot can be obtained. This is analogous to the process followed in UV-Vis absorption spectroscopy, where the NP absorption is monitored as time function and finally plotted to get a growth kinetic plot. In order to show the feasibility of the technique for this application, the OCT results need to be compared with the results from other

known techniques. For this reason UV-Vis absorption spectroscopy and dynamic light scattering experiments were also carried out.

On the other line of investigation the objective is to show that NPs with concave surfaces, specifically branched NPs, can be used to enhance the contrast in OCT images. Other morphologies have been proposed to enhance the contrast in OCT images, however these NPs work well only when the central wavelength of the OCT system used matches with the peak of the surface plasmon band of the NPs. Branched NPs have their surface plasmon band peak around 700nm but due to the high scattering that they present, we want to prove that they can be used as contrast agent for OCT imaging at 1350nm, where our system works. To show this; a phantom, which mimics a tissue, will be used to insert NPs in it; and then, calculate the contrast enhancement respect to an area of the phantom where there is no NPs.

The content of this thesis is based on the objectives described above with the next order

Chapter 2 is dedicated to OCT generalities. In this chapter some statistics about the growth of the market and investigation are presented in order to have an idea of the importance of the technique. Additionally, a brief description of the OCT working principle, of the types of OCT systems, and of some applications is given.

Chapter 3 contains a description of NPs and their properties. Concepts of SPR and LSPR are described together with generalities of NPs with concave surfaces and their characteristics are also presented.

All the work done about following the growth kinetics of NPs by the OCT technique is described in chapter 4, starting with an introduction, then the description of the experiments carried out and finally results and conclusions.

Chapter 5 contains an introduction, details of the experiments and procedures carried out, as well as the results and conclusions of the work done for the use of branched NPs as contrast agents in tissue phantoms in order to increase the contrast in OCT images.

Finally, in chapter 6, general conclusions of the work done for this thesis are presented.

References

[1] D. Huang, E. A. Swanson, C. P. Lin, J. S. Schuman, W. G. Stinson, W. Chang, M. R. Hee, T. Flotte, K. Gregory, C. A. Puliafito, J. G. Fujimoto, "Optical Coherence Tomography," Science, vol. 254, no. 5035, pp. 1178-1181, 1991. doi: http://dx.doi.org/10.1126/science.1957169.

[2] H. H. Gilgen, R. P. Novak, R. P. Salathe, W. Hodel and P. Beaud, "Submillimeter Optical Reflectometry," Journal of Lightwave Technology, vol. 7, no. 8, pp. 1225-1233, 1989. doi: http://dx.doi.org/10.1109/50.32387.

[3] A. F. Fercher, C. K. Hitzenberger, G. Kamp, S. Y. El-Zaiat, "Measurement of intraocular distances by backscattering spectral interferometry," Optics Communications, vol. 117, no. 1–2, pp. 43-48, 1995. doi: http://dx.doi.org/10.1016/0030-4018(95)00119-S

[4] M. A. Choma, M. V. Sarunic, C. H. Yang, J. A. Izatt, "Sensitivity advantage of swept source and Fourier domain optical coherence tomography," Optics Express, vol. 11, no. 18, pp. 2183-2189, 2003. doi: http://dx.doi.org/10.1364/OE.11.002183.

[5] R. Leitgeb, C. K. Hitzenberger, and A. F. Fercher, "Performance of fourier domain vs. time domain optical coherence tomography," Optics Express, vol. 11, no. 8, pp. 889-894, 2003. http://dx.doi.org/10.1364/OE.11.000889.

[6] J. F. de Boer, B. Cense, B. H. Park, M. C. Pierce, G. J. Tearney, B. E. Bouma, "Improved signal-to-noise ratio in spectral-domain compared with time-domain optical coherence tomography," Optics Letters, vol. 28, no. 21, pp. 2067-2069, 2003. doi: http://dx.doi.org/10.1364/OL.28.002067.

[7] S. R. Chinn, E. A. Swanson, and J. G. Fujimoto, "Optical coherence tomography using a frequency-tunable optical source," Optics Letters, vol. 22, no. 5, pp. 340-342, 1997. doi: http://dx.doi.org/10.1364/OL.22.000340.

[8] B. Golubovic, B. E. Bouma, G. J. Tearney, and J. G. Fujimoto, "Optical frequency-domain reflectometry using rapid wavelength tuning of a Cr^{4+}:forsterite laser," Optics Letters, vol. 22, no. 22, pp. 1704-1706, 1997. doi: http://dx.doi.org/10.1364/OL.22.001704.

[9] W. Y. Oh, S. H. Yun, G. J. Tearney, and B. E. Bouma, "115 kHz tuning repetition rate ultrahigh-speed wavelength-swept semiconductor laser," Optics Letters, vol. 30, no. 23, pp. 3159-3161, 2005. doi: http://dx.doi.org/10.1364/OL.30.003159.

[10] http://www.octnews.org/articles/4061333/some-historical-statistics-of-academic-publication/.

[11] H. Kawagoe, S. Ishida, M. Aramaki, Y. Sakakibara, E. Omoda, H. Kataura, and N. Nishizawa, "Development of a high power supercontinuum source in the 1.7 μm wavelength region for highly penetrative ultrahigh-resolution optical coherence tomography," Biomedical Optics Express, vol. 5, no. 3, pp. 932-943, 2014. doi: http://dx.doi.org/10.1364/BOE.5.000932.

[12] S. Tozburun, M. Siddiqui, and B. J. Vakoc, "A rapid, dispersion-based wavelength-stepped and wavelength-swept laser for optical coherence tomography," Optics Express, vol. 22, no. 3, pp. 3414-3424, 2014. doi: http://dx.doi.org/10.1364/OE.22.003414.

[13] N. H. Cho, K. Park, R. E. Wijesinghe, Y. S. Shin, W. Jung, J. Kim, "Development of Real-Time Dual-Display Handheld and Bench-Top Hybrid-Mode SD-OCTs," Sensors, vol. 14, no. 2, pp. 2171-2181, 2014. doi: 10.3390/s140202171.

[14] C. D. Lu, M. F. Kraus, B. Potsaid, J. J. Liu, W. Choi, V. Jayaraman, A. E. Cable, J. Hornegger, J. S. Duker, and J. G. Fujimoto, "Handheld ultrahigh speed swept source optical coherence tomography instrument using a MEMS scanning mirror," Biomedical Optics Express, vol. 5, no. 1, pp. 293-311, 2014. doi: http://dx.doi.org/10.1364/BOE.5.000293.

[15] N. Zhang, T. H. Tsai, O. O. Ahsen, K. Liang, H. C. Lee, P. Xue, X. Li, and J. G. Fujimoto, "Compact piezoelectric transducer fiber scanning probe for optical coherence tomography," Optics Letters, vol. 39, no. 2, pp. 186-188, 2014. doi: http://dx.doi.org/10.1364/OL.39.000186.

[16] X. Yang, D. Lorenser, R. A. McLaughlin, R. W. Kirk, M. Edmond, M. C. Simpson, M. D. Grounds, and D. D. Sampson, "Imaging deep skeletal muscle structure using a high-sensitivity ultrathin side-viewing optical coherence tomography needle probe," Biomedical Optics Express, vol. 5, no. 1, pp. 136-148, 2014. doi: http://dx.doi.org/10.1364/BOE.5.000136.

[17] C. V. Bourantas, M. I. Papafaklis, L. Lakkas, A. Sakellarios, Y. Onuma, Y. J. Zhang, T. Muramatsu, R. Diletti, P. Bizopoulos, F. Kalatzis, K. K. Naka, D. I. Fotiadis, J. Wang, H. M. Garcia Garcia, T. Kimura, L. K. Michalis, P. W. Serruys, "Fusion of optical coherence tomographic and angiographic data for more accurate evaluation of the endothelial shear stress patterns and neointimal distribution after bioresorbable scaffold implantation: comparison with intravascular ultrasound-derived reconstructions," The international journal of cardiovascular imaging, vol. 30, no. 3, pp.485-94, 2014. doi: http://dx.doi.org/10.1007/s10554-014-0374-3.

[18] D. Hillmann, Ch. Luhrs, T. Bonin, P. Koch, and G. Huttmann, "Holoscopy-holographic optical coherence tomography," Optics Letters, vol. 36, no. 13, pp. 2390-2392, 2011. doi: http://dx.doi.org/10.1364/OL.36.002390.

[19] G. Liu, A. J. Lin, B. J. Tromberg, and Z. Chen, "A comparison of Doppler optical coherence tomography methods," Biomedical Optics Express, vol. 3, no. 10, pp. 2669-2680, 2012. http://dx.doi.org/10.1364/BOE.3.002669.

[20] K. H. Kim, M. C. Pierce, G. Maguluri, B. H. Park, S. J. Yoon, M. Lydon, R. Sheridan, and J. F. de Boer, "In vivo imaging of human burn injuries with polarization-sensitive optical coherence tomography," Journal of Biomedical Optics, vol. 17, no. 6, 2012. doi: http://dx.doi.org/10.1117/1.JBO.17.6.066012.

[21] H. Zhang, M. Jin, and Y. Xia, "Noble-Metal Nanocrystals with Concave Surfaces: Synthesis and Applications," Angewandte Chemie International Edition, vol. 51, no. 31, pp. 7656–7673, 2012. doi: http://dx.doi.org/10.1002/anie.201201557.

[22] C. L. Nehl, H. Liao, and J. H. Hafner, "Optical Properties of Star-Shaped Gold Nanoparticles," Nano Letters, vol. 6, No. 4, pp. 683-688, 2006. doi: http://dx.doi.org/10.1021/nl052409y.

CHAPTER 2

Optical Coherence Tomography

The Optical Coherence Tomography technique is an optical imaging modality similar to ultrasound that uses NIR light instead of sound. It performs cross sectional (tomographic) images with high axial and lateral resolutions of 1-15µm in situ, without contact, and in real time, which make it a powerful technique to be used in a great variety of applications, principally medical. OCT depth penetration capacity is of few mm; however, coupled with other devices such as catheter, endoscopic, laparoscopic or needle delivery can cover a major field of applications. OCT works by measuring the echo time delay and intensity of the backscattered or backreflected light from microstructures within the sample.

2.1. Comparison of OCT with other imaging modalities

Optical Coherence Tomography is called the optic analogous of ultrasound since both measure the time delay and intensity of waves backscattered or backreflected from within the sample; however, ultrasound has more depth capacity but less axial resolution than OCT. On the other hand, OCT has axial resolutions comparable with transverse resolutions of microscopic techniques, but more depth capacity, for these facts, it is said that OCT fills a gap between ultrasound and microscopic techniques. Fig. 2.1 shows a comparative diagram of these imaging modalities capacities [1].

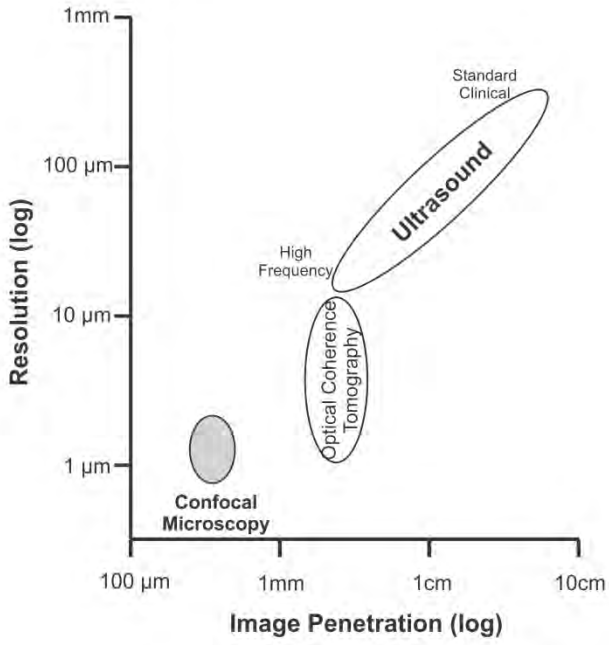

Fig. 2.1 Comparative diagram of the capacities of resolution and image penetration of ultrasound, optical coherence tomography, and confocal microscopy systems.

Ultrasound axial resolution depends on sound wave frequency, and although resolutions of 15-20µm can be reached at high ultrasound frequencies (~100 MHz) they are highly attenuated in biological tissues limiting the deep imaging to a few millimeters. On the other hand, at standard ultrasound frequencies, waves are transmitted with minimal absorption in biological tissues, which allows imaging deeper than OCT in the human body but with axial resolutions of 0.1-1mm; additionally, since ultrasound uses sound waves, it requires direct contact with the sample or an immersion in liquid to transmit the sound waves. In contrast, in OCT, axial resolutions of 1-15µm can be reached and image acquisition is made without contact, neither a transducing medium.

Some imaging techniques with high transverse resolutions are microscopy or confocal microscopy, which generate *en-face* images with transverse resolutions of around 1µm. However, imaging depth in biological tissues is limited since image signal and contrast are significantly degraded by multiple optical scattering, allowing depths of only a few hundreds of micrometers. OCT has axial resolution of 1-15µm with depth capacities of few mm which makes better than microscopy techniques for imaging deeper in highly scattering tissues.

2.2 OCT marketing and scientific output

To understand the importance of the growth that the OCT technique has had in the market, as in the research area, is necessary to show some statistics. The first paper of this technique by Huang et al. [2], reported the analysis of a human retina and a human coronary artery, both ex-vivo. Since then, the principal field of research and the main market in OCT systems has been given in the ophthalmic area, followed by cardiovascular. However, a significant number of applications in other fields such as dermatology, dentistry, neurology, and more have been reported.

Figure 2.2 shows a graph of the annual revenue from 1996 to 2012 for ophthalmic OCT system market in the world. As can be seen on the graph in 2002 revenue were below $50M/year, ten years later, these exceeded $300M/year, which gives an idea of the enormous growth in the market of ophthalmic OCT systems. Although nowadays there are more than 36 OCT system companies in the market [3], only 14 make ophthalmic OCT instruments, about 10 of them in the diagnostic ophthalmology OCT market and 4 that use OCT guide laser surgical procedures in ophthalmic applications. These are: Alcon/LenSx, Bioptigen, Canon/Optopol, Heidelberg Engineering, Nidek, OptiMedica, Optos/OTI, Optovue, Schwind, Shenzhen Moptim Imaging, Technolas Perfect Vision, Tomey, Topcon, and Zeiss. Among them the leading companies are Zeiss, Optovue, Heidelberg Engineering, and Topcon [4].

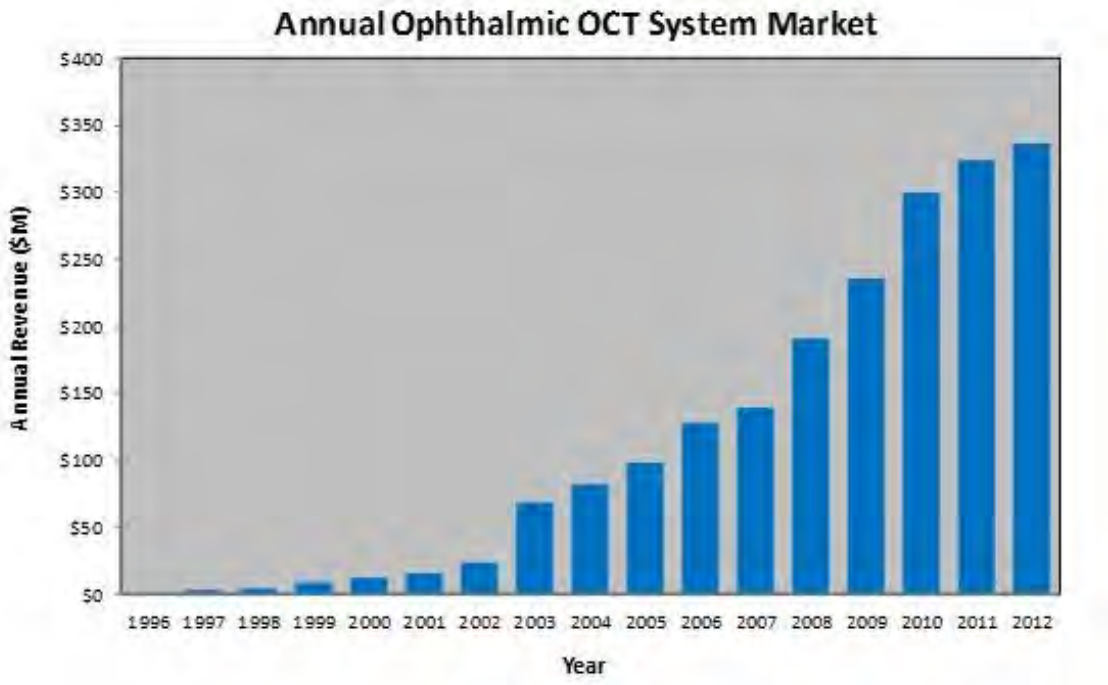

Fig. 2.2 Graph of the growth of the ophthalmic OCT market from 1996 to 2012 [4]**.**

In the aspect of publications, in October 2012, an analysis of the estimated articles published in the OCT field was presented in the website OCT News in the article untitled "Some Historical Statistics of Academic Publications in the Field of Optical Coherence Tomography" [5]. Table 2.1 shows the detailed information of the estimated articles published by field annually from 1991 to September 2012. Fig. 2.3 shows the graph corresponding to the data of table 2.1. The growth rate of publications is around 200 articles per year and the principal area is ophthalmology, followed by technology and in third place cardiology. Something to notice is that ophthalmology papers are 7 times those in the technology field; something similar happens with the cardiology field. The reason for this tremendous difference is that OCT is a very promising technology for ophthalmology. Additionally, national institute of health (NIH), national eye institute (NEI), and government agencies around the world have being providing massive founding, and also, commercial companies provided early commercial OCT systems devoted to ophthalmic applications. An important fact is that most of the articles in ophthalmology are reported by people working in the medical/clinical area working with commercial systems. Is also important to

mention that the second field with most articles is technology, which in this case is about all the articles devoted to the development or improvement of OCT systems.

The data presented show how much important has been the OCT technique in the medical area, without underestimated the importance of applications in other non-medical fields, even though there are not many articles.

Table 2.1 Data of the OCT articles published annually from 1991 to September 2012 [5].

Field \ Year	1991	1992	1993	1994	1995	1996	1997	1998	1999	2000	2001	2002	2003	2004	2005	2006	2007	2008	2009	2010	2011	2012	Total
Ophtalmology			3	1	8	9	7	19	34	80	89	101	162	208	388	474	685	772	931	1198	1359	1188	7716
Technology	1	0	1	1	2	2	8	18	11	13	17	41	56	101	71	68	89	97	102	144	125	105	1073
Cardiovascular						4	1	4	2	3	4	8	13	6	23	90	45	119	182	155	207	193	1059
Gastroenterology & Endoscopy							4	3	1	9	7	13	11	10	18	19	18	13	17	19	21	15	198
Dermatology							1	2	2	5	2	1	3	13	7	15	13	13	20	31	31	31	190
Dentistry								1	1	3	1	1	3	4	5	4	4	16	16	16	19	12	106
Neurology						1		1					4	3	4	6	2	9	12	12	20	26	100
Otolaryngology										1	2	1	1	4	6	12	3	13	13	17	9	4	86
Urology							1			1	2	3	2		1	6	5	12	14	11	10	15	83
Brocoscopy & Pulmonology								1					1	1	3	2	3	9	15	12	7	11	65
Other Medical											1	1	2	3	2	9	9	3	5	8	11	9	63
Developmental Biology						1	1			1			1	2		4	5	6	12	8	15	4	60
Orthopedics & Rheumatology									1		1	2	5	3	6	2	6	7	3	8	5	9	58
Oral Cavity (not dentistry)								2		1				4	2	1	2	3	8	4	3	6	36
Gynecology								1	2				1	2	1	2	1	3	5	5	7	5	35
NDE/NDT							1	1	1				1		1		1		1	7	6	1	21
Microscopy				1						1		2			3	2	1		1	2	2	4	19
Other Non-Medical														1		1	1	1	4	2	2		12
Surgery							1	1	1								1		1	2	3	1	11
Total	1	0	4	3	10	17	25	54	56	118	126	174	266	365	541	717	894	1096	1362	1661	1862	1639	10991

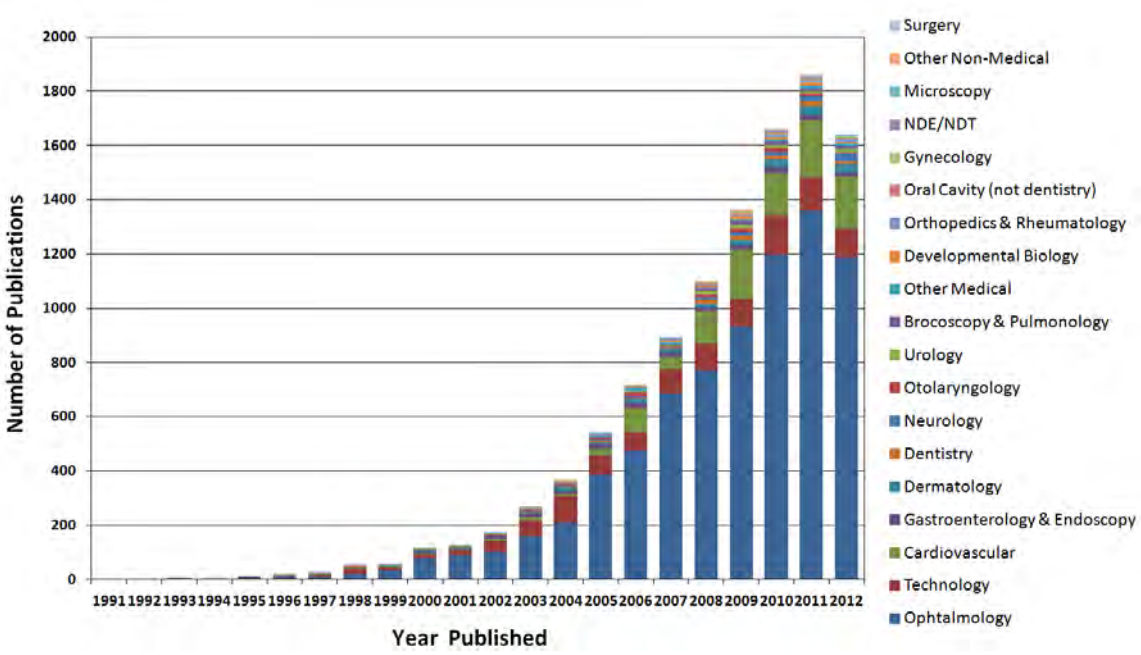

Fig. 2.3 Graph of the OCT articles published annually from 1991 to September 2012 [5].

2.3 Fundamentals of the working principle

As mentioned before, OCT works similar to ultrasound by measuring the intensity and echo time delay of light instead of sound. In ultrasound the echo time delay of sound waves is performed by direct electronic detection; however, light velocity is approximately a million times faster than sound velocity, consequently, delays are in the range of femtoseconds which are not possible to detect directly by electronic means. Therefore, measurement methods such as high-speed optical gating, optical correlation, or interferometry must be used. In OCT these measurements are typically based on interferometry techniques, recurring in most of the cases to a Michelson interferometer, where the backscattered or backreflected signal from the sample is compared with a reference light traveling a known path length.

Similar to ultrasound, in OCT an axial scan is called A-scan, a tomographic image or 2D is called B-scan whereas a three dimensional image is called C-scan, and can be manipulated similar to magnetic resonance (MR) or computer tomography (CT) images. The OCT modes of scans are

shown in Fig. 2.4. The 1D o A-scan, Fig. 2.4a, is an axial scan which represents the backscattering intensity versus depth. By performing a longitudinal scan, it is a sequence of axial scans, a 2D image (B-scan) is obtained; see Fig. 2.4b, where the optical scattering within the sample is represented in an image of transversal distance versus depth. Three dimensional images, Fig. 2.4c., are generated by acquiring a sequence of B-scan images.

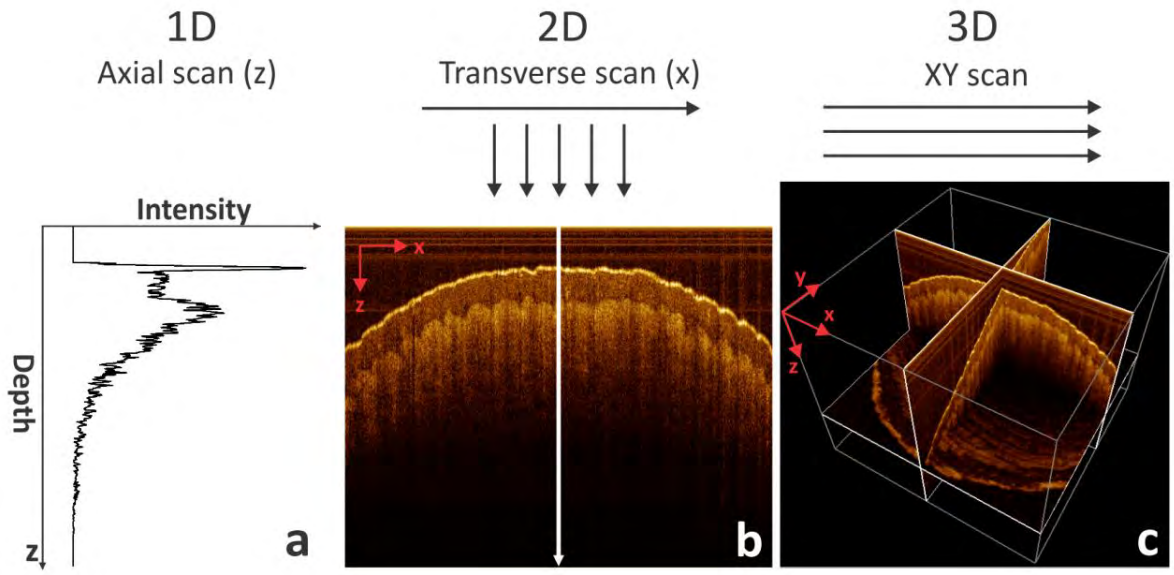

Fig. 2.4 OCT modes of scans. a) 1D image or A-scan; b) 2D image or B-scan; c) 3D image or C-scan.

An important characteristic of the OCT systems is that lateral and axial resolutions are independent. In OCT the axial image resolution is determined by the bandwidth, it is the coherence length of the light source; whereas lateral or transverse resolution is the same as for conventional optical microscopy and is determined by the diffraction limited spot size of the focused optical beam and is also related with the depth of field. Axial and transverse resolution equations are respectively Eq. 2.1 and 2.2 [1].

$$\Delta z = \frac{2Ln2}{\pi}\left(\frac{\lambda^2}{\Delta\lambda}\right) \tag{2.1}$$

$$\Delta x = \frac{4\lambda}{\pi}\left(\frac{f}{d}\right) \tag{2.2}$$

In the axial resolution equation (Eq. 2.1) Δz and Δλ are the full width at half-maximum (FWHM) of the autocorrelation function and power spectrum, respectively; and λ is the central wavelength of the source light. On the lateral resolution equation (Eq. 2.2), *d* is the spot size on the objective lens and *f* is the focal length. Current OCT technologies have axial resolutions ranging from 1 to 15 μm, approximately 10–100 times finer than standard ultrasound.

2.4 OCT systems

An important advantage of the OCT systems is that they can be built with fiber-optic components. However, for better understanding, the types of OCT will be described with a simple scheme of a Michelson interferometer

Three are the basic types of OCT systems based on interferometric detection, one of them works in time domain, and the other two in the Fourier domain; these last are spectral/Fourier domain and swept source/ Fourier domain or also called optical frequency domain imaging (OFDI). These systems are briefly described in the next subsections. Also, there exist other categories of OCT systems that are extensions of the previously mentioned which would be also listed.

Time domain OCT system

The time domain OCT system consists of a Michelson interferometer with a (low coherence) broad bandwidth light source and a photodetector. The light is split into two beams, the sample and the reference arms, as can be seen in Fig. 2.5. One of the beams is directed to the sample and is backscattered or backreflected from it, the second beam is reflected by a reference mirror, to then recombine both beams and form interference, which is observed only when the

path lengths of both arms are matched to within the coherence length of the light. The information of magnitude and echo time delay is contained in the interference signal, which is acquired with a detector. By translating the reference mirror, a scanning of the reference arm is performed; and the signal detected is demodulated to obtain an axial scan or A-scan, which represents the backscattering or backreflected light versus depth. By scanning the beam sample transversely, a two dimensional (B-scan) is obtained, which represents the optical backscattering in a cross-sectional plane through the sample. To get a 3D image a sequence of B-scan needs to be performed [1].

Due to interferometry measures the light field rather than the intensity of light, it is equivalent to heterodyne detection in optical communication. The weak signals from the sample beam are multiplied by the strong signals of the electric field of the reference beam; as a result, the magnitude of the oscillating term detected is increased. The interferometer thus produces heterodyne gain for weak optical signals [1, 6].

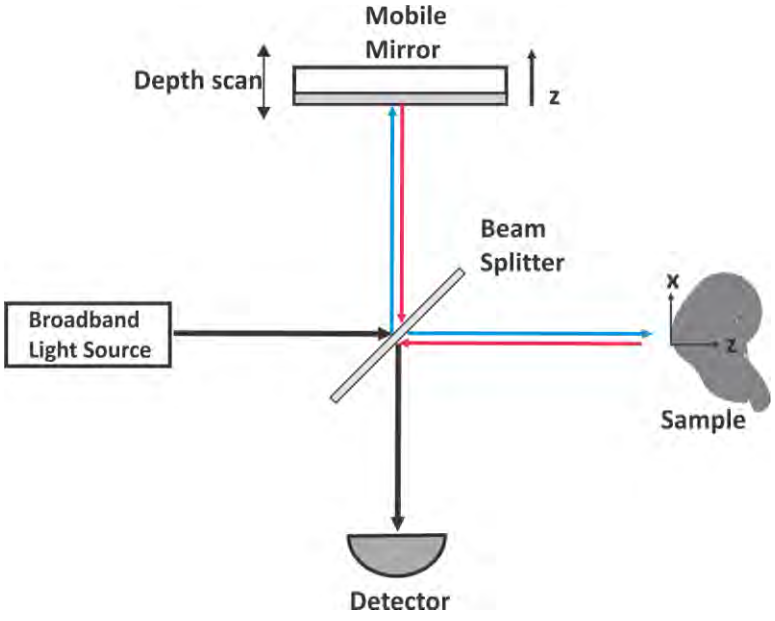

Fig. 2.5 Diagram of a Time Domain OCT system.

Spectral/Fourier domain OCT system

Spectral/Fourier domain was the advanced OCT from time domain, Fercher et a. [7] in 1995 proposed that by measuring the interference spectrum is possible to perform detection in the Fourier domain, and by 2003 different groups [8-10] demonstrated that Fourier domain detection has a powerful sensitivity advantage over time domain detection, since Fourier domain detection basically measures all of the echoes of light simultaneously, increasing sensitivity and imaging speeds 50 to 100 times

As in time domain OCT, Spectral/Fourier domain OCT systems use a Michelson interferometer and a broad bandwidth light source; but here the spectrum from the interferometer is detected using a spectrometer and a line scan camera, and the reference mirror is fixed, see Fig 2.6. As in time domain the light is split into two beams, the reference and the sample beams, the reference beam goes to a fixed mirror which reflects the light, and the sample beam is directed to the sample and is backscattered or backreflected from within the sample at different depths. The interference produced by the two beams is modulated as function of the frequency, which is proportional to the path length difference and related with the depth of the sample. The interference is measured with a spectrometer; and an A-scan can be obtained by rescaling the spectrometer output from wavelength to frequency and Fourier transforming the interference signal [6]. By performing a sequence of axial scans a B-scan image is obtained and a sequence of B-scan images yields 3D-OCT volumetric information.

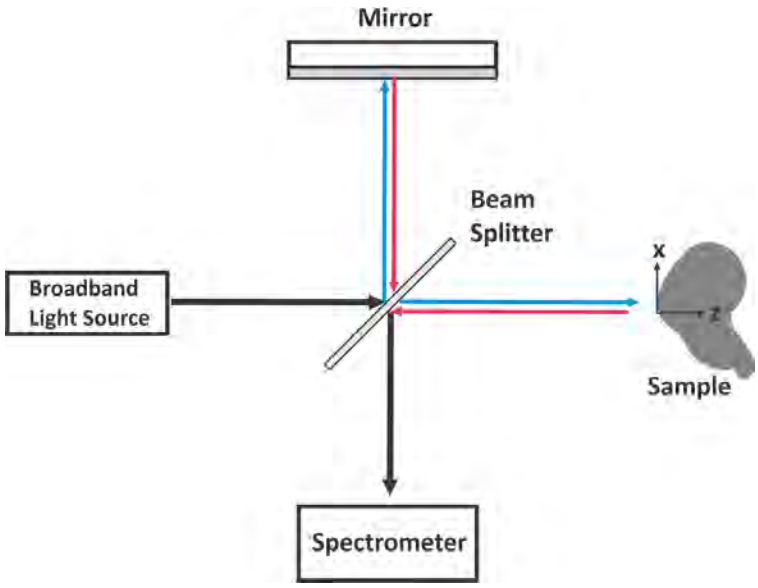

Fig. 2.6 Diagram of a Spectral/Fourier domain OCT system.

Swept Source/Fourier domain OCT system

Swept Source/Fourier domain detection OCT systems or also known as optical frequency domain interferometry (OFDI), similar to Spectral/Fourier domain OCT system, it uses a Michelson interferometer with the reference arm fixed. But unlike Spectral/Fourier domain, it uses a swept source with a narrow bandwidth, which is frequency swept in time. Also, the interference signal is detected with a single photodetector, while tuning the light source rather than in parallel with a spectrometer.

In this system the same description of Spectral/Fourier domain OCT applies. However, the reference and sample beams have a time offset determined by the path length difference, and because the frequency of the light is swept as function of time, the light echoes in the sample beam will have a frequency offset from the reference beam. When interference is generated a modulation or beat in intensity is produced at a frequency which is given by this frequency offset. And by digitizing the signal over a single frequency sweep of the light source, correcting any nonlinearity in the frequency sweep as time function, and then Fourier transforming this beat

frequency signal, an axial scan measurement of the magnitude and echo time delay from the sample is obtained [6].

Swept Source OCT systems have the advantage that detection is made at the same time rater than sequentially as in time domain detection, which permits high speed imaging; it also uses a single photodetector, and not a line scan camera as in Spectral Fourier domain, which allows their use in wavelengths from 1000 to 1300nm.

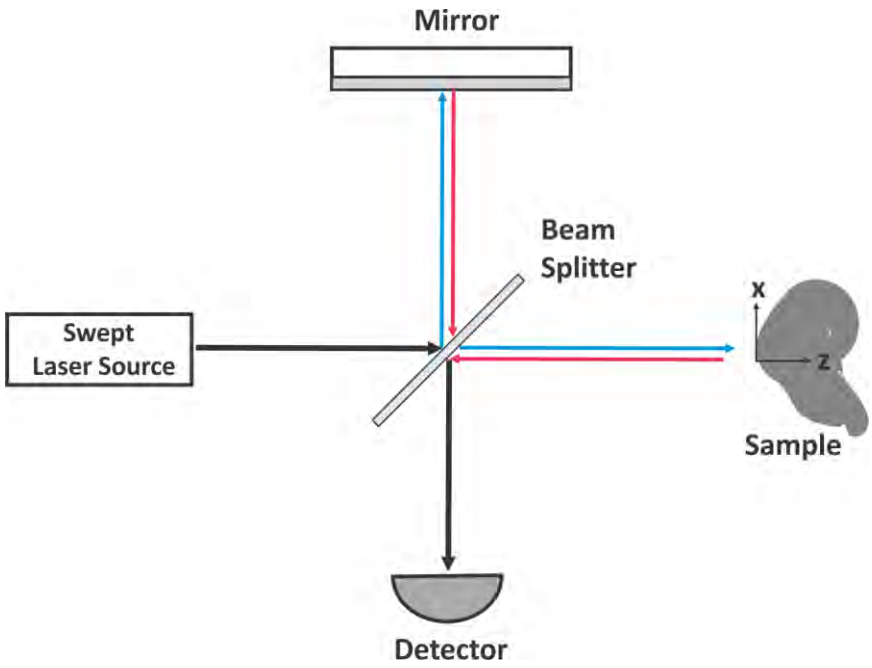

Fig. 2.7 Diagram of a Swept Source /Fourier domain OCT system.

As a summary of the OCT systems described before, the table 2.2 is presented; where the differences in light source, mobile parts, detection system, and method of image reconstruction among systems are listed.

Table 2.2 Comparative table of the time domain, spectral domain and swept source OCT systems.

OCT system	**Light source**	**Mirror in the reference arm**	**Detection system**	**Image reconstruction method**
Time domain	Broad bandwidth	Mobile	Photodetector	Demodulating
Spectral/fourier domain	Broad bandwidth	Fixed	Spectrometer and a line scan camera	Fourier transforming
Swept Source/Fourier domain	Swept source	Fixed	Photodetector	Fourier transforming

Extensions of the OCT systems

In the improvement of OCT systems some extensions have been developed, such as Doppler or Polarization-Sensitive OCT (PS-OCT), *en-face* or full field OCT. These are described briefly in this section. OCT systems had also been coupled with other devices such as catheters, endoscopes, laparoscopes or needle delivery in order to inspection internal body parts.

Doppler Optical Coherence Tomography. This technique measures and maps flow velocity by combining the OCT technique with laser Doppler velocimetry. The concept can be understood knowing that displacements of flow in the sample introduce small frequency shifts (Doppler shifts) in the backscattered or backreflected light; when interfering with the reference beam, these Doppler shifts lead to a time dependent change of the interference pattern; that processed, information of microstructure and flow velocity is obtained. Conventional laser Doppler velocimetry is typically a non imaging technique, whereas Doppler OCT can provide local velocity mapping with high spatial resolution. As a result, Doppler OCT has found distinct applications in the field of laser Doppler velocimetry [11].

Polarization-Sensitive Optical Coherence Tomography (PS-OCT). This technique is based on detecting the changes in the polarization state of light re-emitted from the sample. Polarization state of light can give extra information of the sample. There exist different configurations, one of them is when light linearly polarized is used in the reference arm, whereas circularly polarized light

is used in the other arm, which incidents on the sample, and then is reflected with an arbitrary polarization state, depending on the properties of the sample. Beams recombine and then, the light is split in horizontal and vertical polarization components and detected separately.

Many biological tissues exhibit birefringence, changes in birefringence may, for instance, indicate changes in functionality, structure or viability of tissues [12]. Therefore, PS-OCT may be a powerful clinical technology.

***En-face* acquisition mode.** Despite depth penetration capacity of OCT systems is an advantage for some applications, for others applications a better lateral or transverse resolution and less depth capacity are required. In this way, different systems which perform *en-face* imaging have been developed. They are, Optical coherence Microscopy (OCM), *en-face* OCT, or Full field OCT. OCM and *en-face* OCT performs scans laterally instead of axial as in typical OCT. Full field OCT does not performs any X-Y scans, it acquires a complete *en-face* image by illuminating all the field of view taking only one shot. The only scan that it performs is in the Z plane to acquire images at different depths of the sample to generate a 3D image. The transverse resolutions of these systems are around 1µm. A comparative technique is the called wavelength scanning interferometry (WSI), which is a full field technique that uses a tunable light source; that by scanning the wavelength, it acquires information in depth. Since the light source is changing in time, it is also similar, to swept source OCT.

OCT coupled with other devices. Coupled with catheter, endoscopic, laparoscopic, or needle delivery devices, OCT is having a powerful impact on many medical applications, for instance, for analyze cardiovascular system, gastrointestinal or respiratory tract among others. This combination of OCT with probe devices have made that OCT extends their capacity to be applied where typical OCT imaging would be impossible and in applications that are having a great impact.

2.5 Applications

As mentioned before, the principal application of the OCT systems is in ophthalmology followed by cardiology, gastroenterology & endoscopy, dermatology, dentistry, neurology, otolaryngology, urology, broncoscopy & pulmonology, other medical, developmental biology, oral cavity, gynecology, non-destructive evaluation/examination (NDE)/non-destructive testing (NDT), microscopy, surgery, and other non-medical, as was shown in the statistics section. The second area of most publications is the field of technology; nevertheless, the works included in this category are those that involve the development and improvements of OCT systems.

OCT in ophthalmology. It was the first application together with cardiovascular. Since the beginning the promising potential of the technique to be applied in ophthalmology was clear. Its viability to work with transparent tissues, none invasively, with higher resolution than any other ophthalmic system, and the independence of axial resolution from numerical aperture constitute the characteristics that have made OCT a current commercial tool in ophthalmology and the mean topic of research in OCT. For ophthalmologist its simplicity, fast imaging, reliability, repeatability and quantification of measures and results are the main reasons of success of OCT in the market. Its applications in ophthalmology are very extensive; among them, for the diagnosis and monitoring of many retinal diseases such as glaucoma, or macular edema associated with diabetic retinopathy. The OCT technique is able to identify early stages of disease before physical symptoms. Additionally, the track of pathology can be possible, as before such as after intervention.

OCT in cardiology. Cardiovascular disease is one of the mean causes of death around the world. In this medical area OCT make use of catheters. Its resolution is about 10 times higher than intravascular ultrasound. OCT may provide characterization and differentiation of plaque components better than ultrasound, making it an attractive imaging method for the identification of vulnerable plaque. The use of OCT systems in cardiology is very extensive, since ex-vivo analysis to the use for guidance in interventions, principally coronary [13]. It has been also combined with other techniques like angiography to get better analyses [14].

OCT in gastroenterology. Coupled with different tools, such as catheters or endoscopes, OCT has been able to acquire images of the gastrointestinal tract *in vivo* at real time. The first *in vivo* study was in 1997 by A.M. Sergeev [15]. One of the principal diseases in the gastrointestinal tract is Barrett's Esophagus (BE). Patients with BE have an increased risk for development of esophageal adenocarcinoma which has increased by 300-400% in white men in the last 30 years [16]. OCT has contributed in different findings in BE, also as in the study of other parts of the gastrointestinal tract. Recently, a new technique for inspectioning gastrointestinal tract was proposed, which is a tethered capsule endomicroscope that is swallowed by the patient and provides microscopic information from the entire esophagus as the pill passes through the gastrointestinal tract [17]. It is based in Optical Coherence Tomography termed optical frequency domain imaging.

Other applications. There exist many other applications reported in OCT, to mention few, for example in dermatology where OCT is used to analyze principally melanoma cancer, another application is in dentistry for analyzing structural components of teeth, or in the art field to analyze paintings and objects of cultural heritage. An interesting application has been proposed recently. It consists in the possibility to integrate a handheld OCT system with Google Glass. This is being exploring by a group at the University of Illinois at Urbana-Champaing (USA). The system will allows the physician to focus on the patient during the medical history review and during the patient exam, resulting in potential improvements to the quality of care and efficient access to real-time data for display and analysis [18].

As can be observed, the main applications of OCT systems are in the medical area, where most of the tissues are highly scattering. For this reason, different materials have been suggested and analyzed as clearing or contrast agents for OCT imaging. For instance, clearing agents such as glycerol [19], PEG-400 [20], a mix of both [21], and others [22, 23]. Among the contrast agent reported for OCT imaging the most used are NPs. Although NPs of different materials have been reported, such as polymeric NPs [24, 25], or TiO_2 [26], the most used are gold NPs [27-31]. In this thesis one of the works reported is precisely the use of branched gold NPs as contrast agent for OCT imaging; detailed in chapter 5. The implications of use contrast agents improve importantly the applications of the OCT technique.

Among the non-medical applications is the use of the OCT technique for following the NPs growth kinetics, which we are proposing for the first time and we hope it will be an active field of research in future years. This investigation is detailed in chapter 4.

2.6 Thorlabs OCS 1300 SS Swept Source OCT system

The OCT system used for the realization of this thesis was a commercial OCT from Thorlabs, which can be seen in Fig. 2.8. The system is a Swept Source OCT with a central wavelength at 1325nm and a spectral bandwidth of 100nm. The coherence length of the source is 6mm and the average output power is 10mW. The maximum image depth is 3mm, whereas the transverse resolution is 15µm. The axial resolution is 12µm in air and 9µm in water. The maximum volume size is 10 x 10 x 3 mm corresponding to length x width x depth. More details about the system can be consulted in the appendix.

Fig. 2.8 Thorlabs OCS 1300SS Swept Source OCT system.

References

[1] J. G. Fujimoto, Optical Coherence Tomography: Introduction. In: B. E. Bouma, G. J. Tearney (eds.) Handbook of optical coherence tomography. Marcel Dekker, New York, pp. 1-40, 2002.

[2] D. Huang, E. A. Swanson, C. P. Lin, J. S. Schuman, W. G. Stinson, W. Chang, M. R. Hee, T. Flotte, K. Gregory, C. A. Puliafito, J. G. Fujimoto, "Optical Coherence Tomography," Science, vol. 254, no. 5035, pp. 1178-1181, 1991. doi: http://dx.doi.org/10.1126/science.1957169.

[3] E. Swanson, "Some Historical Statistics on Companies in the Market of Optical Coherence Tomography Systems," Optical Coherence Tomography News, Other Business News, Nov. 2012. http://www.octnews.org/articles/4111178/some-historical-statistics-on-companies-in-the-mar/

[4] E. Swanson, "Estimates of Ophthalmic OCT Market Size and the Dramatic Reduction in Reimbursement Payments," Optical Coherence Tomography News, Ophthalmology, Dec. 2012. http://www.octnews.org/articles/4176266/estimates-of-ophthalmic-oct-market-size-and-the-dr/

[5] E. Swanson "Some Historical Statistics of Academic Publications in the Field of Optical Coherence Tomography," Optical Coherence Tomography News, Oct. 2012. http://www.octnews.org/articles/4061333/some-historical-statistics-of-academic-publication/

[6] W. Drexler, J. G. Fujimoto, Introduction to Optical Coherence Tomography. In: W. Drexler, J. G. Fujimoto (eds.) Optical Coherence Tomography, Technology and Applications, Springer Berlin Heidelberg, New York, pp. 1-45, 2008.

[7] A.F. Fercher, C.K. Hitzenberger, G. Kamp, S.Y. El-Zaiat, "Measurement of intraocular distances by backscattering spectral interferometry," Optics Communications, vol. 117, no. 1–2, pp. 43-48, 1995. doi: http://dx.doi.org/10.1016/0030-4018(95)00119-S.

[8] M. A. Choma, M. V. Sarunic, C. H. Yang, J. A. Izatt, "Sensitivity advantage of swept source and Fourier domain optical coherence tomography," Optics Express, vol. 11, no. 18, pp. 2183-2189, 2003. doi: http://dx.doi.org/10.1364/OE.11.002183.

[9] R. Leitgeb, C. K. Hitzenberger, and A. F. Fercher, "Performance of fourier domain vs. time domain optical coherence tomography," Optics Express, vol. 11, no. 8, pp. 889-894, 2003. http://dx.doi.org/10.1364/OE.11.000889.

[10] J. F. de Boer, B. Cense, B. H. Park, M. C. Pierce, G. J. Tearney, B. E. Bouma, "Improved signal-to-noise ratio in spectral-domain compared with time-domain optical coherence tomography," Optics Letters, vol. 28, no. 21, pp. 2067-2069, 2003. doi: http://dx.doi.org/10.1364/OL.28.002067.

[11] B. Liu, Doppler Optical Coherence Tomography. In: M. E. Brezinsky, Optical Coherence Tomography, Principles and Applications, Academic Press, pp. 277-304, 2006, ISBN: 978-0-12-133570-0.

[12] J. F. De Boer, S. M. Srinivas, J. S. Nelson. T. E. Milner, and M. G. Ducros, Polarization-Sensitive Optical Coherencen Tomography. In: B. E. Bouma, G. J. Tearney (eds.) Handbook of optical coherence tomography. Marcel Dekker, New York, pp. 237–274, 2002.

[13] L. Di Vito, F. Prati "OCT Guidance to Improve Clinical Outcome of Coronary Interventions: What Have We Learnt?," Current Cardiovascular Imaging Reports, vol. 6, no. 5, pp. 421-425, 2013. doi: http://dx.doi.org/10.1007/s12410-013-9220-6.

[14] C. V. Bourantas, M. I. Papafaklis, L. Lakkas, A. Sakellarios, Y. Onuma, Y. J. Zhang, T. Muramatsu, R. Diletti, P. Bizopoulos, F. Kalatzis, K. K. Naka, D. I. Fotiadis, J. Wang, H. M. Garcia Garcia, T. Kimura, L. K. Michalis, P. W. Serruys, "Fusion of optical coherence tomographic and angiographic data for more accurate evaluation of the endothelial shear stress patterns and neointimal distribution after bioresorbable scaffold implantation: comparison with intravascular ultrasound-derived reconstructions," The International Journal of Cardiovascular Imaging, vol. 30, no. 3, pp. 485-494, 2014. doi: http://dx.doi.org/10.1007/s10554-014-0374-3.

[15] A. M. Sergeev, V. M. Gelikonov, G. V. Gelikonov, F. I. Feldchtein, R. V. Kuranov, N. D. Gladkova, N. M. Shakhova, L. B. Snopova, A. V. Shakhov, I. A. Kuznetzova, A. N. Denisenko, V. V. Pochinko, Yu. P. Chumakov, and O. S. Streltzova, "In vivo endoscopic OCT imaging of precancer and cancer states of human mucosa," Optics Express, vol. 1, no. 13, pp. 432–440, 1997. doi: http://dx.doi.org/10.1364/OE.1.000432.

[16] T. S. Kirtane and M. S. Wagh, "Endoscopic Optical Coherence Tomography (OCT): Advances in Gastrointestinal Imaging," Gastroenterology Research and Practice, vol. 2014, Article ID 376367, 7 pages, 2014. doi: http://dx.doi.org/10.1155/2014/376367.

[17] M. J. Gora, J. S. Sauk, R. W. Carruth, W. Lu, D. T. Carlton, A. Soomro, M. Rosenberg, N. S. Nishioka, G. J. Tearney, "Imaging the Upper Gastrointestinal Tract in Unsedated Patients Using Tethered Capsule Endomicroscopy," Gastroenterology, vol. 145, no. 4, pp. 723-725, 2013, http://dx.doi.org/10.1053/j.gastro.2013.07.053.

[18] G. L. Monroy, N. D. Shemonski, R. L. Shelton, R. M. Nolan, S. A. Boppart, "Implementation and evaluation of Google Glass for visualizing real-time image and patient data in the primary care office," Proceedings of SPIE 8935, Advanced Biomedical and Clinical Diagnostic Systems XII, 893514, 2014, doi: http://dx.doi.org/10.1117/12.2040221.

[19] S. G. Proskurin, and I. V. Meglinski, "Optical coherence tomography imaging depth enhancement by superficial skin optical clearing", Laser Physics Letters, vol. 4, no. 11, pp. 824–826, 2007. doi: http://dx.doi.org/10.1002/lapl.200710056.

[20] X. Wen, S. L. Jacques, V. V. Tuchin, D. Zhu, "Enhanced optical clearing of skin in vivo and optical coherence tomography in-depth imaging," Journal of Biomedical Optics, vol. 17, no. 6, 2012, doi: http://dx.doi.org/10.1117/1.JBO.17.6.066022.

[21] E. A. Genina, A. N. Bashkatov, E. A. Kolesnikova, M. V. Basko, G. S. Terentyuk, V. V. Tuchin, "Optical coherence tomography monitoring of enhanced skin optical clearing in rats in vivo," Journal of Biomedical Optics, vol. 19, no. 2, 2013, doi: http://dx.doi.org/10.1117/1.JBO.19.2.021109.

[22] H. Shan, Y. Liang, J. Wang, Y. Li, "Study on application of optical clearing technique in skin diseases," Journal of Biomedical Optics, vol. 17, no. 11, 2012, doi: http://dx.doi.org/10.1117/1.JBO.17.11.115003.

[23] O. Zhernovaya, V. V. Tuchin, M. J. Leahy, "Blood optical clearing studied by optical coherence tomography," Journal of Biomedical Optics, vol. 18, no. 2, 2013, doi: http://dx.doi.org/10.1117/1.JBO.18.2.026014.

[24] W. Al Rawashdeh, S. Kray, A. Pich, S. Pargen, A. Balaceanu, M. Lenz, F. Spöler, F. Kiessling, W. Lederle, "Polymeric nanoparticles as OCT contrast agents," Journal of Nanoparticle Research, vol. 14, no. 12, 2012. doi: http://dx.doi.org/10.1007/s11051-012-1255-0.

[25] K. M. Au, Z. Lu, S. J. Matcher, S. P. Armes, "Anti-biofouling conducting polymer nanoparticles as a label-free optical contrast agent for high resolution subsurface biomedical imaging," Biomaterials, vol. 34, no. 35, pp. 8925–8940, 2013. doi: http://dx.doi.org/10.1016/j.biomaterials.2013.07.094.

[26] M. Kirillin, M. Shirmanova, M. Sirotkina, M. Bugrova, B. Khlebtsov, E. Zagaynova, "Contrasting properties of gold nanoshells and titanium dioxide nanoparticles for optical coherence tomography imaging of skin: Monte Carlo simulations and in vivo study," Journal of Biomedical Optics, vol. 14, no. 2, 2009, doi: http://dx.doi.org/10.1117/1.3122373.

[27] T. S. Troutman, J. K. Barton, and M. Romanowski, "Optical coherence tomography with plasmon resonant nanorods of gold," Optics Letters, vol. 32, no. 11, pp. 1438-1440, 2007. doi: http://dx.doi.org/10.1364/OL.32.001438.

[28] H. Cang, T. Sun, Z. Y. Li, J. Chen, B. J. Wiley, Y. Xia, and X. Li, "Gold nanocages as contrast agents for spectroscopic optical coherence tomography," Optics Letters, vol. 30, no. 22, pp. 3048-3050, 2005. doi: http://dx.doi.org/10.1364/OL.30.003048.

[29] T. T. Chi, Y. C. Tu, M. J. Li, C. K. Chu, Y. W. Chang, C. K. Yu, Y. W. Kiang, and C. C. Yang, "Photothermal optical coherence tomography based on the localized surface plasmon resonance of Au nanoring," Optics Express, vol. 22, no. 10, pp. 11754-11769, 2014. doi: http://dx.doi.org/10.1364/OE.22.011754.

[30] A. Agrawal, S. Huang, A. W. Haw Lin, J. K. Barton, R. A. Drezek, T. J. Pfefer, M. H. Lee. "Quantitative evaluation of optical coherence tomography signal enhancement with gold nanoshells," Journal of Biomedical Optics, vol. 11, no. 4, 2006. doi: http://dx.doi.org/10.1117/1.2339071.

[31] A. M. Gobin, M. H. Lee, N. J. Halas, W. D. James, R. A. Drezek, and J. L. West, "Near-Infrared Resonant Nanoshells for Combined Optical Imaging and Photothermal Cancer Therapy," Nano Letters, vol. 7, no. 7, pp. 1929–1934, 2007. doi: http://dx.doi.org/10.1021/nl070610y.

CHAPTER 3

Nanoparticles

Nanoparticles are those particles that are in the range of 1-100nm. At these scales materials begin to exhibit different properties than those of bulk materials, which affect their chemical and physical behavior. These properties make NPs very attractive for innumerable applications, principally in the biomedical, optics and electronic fields.

Generally, NPs can be classified depending on their composition in organic and inorganic, or more specifically in fullerenes and carbon nanotubes, metals, ceramics, semiconductors or quantum dots, and polymers. Among them, there exists a special interest in noble metal NPs since they present a strong localized surface plasmon resonance (LSPR), which is a property characteristic of metal NPs that become ideal candidates for many applications.

3.1 Fabrication Methods

There exist two basic methods of NPs fabrication; the top down and the bottom up. The top down methods consist in obtain nanostructures by removing, reducing, subtracting or subdividing a bulk material. Among top down methods are lithography, ball milling, and laser ablation [1]. On the other hand, the bottom-up methods start from atoms, ions or molecules which are assembled to generate nanostructures. Some bottom-up methods are templating, chemical, electrochemical, sonochemical, thermal and photochemical reduction techniques [1, 2]. Both methods possess advantages and disadvantages. Top down methods can suffer of contamination, machine cost and complexity, material damage or heat dissipation, but offer high reproducibility and high production. Since most of the bottom up methods involve chemical processes, synthesis volume is typically small, also lack of stability, high monodispersivity of size

and morphology, and of total reproducibility. Nevertheless, these allow fabricating a great variety of NPs also intricate morphologies easily, without special equipment at low cost.

The most common bottom-up method, in particular for metal colloidal NPs fabrication is the chemical reduction. In this method a metal precursor is dissolved in a solvent with an organic surface capping agent, which enables the NPs to be stably dispersed in the solution. Then, the metal is reduced by adding a reducing agent or by raising temperature.

In this thesis the NPs used where fabricated (synthesized) by the seed mediated method, which allows fabrication of large spherical and non spherical NPs. In this method, seeds are usually fabricated by the chemical reduction method, in which a metal salt is reduced with a strong reducing agent, like sodium borohydride ($NaBH_4$) to obtain generally spherical NPs. These NPs serve as nucleation sites for the growth of the final NPs. The growth solution contains principally a gold salt, a weak reducing agent, such as ascorbic acid, and structure-directing additives. The gold salt is partially reduced by the reducing agent, and after addition of the seeds to the growth solution an autocatalytic reaction take place in the surface of the seeds producing the desired NPs. The size of the NPs can be tuned by modifying the amount of seeds added; larger particles can be obtained by reducing the seed quantity added to the growth solution.

3.2 Nanoparticle Properties

When materials are reduced from bulk to a nanometric size, interesting properties emerge, such as optical, electronic, magnetic, and structural. For example, iron oxide NPs in the presence of an external magnetic field present a large magnetic moment, which make them ideal contrast agents for magnetic resonance imaging (MRI). However, NPs presenting optical properties, such as LSPR, have principally investigated since they are very promising for many applications, mainly in the biomedical area, for instance, optical sensing exploits the intensity and change in LSPR peak position to detect binding events on NPs surfaces in order to examine biomolecules with high sensitivity at low cost. Also, due to LSPR, light absorption and scattering are strongly enhanced, 5 orders of magnitude more than most strongly absorbing organic dye

molecules and 6 orders of magnitude more than the emission of most strongly fluorescent molecules [3], making them excellent candidates as contrast agent for imaging modalities.

The optical property of LSPR is attributed only to metal NPs, and is important due to it strongly enhance the electromagnetic field in the surface of the NP. As consequence, all the radiative and nonradiative properties of metal NPs, such as absorption and scattering, are also enhanced; and light strongly absorbed is converted to heat quickly by a series of nonradiative processes.

The interest in metal NPs also lies in that they can be easily fabricated and tuned for a specific application just by modifying their shape and size. They can be also conjugated with antibodies, ligands, or drugs which make them useful as drug delivery agents [4], labeling agents [5], sensors [6], and contrast agents [7]. Other applications of NPs include enhanced nonlinearities [8], building blocks [9], photothermal therapy [10], and SERS [11]. Additionally, noble metals are resistant to corrosion and oxidation; and unlike dyes, metal particles are photostable and do not undergo photobleaching, allowing higher light excitation energies and longer probing times. Gold specifically presents excellent biocompatibility.

Surface plasmons are electromagnetic excitations of free electrons at the interface between a metal and a dielectric medium, and are described by evanescent electromagnetic waves. If the collective oscillation of free electrons is confined to a finite volume as with a metal NP, the corresponding plasmon is called **localized surface plasmon.**

Surface Plasmon Resonance (SPR) is an optical phenomenon arising from the coherent collective oscillation of the free electrons in the surface of a metal, resonating at a specific frequency, when they are disturbed by an electromagnetic wave from their equilibrium position. See fig. 3.1a

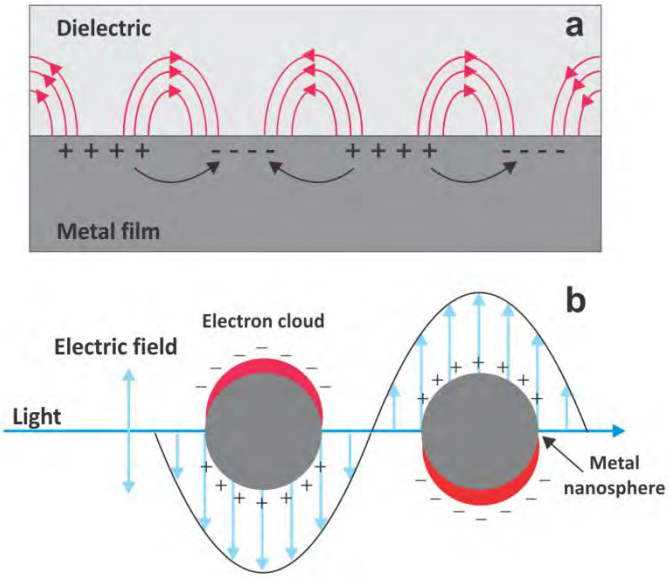

Fig. 3.1 a) propagating surface plasmons of a metal surface; b) localized surface plasmons of a metal nanosphere.

When a metal spherical particle interacts with a light field (see fig. 3.1b), and its size is much smaller than the wavelength of the light, the electromagnetic field of the light can cause the collective oscillation of the free electrons in the surface moving away from the particle in one direction and creating a dipole that can switch direction with the change in the electric field. When the frequency of the plasmon is approximately the same as the incident light a resonance condition is reached, leading to constructive interference and the stronger signal for the plasmon, it is the electromagnetic field intensity is enhanced on the particle surface. This effect is known as **LSPR**.

In few words LSPR occurs when an electromagnetic field drives the collective oscillation of the free electrons of a NP into resonance. The interactions of an electromagnetic wave with a NP can be described by solving the Maxwell equations. Exact solutions are possible only for special cases, such as the Mie theory; where Maxwell equations where solved for a sphere when a plane wave incident on the sphere and is surrounded by a dielectric medium, given the dielectric function of the metal sphere. Exact solutions have been also found for a concentric spherical shell, a spheroid and an infinite cylinder. For other particles with arbitrary geometrical shapes, it is

required to proceed by numerical calculations with some approximations to solve Maxwell equations.

LSPR depends principally on the intrinsic dielectric property of the metal, the dielectric medium, and the pattern of surface polarization. Therefore, any variation in the shape or size of the particle that yields a change in the surface polarization induces a change in the plasmon resonance. Taking this into account it is possible to tailor the LSPR of metal NPs by modifying their size and shape. Besides, the LSPR band is much stronger for NPs of noble metals, especially Au and Ag, than other metals.

The LSPR induces a strong absorption of the incident light, which can be measured using a UV-Vis absorption spectrometer. In the UV-visible absorption spectrum for metal NPs bigger than 2nm a strong and broad band is observed. This is called the surface plasmon band (SPB).

3.3 Concave Nanoparticles

Nanoparticles with typical geometrical shapes such as spheres, disks, cups, have been fabricated and used in a great variety of applications, the process of fabrication is widely known also how to tune their plasmon band according to a specific application. Generally, these types of NPs show a plasmon band in the visible range of the electromagnetic spectrum. However, some applications such as optical communications, or biomedical require enhanced properties in the NIR region. In different studies, it have been shown how optical properties, such as absorption and scattering of NPs highly depend on their size and shape. For example, El Sayed and others [12, 13], demonstrated that for spherical Au particles of 20nm, absorption is dominant. For particles of 40nm the scattering starts to show up, meanwhile for NPs of 80nm absorption and scattering contribute equally to the extinction, and for particles of 100nm and larger the effect of scattering is dominant. Thus, the scattering to absorption ratio increases dramatically for particles of larger size. Therefore, in photothermal applications small particles are preferred since they absorb almost all the incident light and then is efficiently converted to heat for destructing cells and tissues. On the other hand, larger particles are preferred for imaging applications, since they mainly scatter the incident light. These effects are reflected in the plasmon band, since as size

increases a red shift in the plasmon band is given, but at NP size of 100nm or larger, red shift almost disappear, instead a broadening in the plasmon band appears; to overcome this, and tune SPB to NIR and IR regions a change in the shape of NP needs to be done. Different studies have shown the influence of NP shape in LSPR [14, 15]. For example, for rods, it was observed that the absorption wavelength depends linearly of the aspect ratio, it is, when aspect ratio increases light scattering efficiency increases. Many other shapes have been fabricated and used which enhance optical properties and that can be tuned to NIR and IR regions, such as nanoshells, triangles, prisms, etc.

Last years, a new type of NPs has been actively investigated, since their fabrication, to their properties and applications. These are the NPs with concave surfaces or of high index facets [16]; Fig. 3.2 shown some of the NPs into this category. Within this category is the group of the known as branched or star NPs, which comprise since monopod, bipod tripod, tetrapod [17], to hyperbranched NPs [18], etc. In Fig.3.3 some NPs belonging to this category are shown.

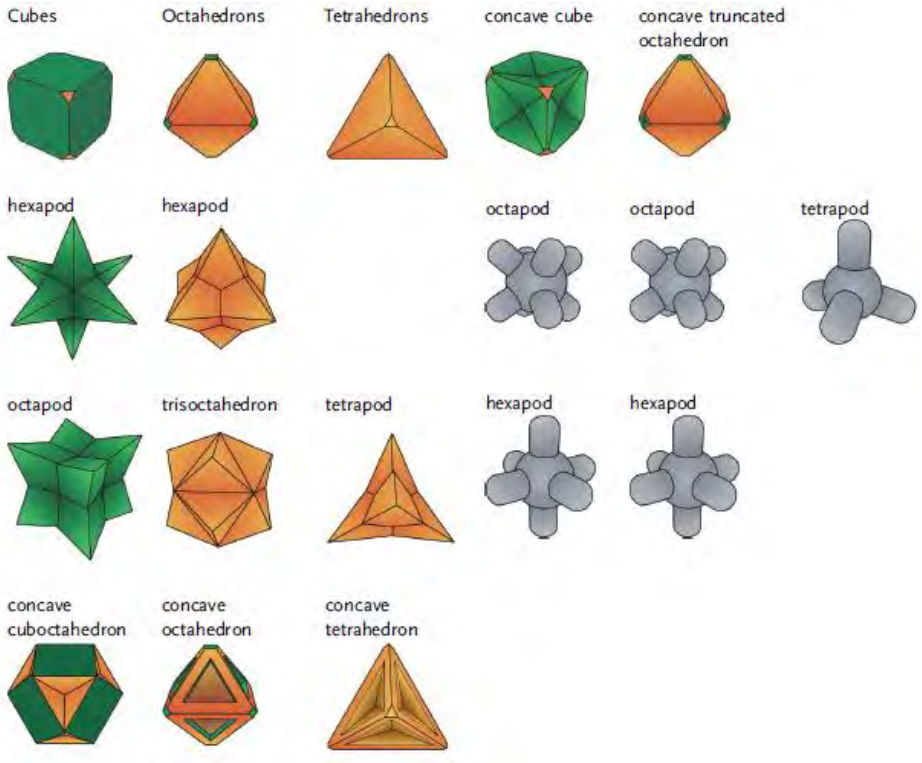

Fig. 3.2 Possible concave nanoparticles [16].

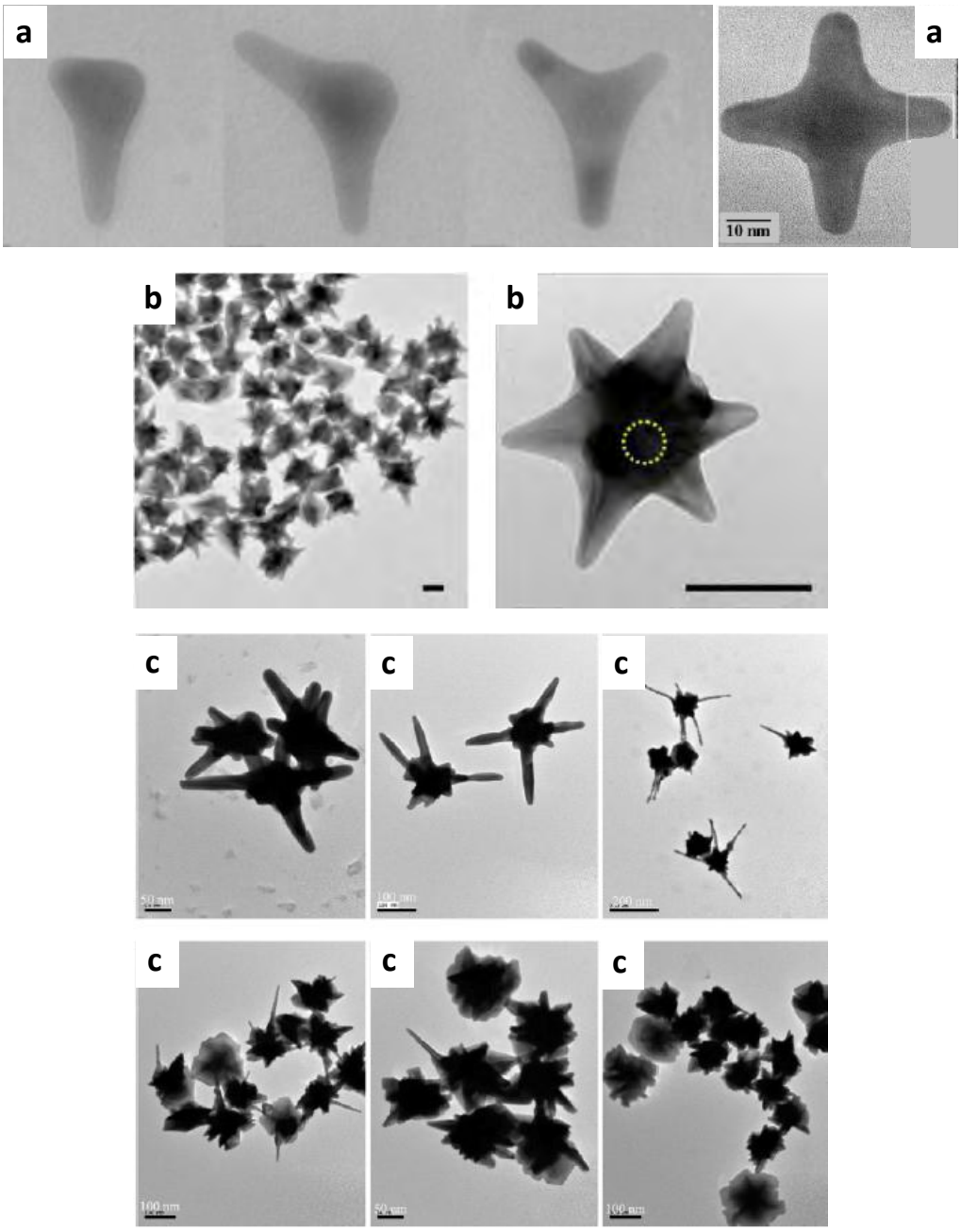

Fig. 3.3 Different branched or star nanoparticles. a) monopod, bipod, tripod, and tetrapod NPs [17]; b) Nanostars with magnetic cores [19]; c) Thorny NPs [20].

Concave nanoparticles are described as those NPs that present a negative curvature in their surface. For a two dimensional system, a concave structure can be defined as a polygon that

has at least one interior angle that is greater than 180 degrees. The same concept can be extended to a three dimensional system by focusing on the cross-sections. In general high index facets other than {100}, {110}, and {111} are involved in the construction of a concave surface [16]. It should be pointed out that nanostructures with branched arms on the surface naturally have concave regions on the surface [21, 22].

Concave and branched NPs are mainly obtained by inducing a directionally controlled overgrowth, or by site-specific dissolution. It can be consider that for both strategies the formation of concave NPs starts from convex NPs encased by a set of low index facets. In the directionally controlled overgrowth atoms or molecules are added so the seeds in order to form the particle. In The site-specific dissolution the polyhedral NP serves as template for site specific dissolution. Among the directionally controlled overgrowth methods is the seed mediated method, which was previously described and which is a very common method of fabrication for larger and anisotropic NPs.

The interest for NPs with this characteristic surfaces or shapes is due to their enhanced and additional properties compared with other morphologies. For instance, it has been shown that NPs with concave surfaces present enhanced properties than their convex counterpart [23]. Additionally, unlike other typical shapes of NPs fabricated principally of Au and Ag, concave and branched particles have also been fabricated of palladium (Pd), platinum (Pt), rhodium (Rh), alloys and combinations, since these metals present high catalytic and electrocatalytic activity, that combined with negative curvatures or high index facets enhance significantly these properties [23-25]. When an electromagnetic field excites the free electrons of a metal NP tip, a highly localized strong electric field is developed at these sharp tips or vertex with large curvatures, leading to large field enhancement in those regions. This is the reason for a very high activity in surface enhanced Raman spectroscopy (SERS) of these NPs [25, 26]. In this context, the application of sensitive SERS detection shows great promise as analytical platform especially in biological systems. The facility of fabrication, functionalization or bioconjugation, and tunabilty of NPs together with the strong LSPR, and enhanced scattering cross-sections make these particles very attractive for their use as contrast agents for NIR imaging applications. However, a challenge remains in the synthesis process, since the mechanism that involve the anisotropic growth of

these unusual shape NPs is not totally determined, restricting the control over the morphology. Specifically the challenges are determine the process to generate these anisotropies and how to stabilize it.

The two main works done for this thesis are related with the mentioned in the last lines. The first one is related with the desire of understand the growth process of NP with concave morphology like gold concave nanocubes, for which, the NPs growth kinetics was followed by the optical coherence tomography technique. The second one was to prove that branched NPs are good contrast agent for being used in the imaging modality of optical coherence tomography, which works in the NIR region.

References

[1] G. L. Horniak, H. F. Tibbals, J. Dutta, J. J. Moore "Introduction to Nanoscience & Nanotechnology," CRC press, 2009

[2] S. Eustis and M. A. El-Sayed, "Why gold nanoparticles are more precious than pretty gold: Noble metal surface plasmon resonance and its enhancement of the radiative and nonradiative properties of nanocrystals of different shapes," Chemical Society Reviews, vol. 35, pp. 209–217, 2006. doi: http://dx.doi.org/10.1039/B514191E.

[3] P. K. Jain, K. S. Lee, I. H. El-Sayed, and M. A. El-Sayed, "Calculated absorption and scattering properties of gold nanoparticles of different size, shape, and composition: applications in biological imaging and biomedicine," The Journal of Physical Chemistry B, vol. 110, no. 14, pp. 7238-7248, 2006. doi: http://dx.doi.org/10.1021/jp057170o.

[4] P. Ghosh, G. Han, M. De, C. K. Kim, V. M Rotello, "Gold nanoparticles in delivery applications," Advanced Drug Delivery Reviews, vol. 60, no. 11, pp. 1307–1315, 2008. doi: http://dx.doi.org/10.1016/j.addr.2008.03.016.

[5] R. Singh, H. S. Nalwa, "Medical Applications of Nanoparticles in Biological Imaging, Cell Labeling, Antimicrobial Agents, and Anticancer Nanodrugs," Journal of Biomedical Nanotechnology, vol. 7, no. 4, pp. 489-503, 2011, doi: http://dx.doi.org/10.1166/jbn.2011.1324.

[6] K. Saha, S. S. Agasti, C. Kim, X. Li, and V. M. Rotello, "Gold Nanoparticles in Chemical and Biological Sensing," Chemical Reviews, vol. 112, no. 5, pp. 2739–2779, 2012, doi: http://dx.doi.org/10.1021/cr2001178.

[7] M. A. Hahn, A. K. Singh, P. Sharma, S. C. Brown, B. M. Moudgil, "Nanoparticles as contrast agents for in-vivo bioimaging: current status and future perspectives," Analytical and Bioanalytical Chemistry, vol. 399, no. 1, pp. 3-27, 2011. doi: http://dx.doi.org/10.1007/s00216-010-4207-5.

[8] X. Huang, W. Qian, I. H. El-Sayed and M. A. El-Sayed, "The potential use of the enhanced nonlinear properties of gold nanospheres in photothermal cancer therapy," Lasers in Surgery and Medicine, vol. 39, no. 9, pp. 747–753, 2007. doi: http://dx.doi.org/10.1002/lsm.20577.

[9] H. Zhang, I. Hussain, M. Brust and A. I. Cooper, "Emulsion-Templated Gold Beads Using Gold Nanoparticles as Building Blocks," Advanced Materials, vol. 16, no. 1, pp. 27–30, 2004. doi: http://dx.doi.org/10.1002/adma.200306153.

[10] X. Huang, P. K. Jain, I. H. El-Sayed, M. A. El-Sayed, "Plasmonic photothermal therapy (PPTT) using gold nanoparticles," Lasers in Medical Science, vol. 23, no. 3, pp. 217-228, 2008. doi: http://dx.doi.org/10.1007/s10103-007-0470-x.

[11] L. Lu, G. Sun, H. Zhang, H. Wang, S. Xi, J. Hu, Z. Tian and R. Chen, "Fabrication of core-shell Au-Pt nanoparticle film and its potential application as catalysis and SERS substrate," Journal of Materials Chemistry, vol. 14, no. 6, pp. 1005-1009, 2004, doi: http://dx.doi.org/10.1039/B314868H.

[12] P. K. Jain, K. S. Lee, I. H. El-Sayed, M. A. El-Sayed, "Calculated absorption and scattering properties of gold nanoparticles of different size, shape, and composition: applications in biological imaging and biomedicine," The Journal of Physical Chemistry B, vol. 110, no. 14, pp. 7238–7248, 2006. doi: http://dx.doi.org/10.1021/jp057170o.

[13] K. S. Lee, M. A. El-Sayed, "Dependence of the enhanced optical scattering efficiency relative to that of absorption for gold metal nanorods on aspect ratio, size, end-cap shape and medium refractive index," The Journal of Physical Chemistry B, vol. 109, no. 43, pp. 20331–20338, 2005. doi: http://dx.doi.org/10.1021/jp054385p.

[14] C. L. Nehl and J. H. Hafner, "Shape-dependent plasmon resonances of gold nanoparticles," Journal of Materials Chemistry, vol. 18, pp. 2415-2419, 2008, doi: http://dx.doi.org/10.1039/B714950F.

[15] C. Noguez "Surface Plasmons on Metal Nanoparticles: The Influence of Shape and Physical Environment," The Journal of Physical Chemistry C, vol. 111, no. 10, pp. 3806–3819, 2007, doi: http://dx.doi.org/10.1021/jp066539m.

[16] H. Zhang, M. Jin, and Y. Xia, "Noble-Metal Nanocrystals with Concave Surfaces: Synthesis and Applications," Angewandte Chemie International Edition, vol. 51, no. 31, pp. 7656–7673, 2012. doi: http://dx.doi.org/10.1002/anie.201201557.

[17] S. Chen, Z. L. Wang, J. Ballato, S. H. Foulger, and D. L. Carrol. "Monopod, Bipod, Tripod, and Tetrapod Gold Nanocrystals," Journal of the American Chemical Society, vol. 125, no.52 pp. 16186-16187, 2003. doi: http://dx.doi.org/10.1021/ja038927x.

[18] A. G. Kanaras, C. Sönnichsen, H. Liu, and A. P. Alivisatos, "Controlled Synthesis of Hyperbranched Inorganic Nanocrystals with Rich Three-Dimensional Structures," Nano Letters, vol. 5, no. 11, pp. 2164-2167, 2005. doi: http://dx.doi.org/10.1021/nl0518728.

[19] Q. Wei, H. M. Song, A. P. Leonov, J. A. Hale, D. Oh, Q. K. Ong, K. Ritchie, and A. Wei, "Gyromagnetic Imaging: Dynamic Optical Contrast Using Gold Nanostars With Magnetic Cores," Journal of the American Chemical Society, vol. 131, no. 28, pp. 9728–9734, 2009, doi: http://dx.doi.org/10.1021/ja901562j.

[20] H. Yuan, W. Ma, C. Chen, J. Zhao, J. Liu, H. Zhu, and X. Gao, "Shape and SPR Evolution of Thorny Gold Nanoparticles Promoted by Silver Ions," Chemistry of Materials, vol. 19, no. 7, pp. 1592-1600, 2007. doi: http://dx.doi.org/10.1021/cm062046i.

[21] B. Lim, Y. Xia, "Metall-Nanokristalle mit hochverzweigten Morphologien," Angewandte Chemie, vol. 123, no. 1, pp. 78-87, 2011. doi: http://dx.doi.org/10.1002/ange.201002024.

[22] B. Lim, Y. Xia "Metal Nanocrystals with Highly Branched Morphologies," Angewandte Chemie International Edition, vol. 50, no. 1, pp. 76–85, 2011. doi: http://dx.doi.org/10.1002/anie.201002024.

[23] M. Jin, H. Zhang, Z. Xie, and Y. Xia, "Palladium Concave Nanocubes with High-Index Facets and Their Enhanced Catalytic Properties," Angewandte Chemie International Edition, vol. 50, no.34, pp. 7850-7854, 2011. doi: http://dx.doi.org/10.1002/anie.201103002.

[24] L. Zhang, D. Chen, Z. Jiang, J. Zhang, S. Xie, Q. Kuang, Z. Xie, and L. Zheng, "Facile Syntheses and Enhanced Electrocatalytic Activities of Pt Nanocrystals with {hkk} High-Index Surfaces," Nano Research, vol. 5, no. 3, pp. 181–189, 2012, doi: http://dx.doi.org/10.1007/s12274-012-0198-1.

[25] L. F. Zhang, S. L. Zhong, and A. W. Xu, "Highly Branched Concave Au/Pd Bimetallic Nanocrystals with Superior Electrocatalytic Activity and Highly Efficient SERS Enhancement," Angewandte Chemie, vol. 125, pp. 673 –677, 2013, doi: http://dx.doi.org/10.1002/ange.201205279.

[26] X. Xia, J. Zeng, B. McDearmon, Y. Zheng, Q. Li, Y. Xia, "Silver nanocrystals with concave surfaces and their optical and surfaceenhanced raman scattering properties," Angewandte Chemie International Edition, vol. 50, pp. 12542–12546, 2011, doi: http://dx.doi.org/10.1002/anie.201105200.

CHAPTER 4

Growth Kinetics of Concave Nanocubes Studied by Optical Coherence Tomography

4.1 Introduction

It is known that nanocrystals (NCs) exhibit fascinating optical properties that can be modified simply by setting a control of parameters such as composition, size, shape or their environment [1]. The use and applications of NCs have been extended in different industrial and scientific areas, for instance, electronics, catalysis or biomedical imaging [2, 3]. In the last decade, shape control of noble metal NPs has received a lot of attention, especially for those morphologies presenting concave surfaces. These NPs are interesting because their properties become suitable for being used in diverse applications related to catalysis, plasmonics, surface-enhanced spectroscopy, or as contrast agents in biomedical imaging [4, 5]. The fabrication of NCs with concave surfaces is not an easy task due to the fact that concave NPs are not favored by thermodynamics because of its high energy. Although diverse works have reported how to stabilize concave NPs [6, 7], a simple chemical route of a high yield synthesis (size and morphology) is still a challenge. Control over size and morphology of the produced particles cannot be a priori predicted because different factors affect the system: the nature of solvents, the stabilizers and reducers concentration, as well as temperature and humidity. Selection of the synthesis conditions to grow NCs of a required size and morphology is usually time consuming; consequently, additional information on the growth kinetics would be valuable to have better control.

Microscopy techniques such as transmission electron microscopy (TEM), scanning electron microscopy (SEM) and atomic force microscopy (AFM) have been used for analyzing the growth of NPs by their direct observation [8-11]. Similarly, scattering and spectroscopic techniques have

been used for monitoring the growth kinetics of phase transformation such as: small-angle X-ray scattering (SAXS) [12, 13], fast single-particle spectroscopy (fastSPS) [14], quick X-ray absorption fine structure (QXAFS) [15], and ultra violet-visible (UV-Vis) absorption spectroscopy [16-18]. Among the above techniques, UV-Vis absorbance spectroscopy is the most recurrent tool for studying the growth kinetics as a result of its simplicity and easy access. NCs of noble metals larger than 2 nm exhibit an optical absorption in the visible range due to the surface plasmon resonance band. A change in their absorbance intensity can be correlated with changes in concentration and a shift in the wavelength of the maximum absorption can be correlated with changes of size or morphology [19, 20]. The main advantages of UV-Vis absorbance spectroscopy is that the study can be done in situ and in real time without modifying the environmental condition of the growth.

Techniques like optical coherence tomography (OCT) measure the echo time delay of backscattered and backreflected optical signals from different layers within the sample with micrometer resolution, being able to acquire 1D (A-scan), 2D (B-scan) or 3D (C-scan) images. Due to its high sensitivity, it is possible to observe the position and movement of scattering particles during NP growth. The ability of OCT to detect NP scattering makes it viable to monitor the growth kinetics of colloidal metals without modifications of the experimental set up; which has not been reported previously.

This chapter describes the study of the growth kinetics of two syntheses of concave nanocubes (CNCBs) of different sizes by the OCT technique. Additionally, UV-Vis spectroscopy and dynamic light scattering (DLS) measurements were carried out to compare the results with those obtained by OCT.

4.2 Experimental Section

Synthesis of Nanoparticles

We fabricated CNCBs modifying slightly the seed-mediated method reported by Zhang et al. [21]. In this type of syntheses a seed solution is required to initiate the growth of NPs. Our procedure to fabricate seeds and CNCBs is as follows.

Seeds: In a typical synthesis, seeds are prepared in the following way: 260 µl of $HAuCl_4$ (10 mM) are added to a 10 ml of cetyltrimethylammonium chloride (CTAC) solution (0.1 M) and to initiate the seed growth, 700 µl of freshly prepared ice-cold $NaHB_4$ solution (10 mM) are added under continuous stirring and left for two min to finally be left undisturbed for 2h. Figure 4.1a shows the final solution of seeds, which has a pale brown color. Figure 4.1b shows the corresponding UV-Vis absorption spectrum of the seeds, where a main peak at around 510 nm can be appreciated, which means that the seed NPs have a size smaller than 10nm.

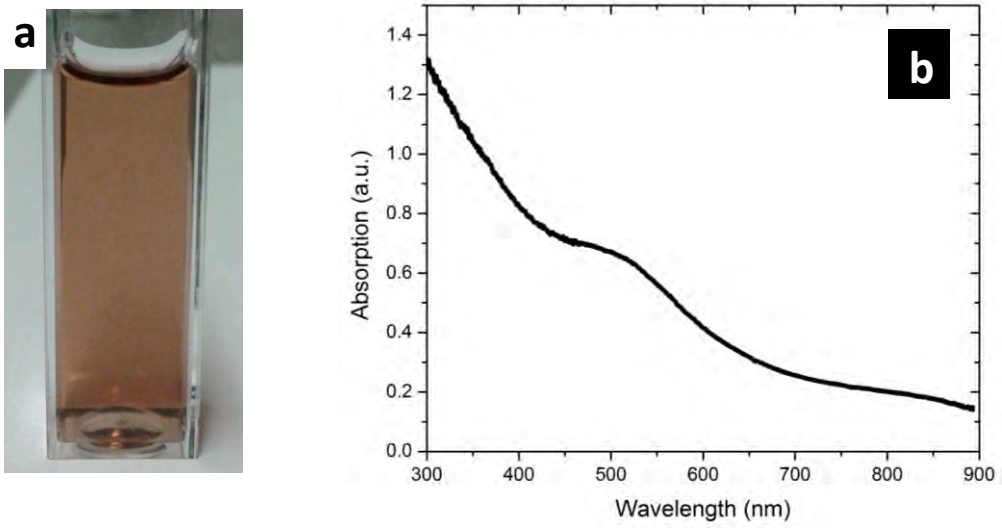

Fig. 4.1 a) Image of the final seed solution; b) UV-Vis absorption spectrum of the seeds.

Concave nanocubes: A growth solution is prepared by consecutively adding: 10 ml of CTAC (0.1 M), 500 µl of $HAuCl_4$ (10 mM), 50 µl of $AgNO_3$ (10 mM), 200 µl of HCl (1 M), 125 µl of ascorbic acid (0.1 M). To initiate the growth of the NPs 50 µl of seed solution diluted 1:100 were added to the growth solution to obtain C1. To produce large particles C2, 10 µl of the diluted seed solution were added to the growth solution.

Instrumentation and Measurements

All the instruments used were previously aligned and calibrated before initiating the data acquisition for each set of measurements.

UV-Vis Spectroscopy. A portable spectrometer Ocean Optics USB 4000 UV-Vis, with a spectral range of 200 to 890 nm, was used to acquire absorption spectra each 30 s after the seeds were added to the growth solution. For monitoring the syntheses growth, plastic cuvettes of 5 mm path length were used. After the syntheses finished, a spectrophotometer Perkin Elmer Lambda 900 was used to obtain absorption spectra from 350nm to 1 350 nm. For recording the UV-near infrared (NIR) absorption spectra quartz cuvettes of 1 cm path length were used.

Optical Coherence Tomography (OCT). A Thorlabs Swept Source OCT system with a central wavelength at 1 325 nm was used to acquire B-scan images each 5 s after the seeds were added to the growth solution. To monitor the growth, 3 ml of the solutions were taken into plastic cuvettes of 1 cm path length. The images acquired were of 512x512 pixels, and an area of 2x0.66 mm for each image was selected to be analyzed. Figure 4.2 shows how the synthesis was being monitoring at the same time with the OCT system and with the UV-Vis spectrometer. In the left hand image, the OCT system and the colloid of NPs in the plastic cuvette, which is into the cuvette holder of the UV-Vis spectrometer (Stellarnet), are observed. The right hand image shows a general perspective of the system acquiring the OCT and spectrometer data. Also, the computer monitors show the simultaneous acquisition of the OCT (B-scan image) and spectrometer (UV-Vis absorption spectra) information.

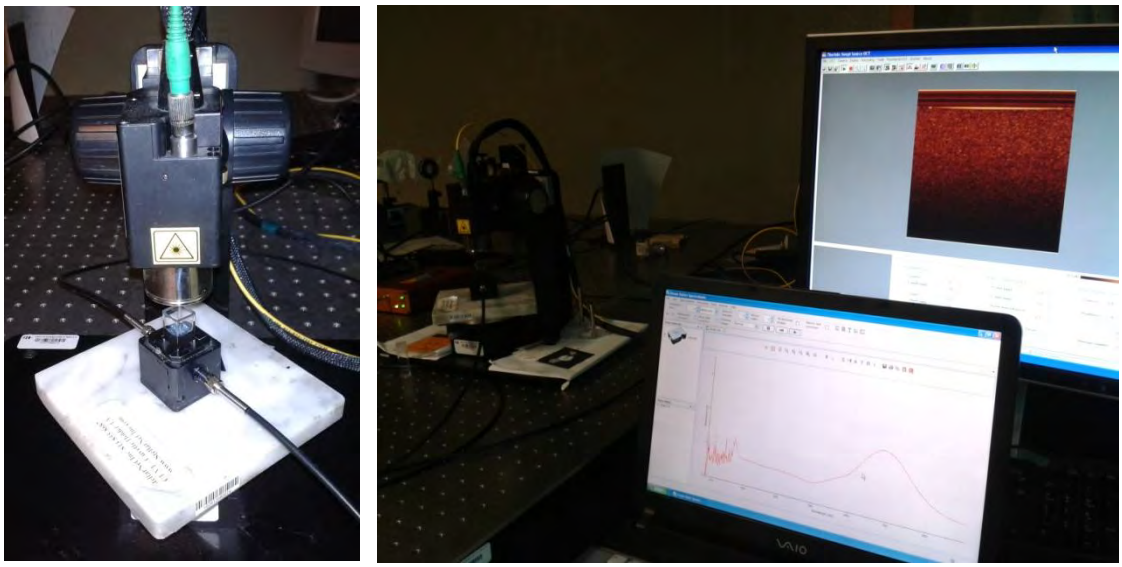

Fig. 4.2 Images of the OCT and spectrometer systems while measurements were being performed.

Dynamic Light Scattering (DLS). The mean size and size distribution of NPs in the colloids were measured using a Zetasizer Nano ZS system (Malvern Instruments). Measurement parameters were as follows: laser wavelength 633 nm (He-Ne), angle of scattering 173^{o}, temperature 25 ^{o}C, medium viscosity 0.89 mPas, and refractive index of the medium 1.33 (water). Samples were collocated into 1 cm path length plastic cuvettes. DLS data were recorded at intervals of 20 s approximately in order to follow the full progress of the nanocube growth kinetics.

Transmission Electron Microscopy (TEM). CNCBs were characterized in morphology and size with a TEM (Philips, MORGAGNI 268). To determine the NPs mean size, several images were measured using the ImageJ software 1.42q (Wayne Rasband National Institutes of Health, USA).

4.3 Results and Discussion

As mentioned in the previous section, growth kinetics of two syntheses of CNCBs was followed by three methods: OCT, UV-Vis spectroscopy, and DLS. Figure 4.3a, b shows the recorded UV-Vis spectra of the growth kinetics for solutions C1 and C2, respectively. For simplicity, only some spectra at selected times are plotted. In Fig. 4.3, it can be observed that at minute 2, both colloids show zero absorbance in all the spectral range, whereas at minute 5, colloid C1 displays an increase in the absorbance value (0.1 OD) at the wavelength of maximum absorbance (665 nm). In addition, in C1, a slightly defined peak appears while sample C2 does not exhibit a significant increase in its absorbance at the same time. A faster growth of sample C1 was observed from minute 5 to minute 16, then the growth becomes slow reaching a steady state at around the minute 25; this stage means that the synthesis has almost ended. For the case of C2, the region of fast growth was observed from minute 13 to minute 28, and a slower and longer time of growth can be observed, reaching the steady state at minute 40. During the growth of the nanocubes the plasmon band suffered a bathochromic shift; the wavelength of the maximum absorbance of C1 started at 665 nm and finished at 673 nm, whereas for C2, it started at 699 nm and finished at 708 nm, and therefore the corresponding displacements are 8 and 9nm, respectively. NP concentration at final stage should be ideally equal to seed concentration, also absorbance is proportional to NP concentration; consequently, C1 shows a higher absorbance than C2 at the final stage of the syntheses, which is in agreement with our experimental values.

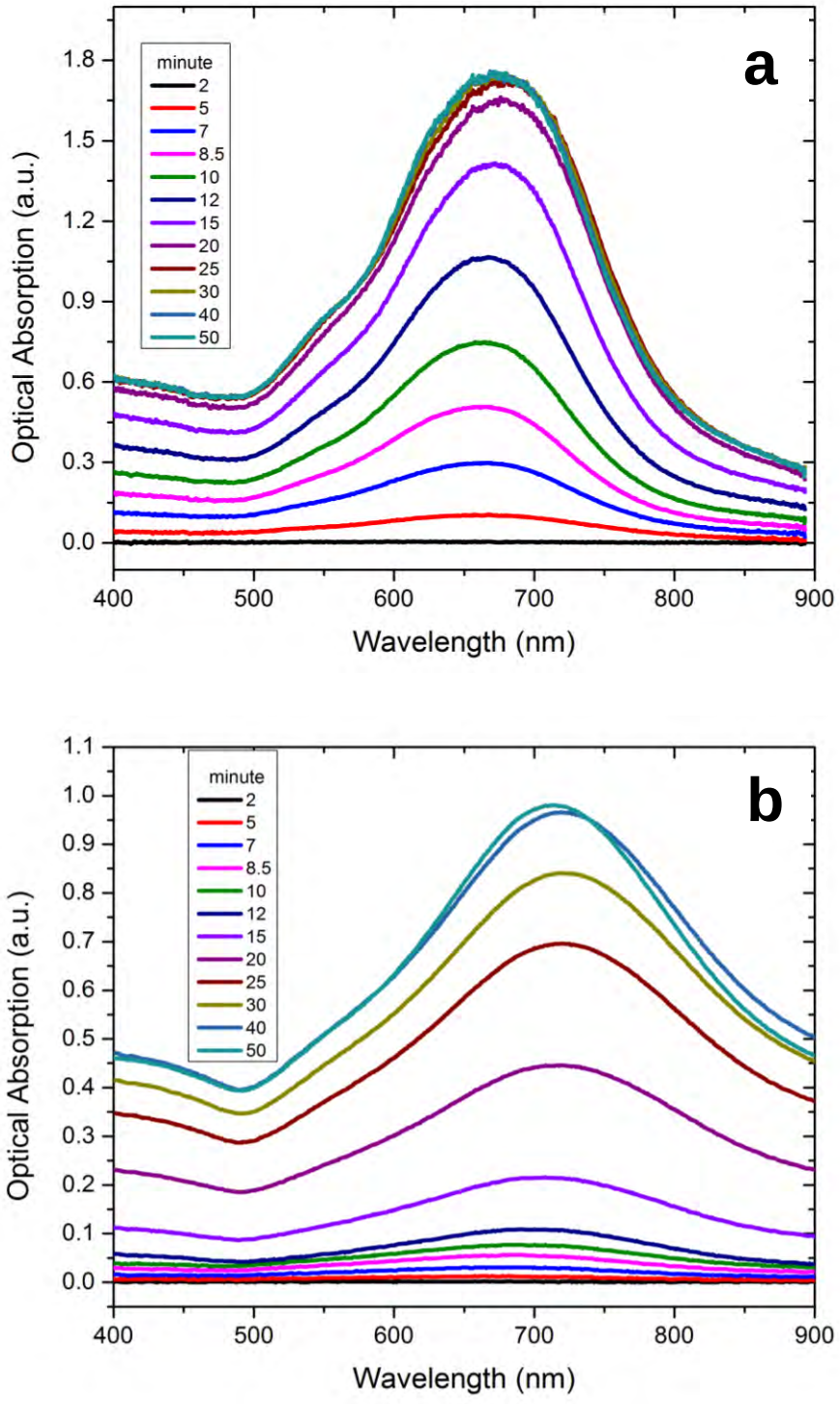

Fig. 4.3 UV-Vis absorption spectra at different times during NPs growth for: a) C1; b) C2.

Additionally to an increase in the absorption spectrum, visually, a change in the color of the colloids can be observed. The initial solution is transparent, and as times goes the solution acquire coloring. Figure 4.4 shows the images of the colloid of the synthesis C1 at minute 3, 5, 7, 8.5, 10, 12, 15, and 20, respectively for a-h. It is observed that at minute 3 the solution presents an almost imperceptible light blue tone, at minute 5, a very light blue tone is observed, which continues increasing until reach a dark blue tone. It can be also noticed that before minute 12 the colloid was partially transparent, whereas in the next images the solution looks totally dark; being this dark blue the final color of the synthesis C1. The observing increase in coloring as time increases is also a signal of the evolution of NP growth. As that seen in the absorption spectra, for synthesis C1 the period of fast growth is from minute 5 to minute 16, as is seen in the images of the colloids, Fig. 4.4 b-g. Figure 4.4 l-q shows the images for the colloid C2. In this case the growth is slower than in synthesis C1. Additionally, NP size influence the color of the colloid, thus, as NPs in C2 are bigger than NPs in C1, the final synthesis of C2 shows a blue-gray color; also, concentration in C1 is higher than in C2. In the images of the synthesis C2, it is observed that there are no important changes in the synthesis color until minute 12. From minute 12 to 25 the major changes are present, which agree with the period of fast growth observed in the absorption spectra, minute 13 to 28. It is also observed that the final color of the colloid C2 become most transparent than the colloid at minute 30. This difference is due to the synthesis at minute 30 is not finished and particle size is less than the final NP size.

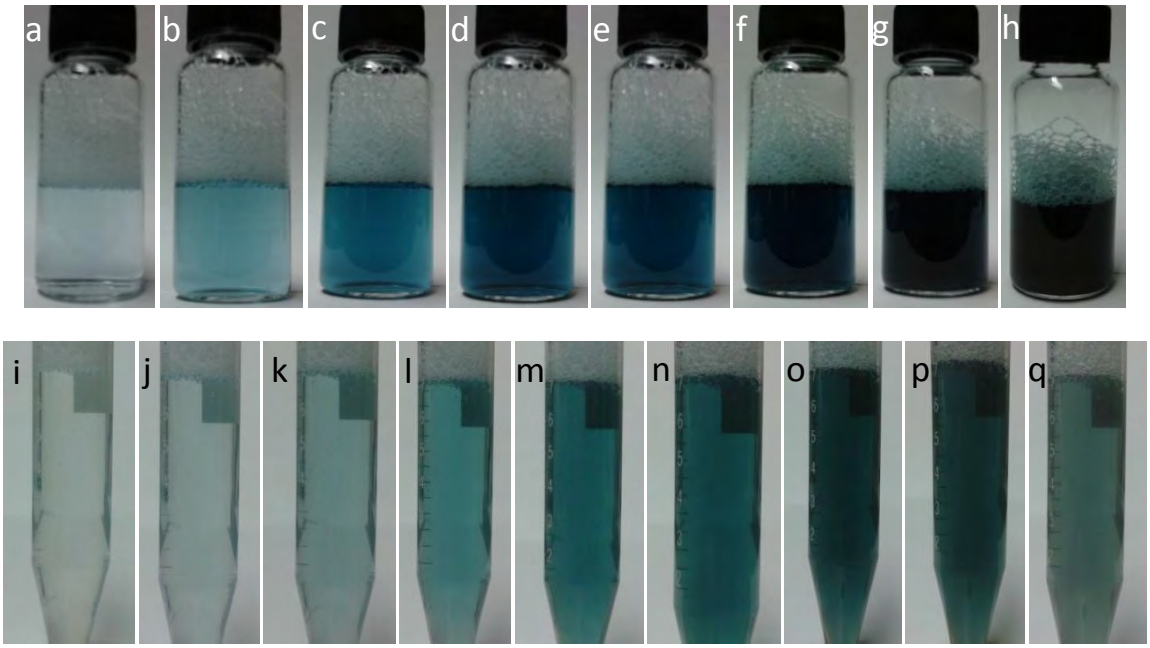

Fig. 4.4 a-h Images of the colloid of synthesis C1 at minute 3, 5, 7, 8.5, 10, 12, 15, and 20, respectively. i-q Images of the colloid of synthesis C2 at minute 5, 7, 10, 12, 15, 20, 25, 30, and 40, respectively.

Once the syntheses finished, UV-NIR absorption spectra were recorded from 350 to 1 350 nm. The absorption spectrum of solution C1 shows the characteristic narrow band of CNCBs, with a low absorbance in the NIR region. The spectrum of sample C2 also displays the characteristic band of CNCBs, but in this case, a strong scattering contribution in the NIR region is present (see Fig. 4.5a).

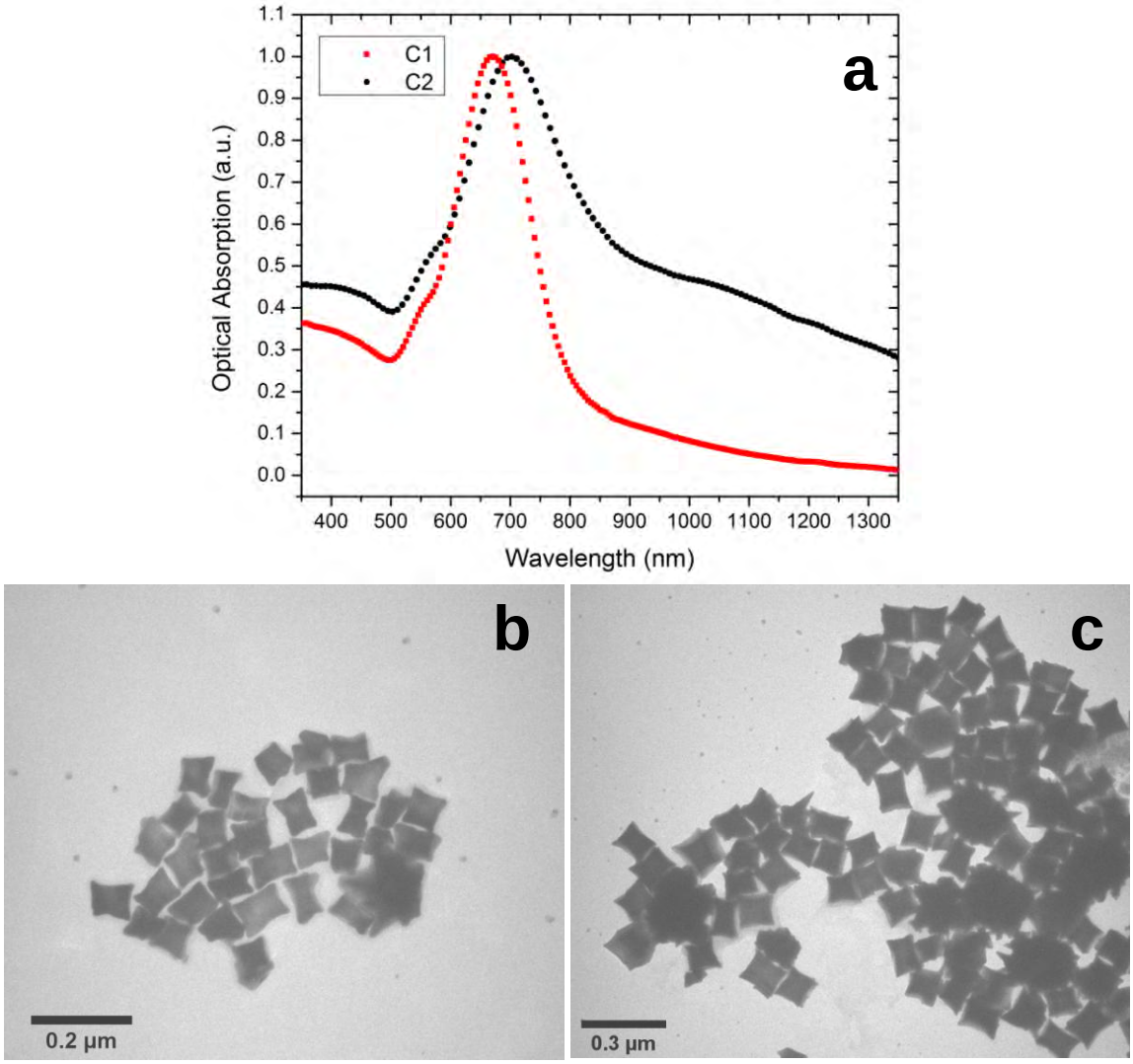

Fig. 4.5 a) Final UV-Vis absorption spectra of CNCBs recorded in the spectral range of 350 to 1350nm. Transmission electron microscopy images of CNCBs of: b) 72±10 nm mean length side (synthesis C1) and c) 108±14nm mean length side (synthesis C2).

The final product of both syntheses was characterized by TEM images. Figure 4.5b, c shows the corresponding TEM images for C1 and C2, from which it was confirmed that the produced NPs have concave cube morphology. After we analyzed several images, the mean length side of NPs measured was 72±10 nm for C1 and 108±14 nm for C2. In the TEM image of sample C2, some branched NPs (NPs with tips) appear. This kind of particles are produced due to an overgrowth of the cubes and have the characteristic that are very efficient scattering radiation at

the visible and infrared regions. In a previous work [5], we reported that these NPs can be useful as contrast agent for OCT imaging since they exhibit strong optical scattering.

OCT is a very sensitive technique to detect changes in the optical properties of NPs, mainly because it monitors the backreflected or backscattered light. The synthesis of CNCBs was followed in situ using the OCT technique from the begging to the end. Figure 4.6 a-g shows OCT B-scan images of synthesis C1, while Fig. 4.6 h-n of synthesis C2. These images correspond to the growth kinetics at minutes 5, 10, 15, 20, 30, 40, and 50, respectively for both syntheses. An increment in the scattering intensity is observed as time increases in both cases; nonetheless, C1 exhibited a stronger intensity compared with C2 during the first minutes. It is because of CNCBs of C1 grow faster, thus, for instance, at minute 15 the growth process for C1 was very advanced contrary to the C2 growth process, in consequence C1 have more NPs formed than C2, which causes the scattering. Whereas, at minute 30, the scattering looks a little higher for synthesis C2; at this time the synthesis C1 had already ended, and synthesis C2 has a considerable advance in the synthesis. At minute 50 both syntheses have already ended and the scattering of synthesis C2 is higher than the scattering of C1; even when NP concentration in C2 is lower than in C1. This happened because C2 produced particles of bigger size than C1; thus, they scatter more than the small particles. Figure 4.6 o shows a B-scan image of a sample of water. This image was used as reference in the contrast enhancement calculations. The bright line at the top is the air-water interface.

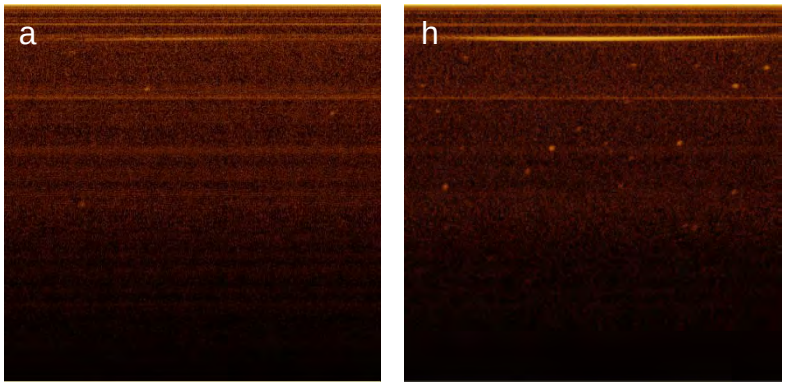

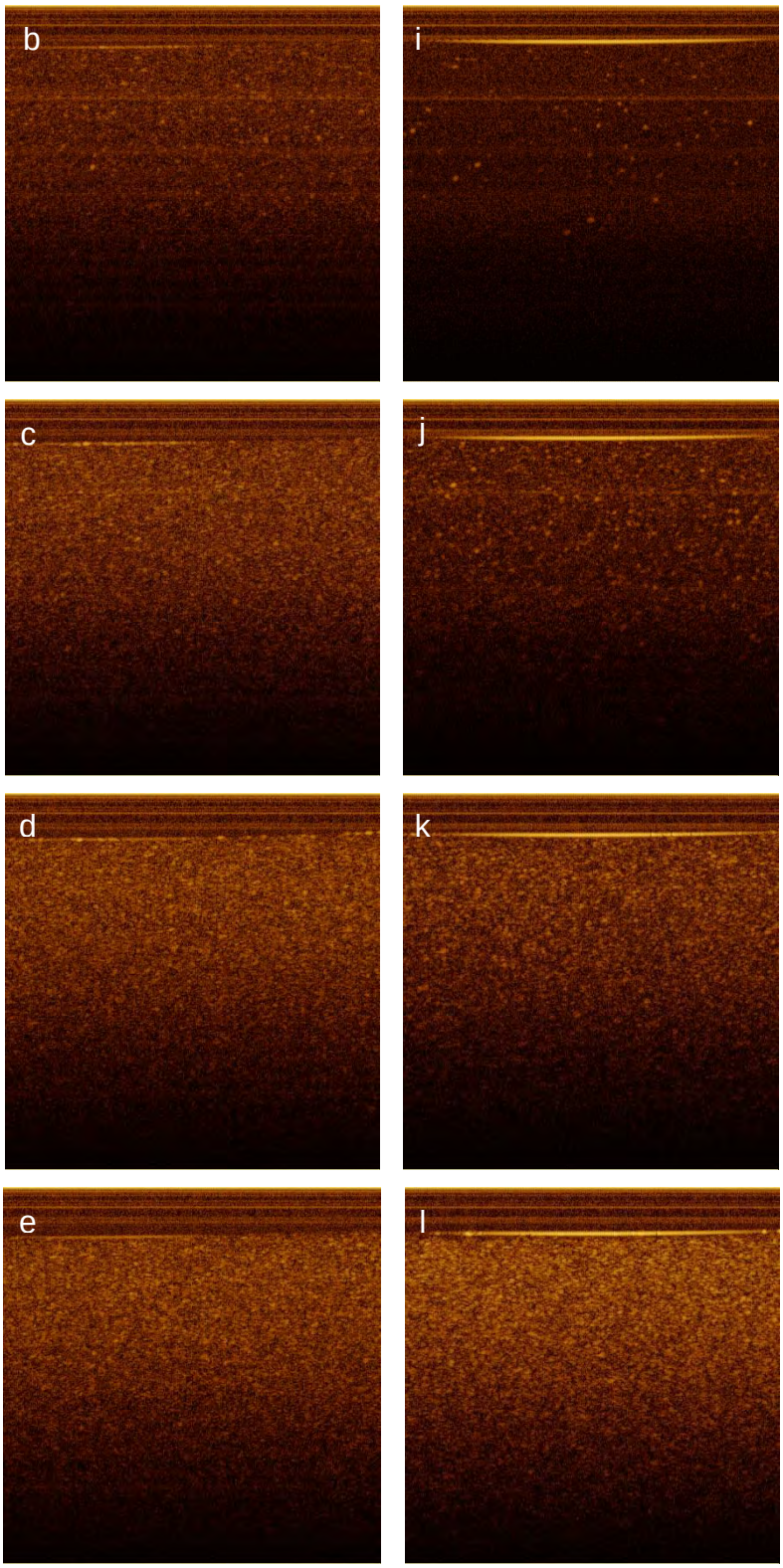
b
i
c
j
d
k
e
l

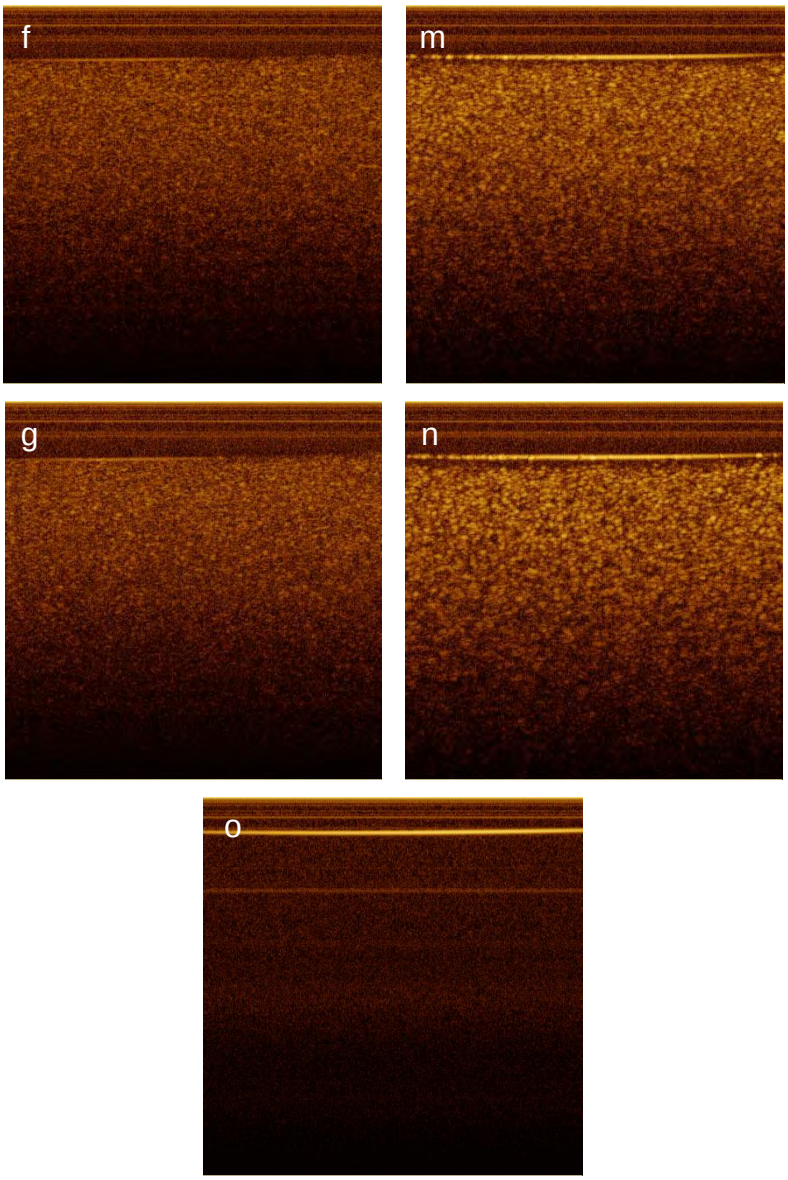

Fig. 4.6 OCT B-scan images for : a-g) C1 at minute 5,10,15,20,30,40 and 50, respectively; h-n) C2 at minute 5,10,15,20,30,40 and 50, respectively; o) water sample.

The full progress of the syntheses of CNCBs was followed by OCT recording B-scan images each 5 s. From each one of these images, it is possible to obtain an average intensity profile by averaging all the columns of the image, yielding an A-scan profile (intensity as depth function), which can be compared to acquire absorption spectra. Figure 4.7a, b shows the corresponding average A-scans for C1 and C2, respectively. OCT profiles show the backscattering behavior of the colloids at different depths. It can be noticed that at the beginning of the syntheses, the A-scan

profile for C1 displays higher intensity than C2; this is because there are more NPs formed in C1 than in C2; therefore, the scattering is higher for C1. However, after minute 25, the scattering intensity becomes higher for C2 because at this time, there is enough quantity of formed NPs in C1; remember that particles of higher size scatter more. It is also observed that C2 took more time than C1 to finish, similar to that seen in UV-Vis spectroscopy.

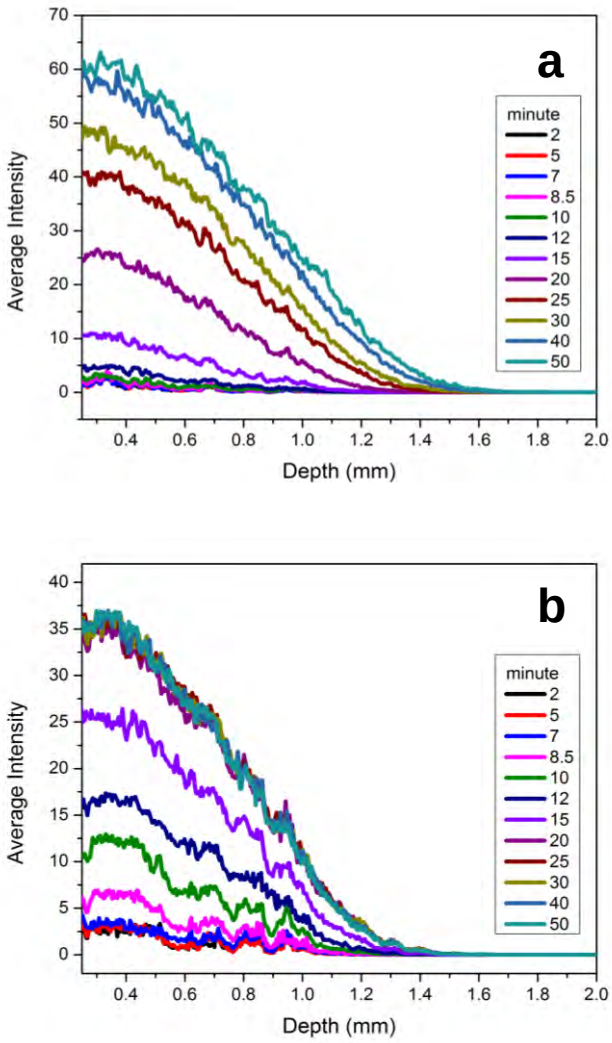

Fig. 4.7 Average intensity profiles at different times during nanoparticles growth for: a) C1; b) C2.

In order to plot the backscattered intensity as a function of time, we calculated the contrast enhancement (***S$_I$***) of each B-scan image using the following equation:

$$S_I = 10 \log_{10}(I_S / I_R), \tag{4.1}$$

where I_S is the average pixel intensity of the area of interest and I_R is the average pixel intensity of the reference area. The OCT reference image area was recorded using a sample of Millipore water. The values of contrast enhancement were plotted as time function in order to obtain a growth kinetic plot. In the case of UV-Vis spectroscopy, the maximum absorption values of surface plasmon resonance of the recorded spectra were plotted as time function to obtain a growth kinetic plot.

UV-Vis and OCT growth kinetics

According to the general theory of NCs, the growth kinetics process in solution is evolved mainly by the nucleation and growth processes. The NC growth can be done by the process of Ostwald Ripening (coarsening) or by the lately proposed theory of aggregative growth, where small primary NPs aggregate and then coalescence to produce larger NCs [22-24]. In either case, a sigmoidal profile is observed when NP volume is plotted as a function of time. The classical Kolmogorov-Johnson-Mehl-Avrami (KJMA) is the more used model to study the nucleation and the growth of phase transformation [25-28], which is given in Eq. 4.2, having two fitting parameter, a growth rate parameter ***k*** and an Avrami exponent ***n***.

$$A, S = C\left(1 - e^{(k\,t)^n}\right) \tag{4.2}$$

A or ***S,*** in our case, represents the absorbance of surface plasmon band or the contrast enhancement (by scattering), which can be related to the volume fraction of the NPs grown in the solution as a function of time, ***t***, and ***C*** is a proportionality constant.

Absorbance and contrast enhancement as time function were normalized before fitting calculations. Figure 4.8 shows the normalized plots, points for C1 and squares for C2. A sigmoidal behavior is observed for the growth kinetics. Three regions in the plots are observed, which are defined as a slow growth, then a fast growth (accelerated process), and finally a decelerating process to get the steady state. These curves clearly show that C1 grew faster than C2. A high stability was observed for C1 in both plots, whereas for C2, in the UV-Vis spectroscopy plot, a slightly decrease in the signal is present after minute 40 which is a consequence of NP precipitation. From this observation, it could be assumed that UV-Vis spectroscopy has a good sensitivity to detect small changes of surface plasmon resonance produced by NP precipitation, but OCT seems to not be very sensible at these changes since it did not show a decrease of the signal after minute 40 and the curve seems to be well defined from minute 15 to the end. On the other hand, OCT has a high sensitivity to detect the presence of few NPs, as can be seen in the OCT images corresponding to the minute 5, Fig. 4.6a, g. As a consequence of this sensitivity the contrast enhancement during the first minutes is different to zero. The origin of the high sensitivity of OCT comes from the interferometric measurements since the interferometer detects the field rather than the intensity of light [29]. Sensitivities of 10^{10} and higher have been reported which depends linearly on source power. For this reason, the contrast enhancements can be detected since the beginning of the kinetics, even when NP concentration is very low.

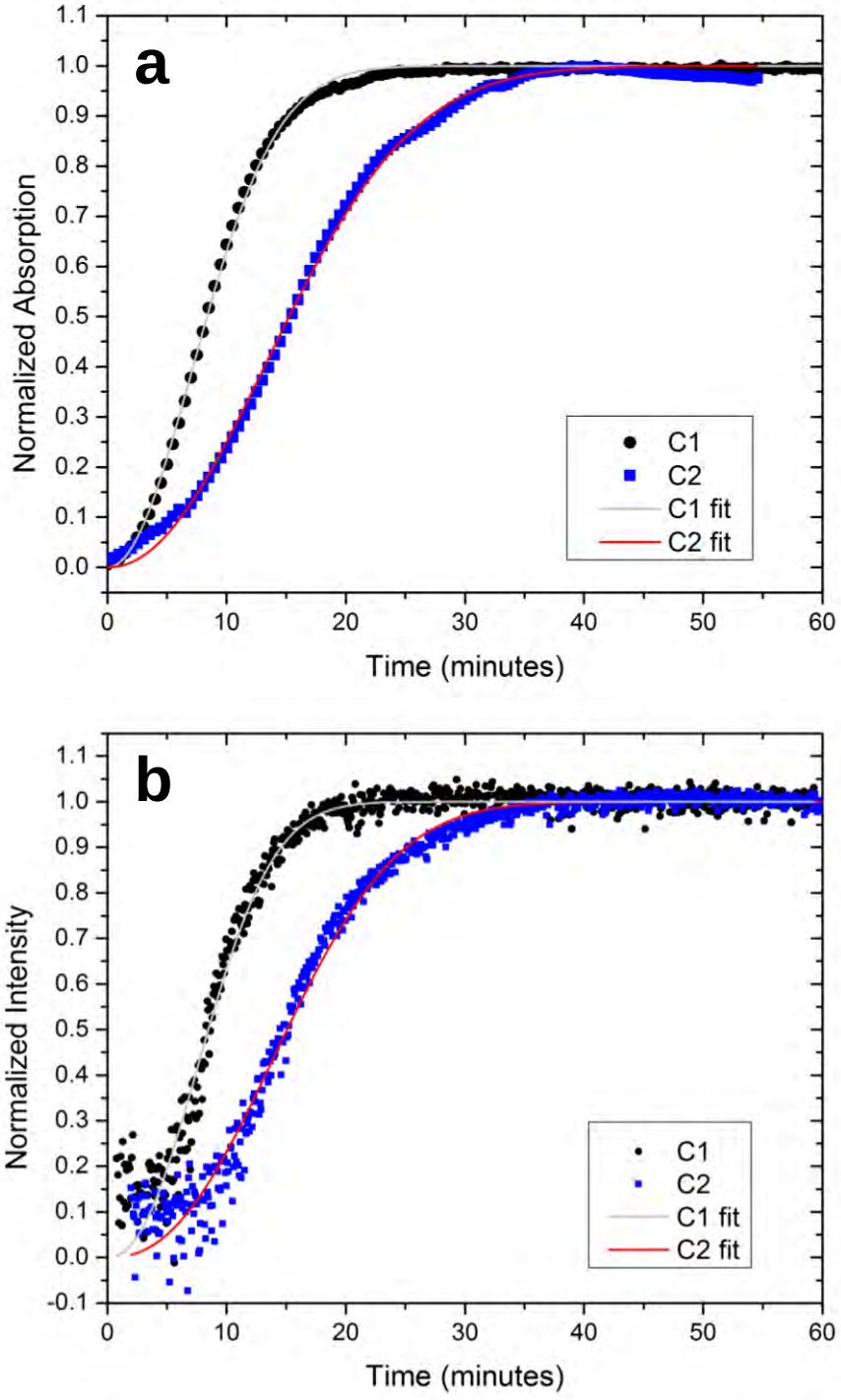

Fig. 4.8 Normalized Plots of C1 and C2 growth kinetic obtained from: a) UV-Vis spectroscopy; b) OCT.

The continuous lines in Fig. 4.8 correspond to the fitting data using Eq. 4.2. The corresponding fitting values for the growth rate parameter ***k*** and the Avrami exponent ***n*** are shown in Table 4.1. The values are in perfect agreement with the above discussion; C1 shows the greatest ***k*** value, 0.1min^{-1}, almost double of C2 (***k***=0.056min^{-1}). However, the ***n*** parameter is more similar to both syntheses. As can be seen in Table 4.1, OCT and UV-Vis spectroscopy have similar results of the growth kinetics parameters of CNCBs.

Table 4.1 Fitting parameters values obtained for the three techniques used.

CNCB Synthesis	Technique	k (min^{-1})	n
C1	OCT	$0.100 \pm 5.1e^{-4}$	2.18 ± 0.035
	UV-Vis spectroscopy	$0.100 \pm 2.2e^{-4}$	2.05 ± 0.013
	DLS Peak 2	$0.103 \pm 5.8e^{-3}$	2.29 ± 0.470
C2	OCT	$0.056 \pm 1.8e^{-4}$	2.35 ± 0.025
	UV-Vis spectroscopy	$0.055 \pm 1.9e^{-4}$	2.08 ± 0.022
	DLS Peak 2	$0.059 \pm 2.1e^{-3}$	1.89 ± 0.180
Secondary Synthesis			
C1	DLS Peak 1	$0.060 \pm 3.2e^{-3}$	3.37 ± 0.740
C2	DLS Peak 1	$0.048 \pm 4.3e^{-3}$	3.08 ± 1.100

DLS growth kinetics

Size evolutions in the growth of NCs have been reported in other works [8, 18] by means of TEM images. In those cases, the NC formation was slower and the full syntheses took from 160 min to 50 h. These conditions made possible the preparation of samples for TEM analysis without a significant change in size and morphology. In our case, the full syntheses took 30 and 50 min for C1 and C2, respectively; therefore, TEM analysis is not the best choice for size analysis as time function. Nevertheless, detailed information of the average size and size distribution can be done

by using DLS technique, in fact, DLS permits to avoid any disturbance in the growth kinetics by in situ and in real-time measurements.

Figure 4.9a, b shows the statistic graphs of size distribution for C1 and C2 recorded after 5 min of initiating the syntheses. The graphs show two peaks, which means that a bimodal distribution is present. Peak 2 correspond to NPs of the desired syntheses (CNCBs), whereas peak 1 correspond to particles with different morphology and smaller than nanocubes. We believe they were formed by the nucleation process at the same time that concave cubes were growing. The mean size of NPs at minute 5 given by peak 1 and peak 2 are 2 and 47nm for C1 and 9 and 49nm for C2. As soon as time goes, the size of the particles increases faster, such as was observed in OCT and UV-Vis spectroscopy, to finally reach the final size. The size averaged in time from minute 40 to 60 gives a mean final size of 12±1 and 28±6nm for peak 1, and 78±4 and 115±8nm for peak 2, respectively, for C1 and C2. The mean sizes of peak 2 are in perfect agreement with the mean side length of CNCBs measured by TEM images; these values estimated at the final stage of the syntheses can be considered as a good reference to confirm that sizes at intermediate stages were accurately measured by DLS.

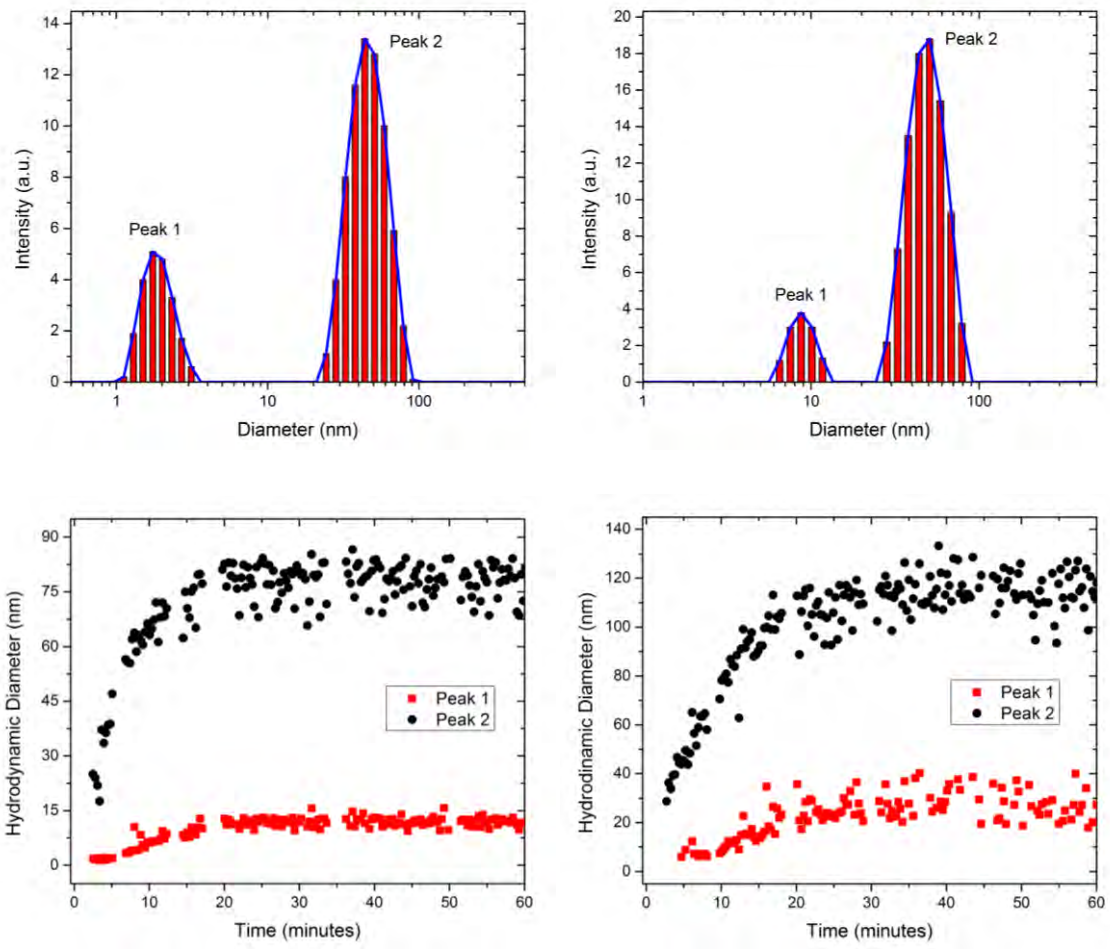

Fig. 4.9 a) and b) Statistic graphs of size distribution at minute 5 for C1 and C2 respectively; c) and d) plots of NPs size as time function obtained from DLS measurements for C1 and C2 respectively.

The size of CNCBs as time function is plotted for both peaks in Fig. 4.9c, d for syntheses C1 and C2, respectively. These plots show a sigmoidal behavior. Since the desired crystals start to grow from seeds addition, the nucleation process is not expected, but peak 1 displays, which we believe is a nucleation process, represented by a longer slow growth state at the beginning of the syntheses. In some works [8, 18], a bimodal distribution is reported as yield and prove of the aggregative growth process, where small particles correspond to little aggregates which

coalescence to form the final crystal; they are also observed only at initial times; however, in our case, the secondary crystals grew simultaneously to concave cubes.

The plots of the mean size versus time were converted in plots of NC volume versus time and fitted using the KJMA equation (Eq. 4.3).

$$V_t = V_i + (V_{\lim} - V_i)(1 - e^{-(kt)^n}), \quad (4.3)$$

parameters ***k*** and ***n*** are the same as in Eq. 4.2, V_t is the mean volume at time ***t***, V_{lim} is the final mean volume of the NPs, and V_i is the initial mean volume, which in this case, is the seed volume (65.45 nm^3) corresponding to a seed size of 5 nm.

The size data converted to volume values are shown in Fig. 4.10a for C1 and Fig. 4.10b for C2; the experimental data are represented by points, while the continuous lines correspond to the fitting data using Eq. 4.3. The fitting values are reported in Table 4.1. As expected, the synthesis C1 shows a higher constant growth rate, ***k***=0.103min^{-1}, 1.69 times the value of the constant ***k*** for C2, ***k***=0.059min^{-1}; these values are in perfect agreement with time relations that each solution required to reach the steady state, the time that C2 took to reach the steady state was 1.6 times the time that took C1. In the case of the Avrami exponent ***n***, it is higher for C1, ***n***=2.3, than for C2, ***n***=1.9; but, relative errors are also much higher than for the ***k*** parameter. The variations of ***n*** between C1 and C2 can be associated with the presence of other NPs; in fact, TEM images show that the colloid of C2 contains particles with different morphology to concave cubes. Therefore, it is possible that the less control over the morphology in this synthesis is affecting the value of the ***n*** parameter. The obtained values suggest that the Avrami exponent may be close to 2 for NPs with concave cube morphology.

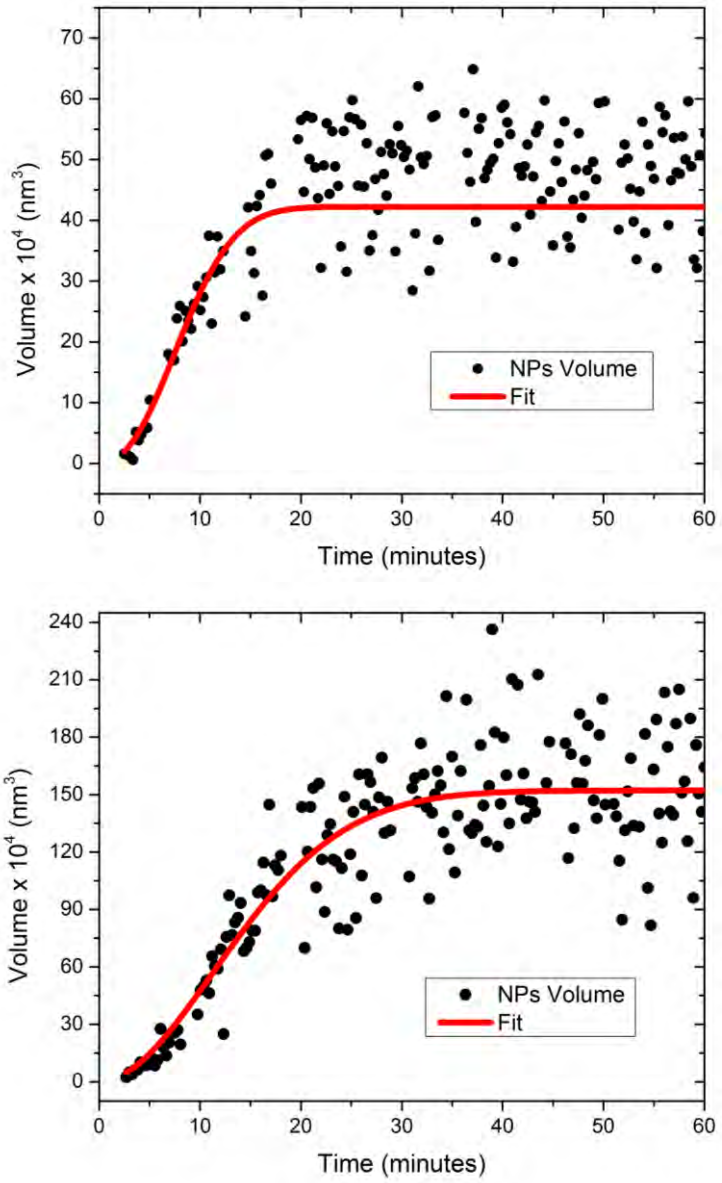

Fig. 4.10 Plots of NPs volume as time function obtained from DLS NPs size measurements, for: a) C1; b) C2.

On the other hand, the growth of NPs corresponding to peak 1 is different to peak 2. The fitting data of peak 1 show that the constant rate of growth ***k*** is a little higher for C1 ($0.060 min^{-1}$) than for C2 ($0.048 min^{-1}$). However, they are lower than those for peak 2; it implies that secondary syntheses took more time to reach the final size. The Avrami exponent ***n*** for peak 1 has the value

of 3.37 for C1 and 3.08 for C2. Although the final size of the observed NPs reach different critical values, a value close to 3 of the Avrami exponent can be related with both secondary syntheses; this means that the same kinetic process is present in both syntheses. Additionally, this value differs of the value of the Avrami exponent for the case of concave cubes, which in this work, we are considering as 2. This difference in the Avrami exponent values can be attributed to differences in morphology, since NPS of secondary syntheses have spherical morphology; which was determined by TEM images and can be observed in Fig. 4.5b, c.

In the case of secondary crystals, the other techniques used (OCT and UV-Vis spectroscopy) are not able to provide information about them, since in UV-Vis spectroscopy, the UV-Vis spectrum is dominated by the mean synthesis. In the case of OCT, a small size of NP implies low scattering at the wavelength we are working; in consequence, a low intensity of the image is generated, which sometimes could not be detected. Moreover, if it was some intensity from small particles, since the intensity is averaged to obtain contrast enhancement, as time goes, it increases and becomes uniform making not possible to detect both syntheses separately.

Table 4.1 shows the fitting parameters values for the three techniques. For C1, the constant growth rate, ***k***, show practically the same value for the three techniques. The maximum variation between the minimum and the maximum value for C1 is 2.91 %. For C2, the maximum variation is 6.78 %. Finally, for the Avrami parameter ***n***, the fitting values show a percentage variation in the values of 10.48 % for C1 and 19.57 % for C2. More significant variations in the fitting values of C2 were observed; we believe that the formation of other morphologies and the different sensitivities of each technique to the precipitation process are the main reasons for such variations.

The results show that each technique has the capacity to obtain a growth kinetic plot with feasible parameter values; however, by using the three techniques, better analyses can be carried out. By means of UV-Vis spectroscopy, an idea of the morphology and size of the NPs being synthesized can be given from the spectrum; on the other hand, sizes and size distribution along the growth process can be known by means of DLS almost since the beginning of the synthesis with a low concentration of NPs. In addition, a secondary synthesis could be detected. With OCT, it

is possible to see the scattering of few particles since the beginning of the synthesis; also, monitoring of growth is not affected by small variations in concentration of NPs.

4.4 Conclusions

In this chapter, the study of the growth kinetics of CNCBs on time resolved in situ studies by OCT, UV-Vis spectroscopy, and DLS is reported. The results show close fitting parameters ***k*** and ***n*** for the KJMA model among the three techniques, which implies that each technique is able to follow the growth kinetics separately; however, the combination of them permits to obtain additional information of the growth kinetics without the use of sophisticated and expensive techniques. The obtained values of the ***k*** parameter showed that nanocubes of small size grow faster than large ones. Moreover, an Avrami exponent close to 2 can be associated to the growth kinetics of CNCBs. Finally, to the best of our knowledge, this is the first time that OCT technique is used to study the growth kinetics of nanoparticles.

References

[1] C. Noguez, “Surface plasmons on metal nanoparticles: the influence of shape and physical environment,” The Journal of Physical Chemistry C, vol. 111, no.10, pp. 3806–3819, 2007, doi: http://dx.doi.org/10.1021/jp066539m.

[2] M. C. Daniel, D. Astruc, “Gold nanoparticles: assembly, supramolecular chemistry, quantum-size-related properties, and applications toward biology, catalysis, and nanotechnology,” Chemical Reviews, vol. 104, no. 1, pp.293–346, 2004, doi: http://dx.doi.org/10.1021/cr030698+.

[3] X. Huang, P. K. Jain, I. H. El-Sayed, M. A. El-Sayed, “Gold nanoparticles: interesting optical properties and recent applications in cancer diagnostic and therapy,” Nanomedicine (Lond), vol. 2, no. 5, pp. 681–693, 2007, doi: http://dx.doi.org/10.2217/17435889.2.5.681.

[4] H. Zhang, M. Jin, Y. Xia, “Noble-metal nanocrystals with concave surfaces: synthesis and applications,” Angewandte Chemie International Edition, vol. 51, no. 31, pp. 7656–7673, 2012, doi: http://dx.doi.org/10.1002/anie.201201557.

[5] Y. Ponce de León ,J. L. Pichardo-Molina, N. Alcalá Ochoa, D. Luna-Moreno, “Contrast enhancement of optical coherence tomography images using branched gold nanoparticles,” Journal of Nanomaterials, vol. 2012, 2012, doi: http://dx.doi.org/10.1155/2012/571015.

[6] X. Xia, J. Zeng, B. McDearmon, Y. Zheng, Q. Li, Y. Xia, “Silver nanocrystals with concave surfaces and their optical and surface-enhanced raman scattering properties,” Angewandte Chemie International Edition, vol. 123, no. 52, pp. 12542–12546, 2011, doi: http://dx.doi.org/10.1002/anie.201105200.

[7] T. Herricks, J. Chen, Y. Xia, “Polyol synthesis of platinum nanoparticles: control of morphology with sodium nitrate,” Nano Letters, vol. 4, no. 12, pp. 2367–2371, 2004, doi: http://dx.doi.org/10.1021/nl048570a.

[8] S. P. Shields, V. N. Richards, W. E. Buhro, “Nucleation control of size and dispersity in aggregative nanoparticle growth. A study of the coarsening kinetics of thiolate-capped gold nanocrystals,” Chemical Materials, vol. 22, no. 10, pp. 3212–3225, 2010, doi: http://dx.doi.org/10.1021/cm100458b.

[9] N. Petkov, “In situ real-time TEM reveals growth, transformation and function in one-dimensional nanoscale materials: from a nanotechnology perspective,” ISRN Nanotechnology, vol. 2013, 2013, doi: http://dx.doi.org/10.1155/2013/893060.

[10] O. C. Compton, F. E. Osterloh, "Evolution of size and shape in the colloidal crystallization of gold nanoparticles," Journal of the American Chemical Society, vol. 129, no. 25, pp.7793–7798, 2007, doi: http://dx.doi.org/10.1021/ja069033q.

[11] Z. Wei, F. P. Zamborini, "Directly monitoring the growth of gold nanoparticle seeds into gold nanorods," Langmuir, vol. 20, no. 26, pp. 11301–11304, 2004, doi: http://dx.doi.org/10.1021/la047408k.

[12] J. Polte, R. Erler, A. F. Thunemann, S. Sokolov, T. T. Ahner, K. Rademann, F. Emmerling, R. Kraehnert, "Nucleation and growth of gold nanoparticles studied via in situ small angle x-ray scattering at millisecond time resolution," ACS Nano, vol. 4, no. 2, pp. 1076–1082, 2010, doi: http://dx.doi.org/10.1021/nn901499c.

[13] B. Abécassis, F. Testard, O. Spalla, P. Barboux, "Probing in situ the nucleation and growth of gold nanoparticles by small-angle x-ray scattering," Nano Letters, vol. 7, no. 6, pp. 1723–1727, 2007, doi: http://dx.doi.org/10.1021/nl0707149.

[14] J. Becker, O. Schubert, C. Sönnichsen, "Gold nanoparticle growth monitored in situ using a novel fast optical single-particle spectroscopy method," Nano Letters, vol. 7, no. 6, pp. 1664–1669, 2007, doi: http://dx.doi.org/10.1021/nl070627g.

[15] M. Harada, Y. Kamigaito, "Nucleation and aggregative growth process of platinum nanoparticles studied by in situ quick XAFS spectroscopy," Langmuir, vol. 28, no. 5, pp. 2415–2428, 2012, doi: http://dx.doi.org/10.1021/la204031j.

[16] R. Patakfalvi, Z. Virányi, I. Dékány, "Kinetics of silver nanoparticle growth in aqueous polymer solutions," Colloid and Polymer Science, vol. 283, no. 3, pp. 299–305, 2004, doi: http://dx.doi.org/10.1007/s00396-004-1138-8.

[17] P. N. Njoki, A. Jacob, B. Khan, J. Luo, C. J. Zhong, "Formation of gold nanoparticles catalyzed by platinum nanoparticles: assessment of the catalytic mechanism," The Journal of Physical Chemistry B, vol. 110, no. 45, pp. 22503–22509, 2006, doi: http://dx.doi.org/10.1021/jp0642342.

[18] P. N. Njoki, J. Luo, M. M. Kamundi, S. Lim, C. J. Zhong, "Aggregative growth in the size-controlled growth of monodispersed gold nanoparticles," Langmuir, vol. 26, no. 16, pp. 13622–13629, 2010, doi: http://dx.doi.org/10.1021/la1019058.

[19] P. N. Njoki, I. I. S. Lim, D. Mott, H. Y. Park, B. Khan, S. Mishra, R. Sujakumar, J. Luo, C. J. Zhong, "Size correlation of optical and spectroscopic properties for gold nanoparticles," The Journal of Physical Chemistry C, vol. 111, no. 40, pp. 14664–14669, 2007, doi: http://dx.doi.org/10.1021/jp074902z.

[20] K. L. Kelly, E. Coronado, L. L. Zhao, G. C. Schatz, "The optical properties of metal nanoparticles: the influence of size, shape, and dielectric environment," The Journal of Physical Chemistry B, vol. 107, no. 3 pp. 668–677, 2003, doi: http://dx.doi.org/10.1021/jp026731y.

[21] J. Zhang, M. R. Langille, M. L. Personick, K. Zhang, S. Li, C. A. Mirkin, "Concave cubic gold nanocrystals with high-index facets," Journal of the American Chemical Society, vol. 132, no. 14, pp. 14012–14014, 2010, doi: http://dx.doi.org/10.1021/ja106394k.

[22] D. L. Van Hyning, W. G. Klemperer, C. F. Zukoski, "Silver nanoparticle formation: predictions and verification of the aggregative growth model," Langmuir, vol. 17, no. 11, pp. 3128–3135, 2001, doi: http://dx.doi.org/10.1021/la000856h.

[23] T. O. Drews, M. Tsapatsis, "Model of the evolution of nanoparticles to crystals via an aggregative growth mechanism," Microporous and Mesoporous Materials, vol. 101, no. 1–2, pp. 97–107, 2007, doi: http://dx.doi.org/10.1016/j.micromeso.2006.10.021.

[24] V. N. Richards, N. P. Rath, W. E. Buhro, "Pathway from a molecular precursor to silver nanoparticles: the prominent role of aggregative growth," Chemical Materials, vol. 22, no. 11, pp. 3556–3567, 2010, doi: http://dx.doi.org/10.1021/cm100871g.

[25] M. Avrami, "Kinetics of phase change I: general theory," The Journal of Chemical Physics, vol. 7, no. 12, pp. 1103-1939, 2004, http://dx.doi.org/10.1063/1.1750380.

[26] M. Avrami, "Kinetics of phase change. II: transformation-time relations for random distribution of nuclei," The Journal of Chemical Physics, vol. 8, no. 2, pp. 212-224, 1940, http://dx.doi.org/10.1063/1.1750631.

[27] M. Avrami, "Granulation, phase change, and microstructure kinetics of phase change. III," The Journal of Chemical Physics, vol. 9, no. 177, 1941, http://dx.doi.org/10.1063/1.1750872.

[28] A. A. Burbelko, E. Fraś, W. Kapturkiewicz, "About Kolmogorov's statistical theory of phase transformation," Materials Sciemce and Engineering: A, vol. 413–414, pp. 429–434, 2005, http://dx.doi.org/10.1016/j.msea.2005.08.161.

[29] J. M. Fujimoto, Optical coherence tomography: introduction. In: B. E. Bouma, G. J. Tearney (eds.) Handbook of optical coherence tomography. Marcel Dekker, New York, pp. 1–40, 2002.

CHAPTER 5

Contrast Enhancement of Optical Coherence Tomography Images Using Branched Gold Nanoparticles

5.1 Introduction

Different endogenous materials have been investigated as contrast agents in optical coherence tomography imaging of tissue structure [1-5]; however, they are very expensive, exhibit low photostability values, introduce poor contrast enhancement, and are difficult to tune in the NIR region. In the last decade, new materials, such as metallic and polymeric NPs, have been designed to have very interesting optical properties [6-8], but few have been explored as contrast agents [9-14]. Metallic NPs have many advantages over dyes and polymeric nanomaterials; they show high photostability and their plasmon band is easily tuned from visible to NIR by controlling their size and morphology [15-17]. The electric field near the NP surface can be highly amplified by the plasmon resonance, which is principally used in surface-enhanced Raman scattering (SERS). Resonant excitation of plasmons also contributes to the strong sensitivity of plasmon resonance to the local dielectric environment, which is exploited in localized surface plasmon resonance (LSPR) sensing [18]. Nonlinear optical effects are also present, such as second harmonic generation (SHG) [19-20]. Additionally, gold NPs are biocompatible and non-toxic, and they can be functionalized to target specific bio-markers of tissue and cells [21-23].

Nanoparticles of different morphologies, such as nanospheres, nanocages or nanorods, have been used to increase the contrast of OCT images; however, the reports show that those geometries and sizes do not significantly improve contrast when the central wavelength of the OCT does not perfectly match the plasmon band of NPs. For example, Anant Agrawal et. Al. [24] tested core/shell NPs of silica/gold with different sizes of core and shell; their NPs were tested in

water and turbid tissue phantoms, getting the maximum enhancement for those NPs with a core of 291 nm and a shell of 25 nm ($1.0x10^9$ nanoshells/ml) for an OCT system with a central wavelength at 1300 nm. Hu Chang et al. [12] fabricated gold nanocages of 35 nm with a plasmon band located at 716 nm, which match the spectrum of their OCT system; they tested the nanocages in a gelatin phantom embedded with TiO_2, and the tissue phantom was well contrasted due to strong light absorption by the nanocages. Another interesting work was reported by Timothy S. Troutman et al. [11], who used gold nanorods of 80 and 120 nm in length with longitudinal plasmon bands located at 750 and 912 nm, respectively, they tested the gold nanorods in polyacrylamide tissue phantoms embedded with polystyrene nanospheres, and found that nanorods, which match the central wavelength of the OCT (890 nm), allow getting maximum enhancement of backscattered light, although out of this wavelength, enhancement is very low.

Recently, new exotic morphologies of metallic NPs have been synthesized; particularly those with tips, such as nanostars or branched NPs [25-27], concave nanocubes [28] or nanoflowers [29]. These intricate morphologies exhibit strong light scattering at longer wavelengths (NIR) and have relatively small sizes. New synthesis methodologies open the viability of producing them with high reproducibility, thus making them suitable as contrast agents for OCT imaging.

To our knowledge, this is the first time that B-GNPs are reported to be used as a contrast agent for OCT imaging. In this chapter, results of the evaluation of B-GNPs in water and turbid tissue phantoms of agarose with TiO_2 are presented. Our results show several advantages of the B-GNPs over those previously reported: our NPs are smaller, and the plasmon band is easily tuned in the NIR. The Vis-NIR extinction spectra shows that B-GNPs still scatter light very efficiently at 1325 nm, enhancing the contrast of the OCT images, and could be used for different central wavelengths.

5.2 Experimental Section

Synthesis of nanoparticles

Branched gold nanoparticles: B-GNPs were fabricated following a process that is slightly different to the typical synthesis of concave gold nanocubes [28]. Before initiating the synthesis, all glassware was cleaned in aqua regia and rinsed with plenty of water. First, a cetyltrimethylammonium chloride (CTAC) solution of 10 ml at 0.1M was prepared, to which, once it was well dissolved in Millipore water, 250 µl of $HauCl_4$ (0.01M) and 600 µl of freshly solution of $NaBH_4$ (0.01M, prepared in an ice bath) were added; the colloid was prepared under continuous magnetic stirring. After $NaBH_4$ was added, the solution took a pale brown color. We continued the stirring for a couple of minutes, and then the colloid was left to stand for three hours. According to the Transmission Electron Microscopy (TEM) images, the seed colloid consisted of spherical particles with a mean size of 4±0.8 nm and with a typical concentration of ≈7.2 x 10^{13} NPs/ml. See Table 5.1 for more details.

Once the gold seeds were ready, branched NPs were prepared in the following way: solutions of 10 ml CTAC (0.1M) were prepared under magnetic stirring, and successively, 500 µl of $HauCl_4$ (0.01M), 100 µl of $AgNO_3$ (0.01M), 200µl of HCl (1M), and 100 µl of ascorbic acid (0.1M) were added. Finally, to initiate the growth of branched NPs, 10 µl of diluted seeds at a rate of 1:100 in CTAC (0.1M) were added. Magnetic stirring continued for 90 more minutes, and then the solution was left to stand undisturbed overnight.

Gold nanospheres: Gold nanospheres were prepared following the Turkevich method reported elsewhere [30]. In a typical synthesis, 20 ml of water and 40 µl of $HauCl_4$ (0.25M) were added to a glass flask of 50 ml. The solution was heated to boiling point; then 300 µl of sodium citrate at 1% were added under continuous magnetic stirring. The solution changed from being transparent to violet, and finally it became ruby red.

Gold nanorods: Gold nanorods were prepared using a seed mediated method [31-32]. First, seeds were prepared as follows: 5 ml of CTAB (0.2M), 5 ml of $HauCl_4$ (0.5mM) and 600 µl of

$NaBH_4$ (0.01M) are mixed and used as seeds within 1-2 hours after preparation; once the seeds were ready, we proceeded to prepare the gold nanorods. In a typical synthesis procedure, 10 ml of CTAB (0.2M) and 10 ml of $HauCl_4$ (0.5mM) were mixed, all under magnetic stirring; then, 220 µl of $AgNO_3$ (1mM) and 95 µl of ascorbic acid (0.1M) were added to get a transparent solution. Finally, 12 µl of the seed solution were added. Magnetic stirring continued for five more minutes, and then, the solution remained undisturbed overnight.

Vis-NIR spectroscopy and TEM analysis

The B-GNPs, nanospheres and nanorods obtained were analyzed by means of Vis-NIR spectroscopy and Transmission Electron Microscopy (TEM). Extinction spectra of the colloids were acquired using a Perkin Elmer lambda 900 spectrometer, with a spectral resolution of ±0.08 nm for UV/Vis and ±0.30 nm for NIR. The mean size and the geometrical shape of B-GNPs, nanospheres and nanorods were determined by TEM (Philips, MORGAGNI 268) after a careful analysis carried out in several TEM images using the ImageJ software 1.42q (Wayne Rasband National Institutes of Health, USA).

Gel samples preparation and OCT system

To evaluate the efficiency of B-GNPs as a contrast agent for OCT imaging, our NPs were tested in water and agarose-TiO_2 tissue phantoms. Agarose-TiO_2 phantoms were prepared in the following way: 0.1 g of agarose and 10 mg of TiO_2 were added to 10 ml of water at boiling point, all under magnetic stirring. Previously, 20 µl of concentrated NPs had been obtained from the centrifugation (1500 rpm, 10 min) of 1.5 ml of NPs solution; the NPs were then sonicated for ten minutes and afterwards, 30 µl of agarose gel were added. A three layer phantom was prepared as follows: first, one layer was prepared with agarose-TiO_2 solution; after that layer gelled, the agarose solution with NPs ($1.9x10^{11}$ NPs/ml) was poured over it, and finally, the solution of agarose-TiO_2 was poured to form the last layer. The tissue phantom was analyzed with a Swept Source Optical Coherence Tomography Imaging System (Thorlabs OCS1300SS) at a central wavelength of 1325 nm, with a spectral bandwidth of 100 nm.

5.3 Results and Discussion

The top graph of Fig. 5.1 shows the Vis-NIR optical extinction spectrum of B-GNPs recorded with a concentration of ≈6.6 x 10^9 NPs/ml; the spectrum is represented by the continuous line. The maximum peak of the extinction spectrum is located at 765 nm, but a deconvolution analysis shows that it can be described by four Gaussian peaks represented by the symbols ★, ■ , ┼ and ○ (see Fig. 5.1). The first peak (★) is located at 555 nm and corresponds to the size of the core of the B-GNPs, while the other three peaks may correspond to the plasmon hybridization of the tips with the core [18]. In fact, the last two peaks are located in the NIR, and the central wavelength of the source of the OCT is close to resonance with the last peak at 1198 nm. The bottom graph of Fig. 5.1 shows the absorption spectra corresponding to nanospheres (continuous line) and nanorods (dotted line); the maximum absorption peak for nanospheres is located at 570 nm, while the absorption peaks for nanorods are respectively located at 519 and 764 nm for the transversal and longitudinal plasmon bands.

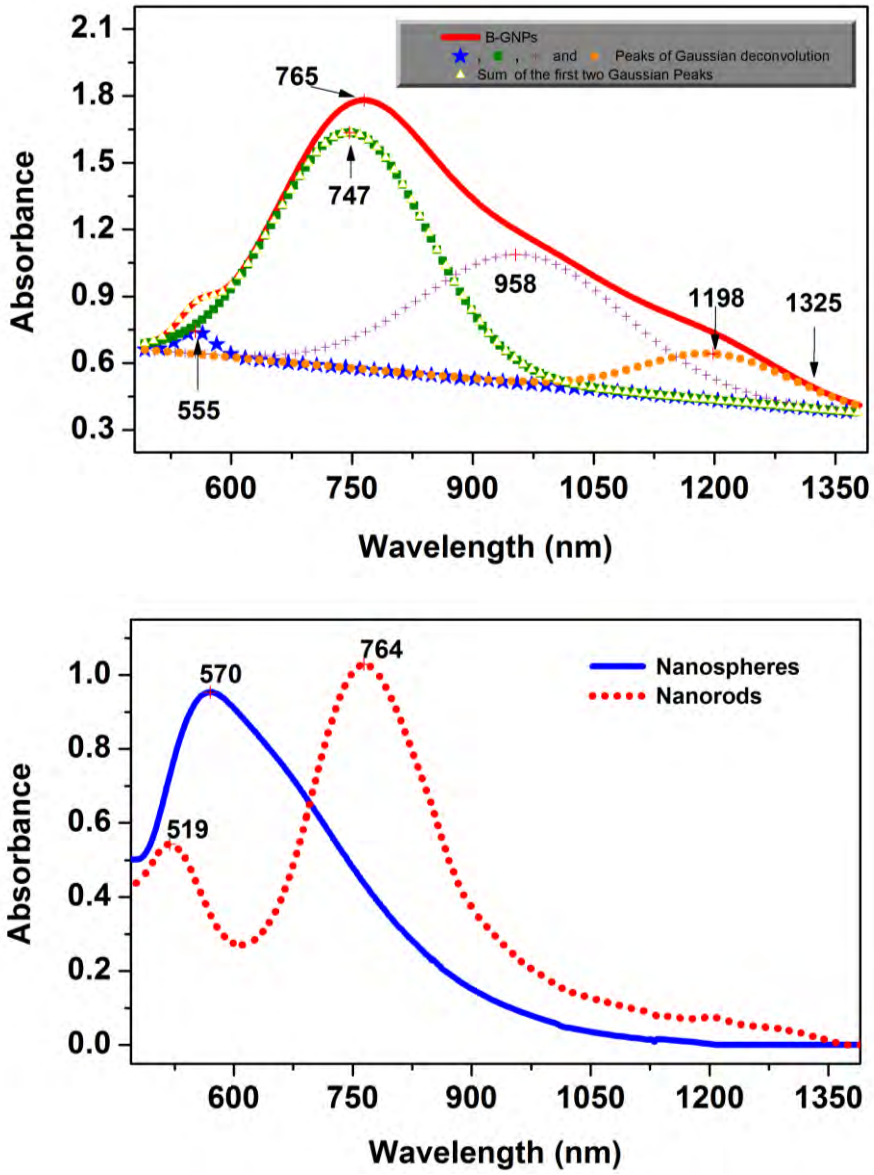

Fig. 5.1 The top graph corresponds to the absorption spectrum of B-GNPs and their Gaussian deconvolution. The continuous line corresponds to the Vis-NIR extinction spectrum of branched gold nanoparticles, while the next four curves correspond to the Gaussian deconvolution. The last curve represented by △ symbols corresponds to the sum of peaks one and two (★ and ■). The bottom graph corresponds to the absorption spectra of nanospheres and nanorods.

Several authors like Kumar et al. [33] and Trigari et al. [34], have reported the 74odeling of gold nanostars with tunable morphology. NPs with large tips display a significant shift of the plasmon band to the NIR region.

Figure 5.2 shows the characteristic TEM images of branched NPs, nanospheres and nanorods. For B-GNPs a mean core size of 78±13 nm and a mean tip length of 40±15 nm for their tips were measured; nonetheless, it is possible to find a few B-GNPs with tips of 120 nm of length. For nanospheres, the mean diameter was 64±12 nm, and for nanorods the mean length and diameter were 44±5 nm and 11±1 nm, respectively. Additional information related to the seeds and B-GNPs is shown in table 5.1.

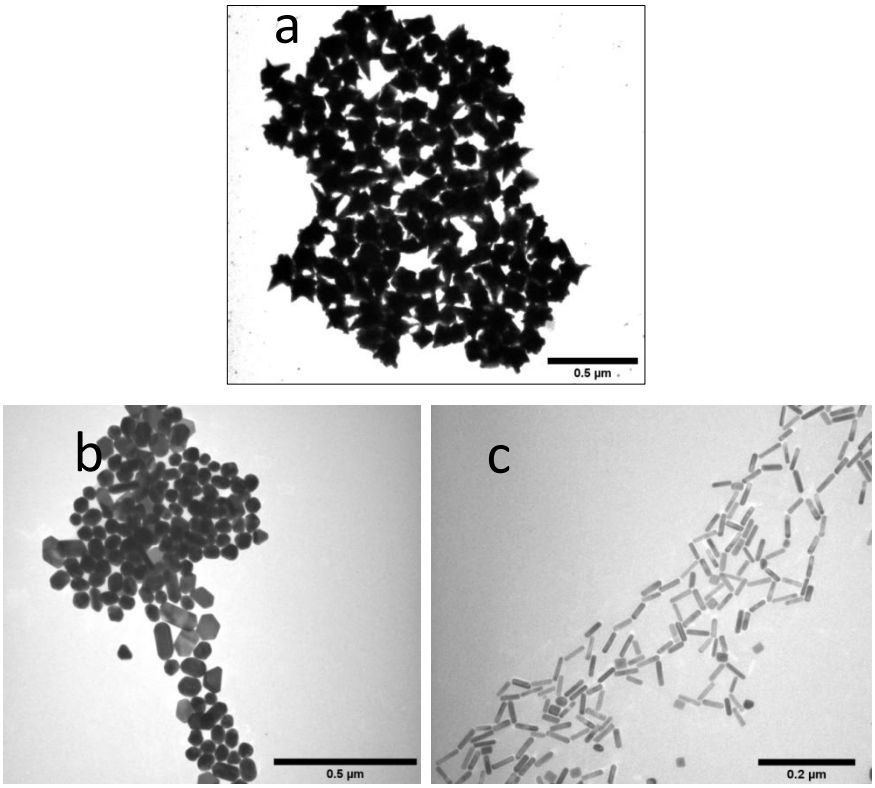

Fig. 5.2 TEM images of a) B-GNPs with mean core diameter of 78±13 nm and mean tip length of 40±15 nm, b) nanospheres with mean diameter of 64±12 nm, and c) nanorods with mean length and diameter of 44±5 and 11±1 nm, respectively.

Table 5.1 Summary of gold seeds and B-GNPs.

Seed Concentration (no. of seeds/ml)	Mean core size of B-GNPs (nm)	Mean tip length of B-GNPs (nm)	Concentration [a] (no. of B-GNPs/ml)
$7.2X10^{13}$	78±13	40±15	$6.6X10^{9}$

[a] NP concentration was calculated in a manner similar to that in reference [35]

B-GNPs were studied as a contrast agent for OCT imaging in water and agarose-TiO_2 tissue phantom. To show the efficiency of our B-GNPs, we compared them with other morphologies, such as nanorods and nanospheres. Figure 5.3 shows the OCT B-scan images corresponding to water samples with nanospheres, nanorods and B-GNPs. The air-water interface can be identified because the border of the interface looks very bright at the top of each image. Also, a white line, a little below the interface was drawn as reference for future calculations of the average A-scan profiles and for contrast enhancement calculations.

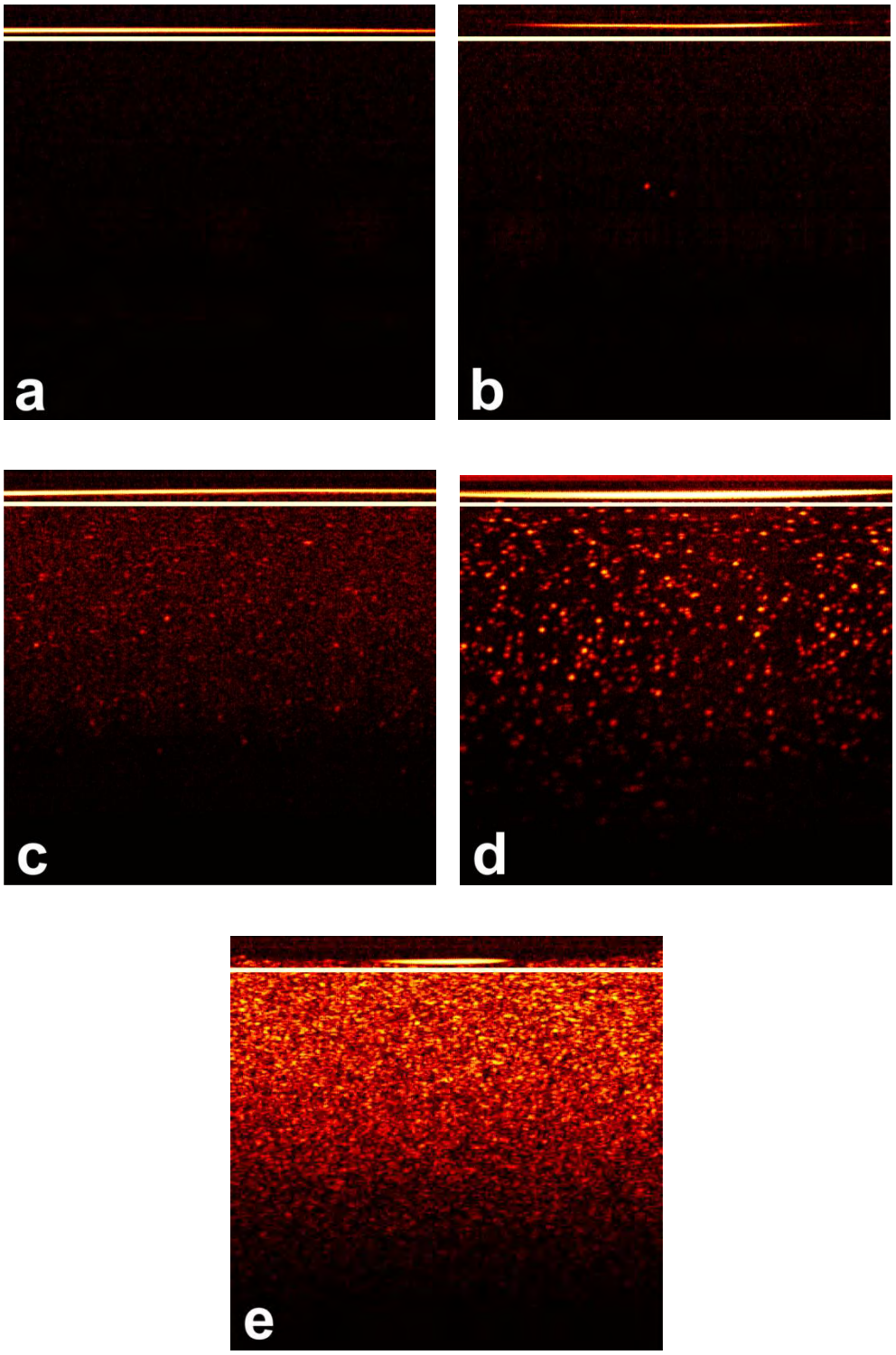
a
b
c
d
e

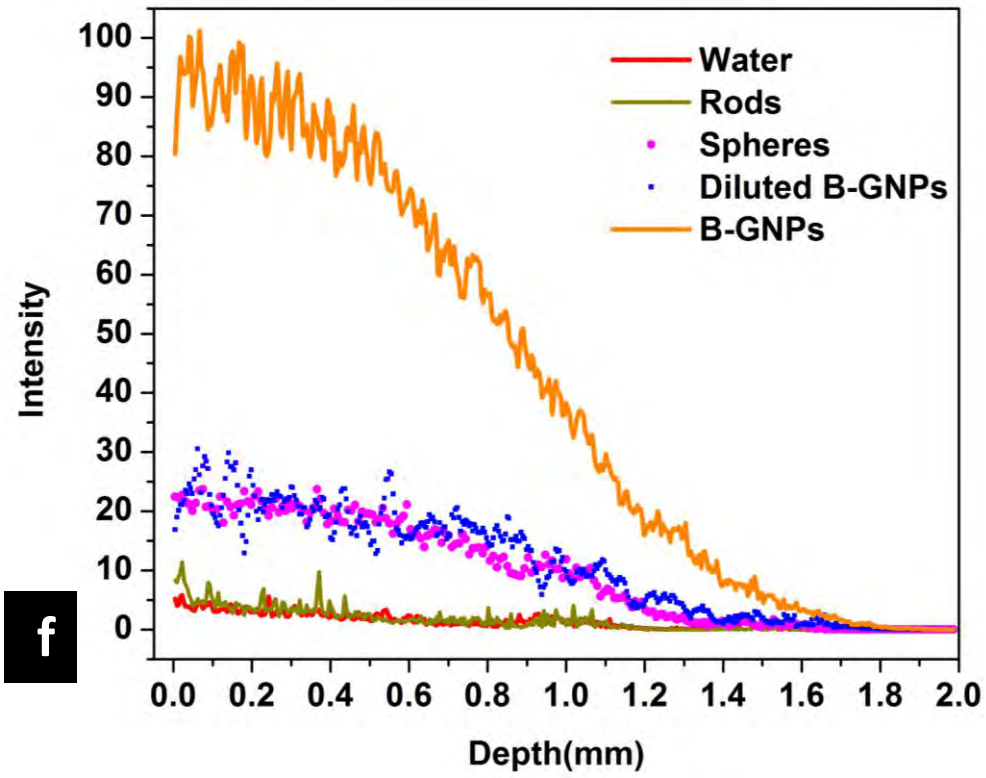

Fig. 5.3 OCT B-scan images of a) water without NPs, b) nanorods in water, c) nanospheres in water, d) diluted B-GNPs in water, e) B-GNPs in water, and f) average A-scan profiles of the water samples. Water without NPs is represented by the black continuous line, nanorods in water by the light gray continuous line, nanospheres in water by ●, diluted B-GNPs by ◇, and B-GNPs by the gray continuous line.

Figure 5.3a shows the OCT B-scan image for the case of Millipore water (18.2 MΩcm and <10 ppb total organic carbon). The OCT image of water is poorly contrasted due to the low intensity of the scattered light; it is difficult to appreciate any bright spot from water molecules, and excepting the interface, the image is almost totally black. Something similar happens in the case of nanorods ($2.1x10^{12}$ NPs/ml) (see Fig. 5.3b): contrast is very poor, except for a few bright spots which can be attributed to big NPs. On the other hand, in the case of nanospheres, Fig. 5.3c, contrast is notably improved, but it still shows a weak contrast enhancement of the image, in spite of the concentration of nanospheres ($3.7x10^{10}$ NPs/ml) is higher than that of the diluted B-GNPs, Fig. 5.3d. These results can be explained from the absorption spectra of nanorods and

nanospheres; optical extinction around 1325 nm is almost zero, so we cannot expect high contrast enhancement due to low scattering intensity. However, for B-GNPs prepared at a concentration of ≈2.2x10^9 NPs/ml, Fig. 5.3d, the intensity due to scattering becomes very strong. The cross sectional image of water with B-GNPs shows spots of similar sizes but with significant differences in intensity. These changes in intensity mean that some of these particles scatter light more efficiently at the central wavelength of the OCT source. In theory, each spot corresponds to one NP, although we do not discard the possibility of a low degree of aggregation which also produces a very efficient process of scattering. As a matter of fact, we expect that the brightest spots correspond to B-GNPs with larger tips. In fact, OCT images of water with B-GNPs with a concentration of 6.6x10^9 NPs/ml (see Fig. 5.3e) were acquired, but in this case we could not see the isolated spots corresponding to each NP, and we only appreciate a bright continuous background, due to the high concentration of NPs. The characteristic mean A-scan was calculated averaging a total of 512 A-scans for the different cases: water without NPs, nanospheres in water, nanorods in water, and diluted and non-diluted B-GNPs in water, which are shown in Fig. 5.3f. Again, from these profiles, we can see more clearly the high efficiency of B-GNPs to enhance the contrast of OCT images. The profile corresponding to water is very flat, as is the nanorods profile, while the profile for nanospheres has a similar intensity of diluted B-GNPs, showing that B-GNPs are more efficient than nanospheres to enhance the contrast of OCT images. On the other hand, B-GNPs without dilution show a very high intensity increment in comparison with the other NPs; indeed, the reflected light intensity at 0.2 mm of depth is around four times higher than that for nanospheres.

The main goal of the present work is to show the usefulness of the B-GNPs as a contrast agent for tissue analysis (enhancing the contrast of OCT images of tissue layers); for this reason, we analyzed a turbid tissue phantom of agarose-TiO2 with and without B-GNPs. Figure 5.4a shows the OCT B-scan image of the turbid tissue phantom; remember that our phantom was prepared with a layer of B-GNPs (1.9x1011 NPs/ml) on the left, but without NPs on the right.

At the bottom of the right side of Fig. 5.4a, the OCT image shows the tissue phantom without B-GNPs; the contrast of the image in this zone is very poor due to the fact that the intensity of backscattered light is very low at this depth, ≈1.5 mm. On the other hand, at the

bottom of the left side, at the same depth, a thin bright layer can be noticed, which corresponds to a thin layer of agarose with B-GNPs. The arrows in Fig. 5.4b show the location of the B-GNPs.

After careful visual inspection, it can be observed that the OCT image displays significant variation in intensity of backscattered light along the layer of B-GNPs, since the upper layer of agarose-TiO_2 on the left side is thinner than on the right side; indeed, the left side shows the presence of an air bubble in the phantom, and the air bubble sent the NPs outside. Then, the NPs around the bubble show good contrast enhancement when compared to the area inside the bubble. Figure 5.4c shows the average profile of the tissue phantom for both cases: the dotted line represents the phantom without B-GNPs, while the continuous line represents the profile of the phantom with branched NPs. The average profile of the tissue phantom without B-GNPs shows a relatively smooth curve. In fact, no abrupt changes of intensity can be appreciated, as it was observed in the profile of water with NPs, which means that the TiO_2 in the phantom was distributed very homogeneously. Also, it can be noticed that the backscattering light decreases continuously as a function of depth. A similar behavior is observed for the case where B-GNPs were used, except at the depth of 1.52 mm, where a sharp peak of backscattered light is observed. This peak shows that even though our NPs are smaller than the TiO_2 particles, they are more efficient at backscattering light.

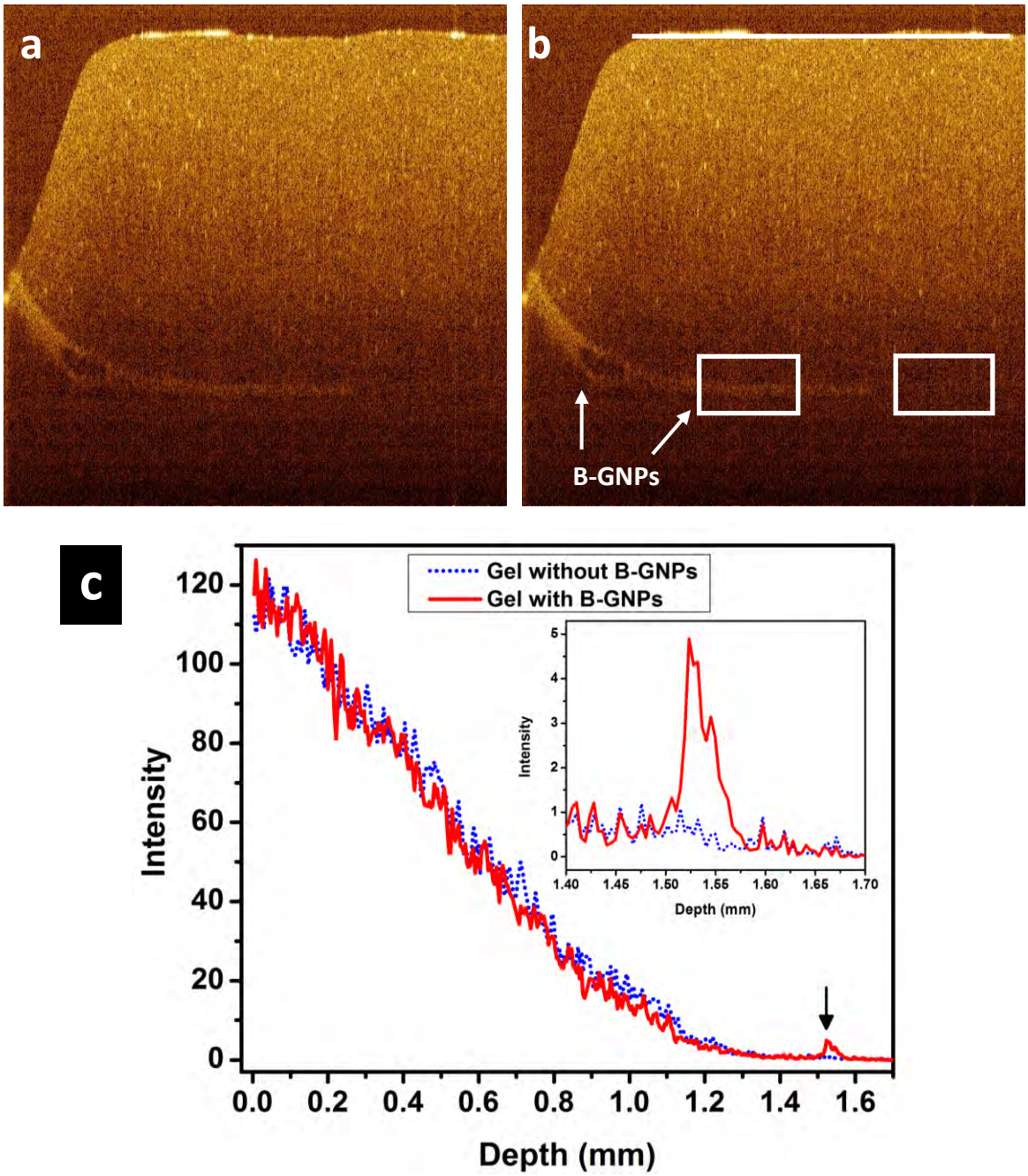

Fig. 5.4 a) Characteristic OCT B-scan image of the tissue phantom with and without B-GNPs. B) OCT B-scan image of the tissue phantom showing the corresponding zones used to calculate contrast enhancement (white squares). C) Average A-scan of the tissue phantom without B-GNPs is represented by the dotted line, while average A-scan of the tissue phantom with B-GNPs is represented by the continuous line. Inset: zoom of the profile corresponding to the depth of the layer with nanoparticles (signaled by the arrow) showing the enhancement of backscattered light.

In order to get a more quantitative and reliable analysis of the behavior of our B-GNPs, the quantification of the contrast enhancement (CE) for OCT images was calculated using the following equation [11].

$$\boldsymbol{CE = 10 * log10\left(\frac{average\ pixel\ intensity\ of\ the\ area\ with\ NPs}{average\ pixel\ \ intensity\ of\ the\ reference\ area}\right)} \quad (5.1)$$

In all cases (water with NPs), we considered an area of 2.00 mm x 1.98 mm for contrast enhancement calculation; the area was selected just below the air-water interface (white line), where our reference was a sample of Millipore water. The estimated increments in contrast were 9.19 dB for diluted B-GNPs in water and 15.07 dB for non-diluted B-GNPs. As we have mentioned, a similar procedure was carried out with the gold nanorods and nanospheres at the concentrations given above; the results for contrast enhancement were 0.65 and 8.72 dB respectively. From these results, we observed that even though nanorods show the plasmon band at 764 nm, almost at the same position of B-GNPs; contrast enhancement is very poor in this case. On the other hand, gold nanospheres show good contrast enhancement, almost the same that was obtained for diluted B-GNPs; however, for non-diluted B-GNPs, contrast enhancement is 1.7 times greater than that for nanospheres, which have a concentration (NPs/ml) one order of magnitude greater than B-GNPs. These results mean that B-GNPs work very well as a contrast agent in water, and that their performance is better than the one seen in the other two cases. Consequently, B-GNPs are the best option to use as a contrast agent in tissue phantoms in order to produce good optical contrast enhancement of OCT images.

Following a procedure similar to that used with water samples, the CE of agarose-TiO_2 tissue phantoms with NPs was calculated. For this case, we selected a rectangular area of 1.95 mm x 0.26 mm (see Fig.5. 4b); the white square on the left corresponds to tissue phantom with NPs, and the average pixel intensity of the area with NPs was obtained from this square, while the white square on the right corresponds to the tissue phantom without NPs, from which we calculated the average pixel intensity of the reference area. The calculated contrast enhancement using eq. 5.1 is equivalent to 3.17 dB. See Table 5.2 for more details.

Table 5.2 Summary of average pixel intensities and contrast enhancement values.

Sample	Average pixel intensity	Contrast enhancement (dB)
Water without NPs	1.30	-
B-GNPs in water	41.91	15.07
Diluted B-GNPs in water	10.81	9.19
Nanospheres in water	9.72	8.72
Nanorods in water	1.51	0.65
Phantom with B-GNPs	0.91	3.17
Phantom without B-GNPs	0.44	-

The present results show that the geometrical shape of branched NPs, which tune the plasmon resonance band at NIR, still enhances the backscattering light of the central wavelength of the OCT at 1325 nm very efficiently. Additionally, the optical extinction spectrum predicts that B-GNPs can be used as a contrast agent for OCT imaging with central sources close to 800 and 900 nm, unlike core/shell, nanocages or nanorods, which generally match just one of these central wavelength sources. The main reason is the behavior of the spectral extinction of the B-GNPs; as it has been shown, they exhibit three interesting peaks, located at 747, 958 and 1198 nm, which can be close to resonance with different OCT sources.

5.4 Conclusions

To our knowledge, this is the first time that B-GNPs are reported to be used as a contrast agent in OCT imaging. In the present work, we have proposed the use of branched gold NPs with a suitable mean core size of 78 nm and a mean tip length of 40 nm as contrast agent. As was shown,

they exhibit three interesting peaks located at 747, 958 and 1198 nm; which can be close to resonance with different central sources used for OCT imaging, yielding a very strong interaction with the plasmon resonance and enhancing the backscattered light, unlike nanorods, which only match one central wavelength, or nanospheres, which scatter light only if their size is big (bulk effect).

Our B-GNPs were evaluated in water and agarose-TiO_2 tissue phantoms, obtaining very good contrast enhancement: 9.19 dB for the case of B-GNPs diluted in water, 15.07 dB for the non-diluted sample, and 3.17 dB for agarose-TiO_2 tissue phantoms.

In general, we obtained considerable good increments in the contrast of OCT images, indicating that even though the maximum peak of the plasmon band is far away from the central wavelength of the OCT system, the peak located at 1198 nm is an indication that B-GNPs are still very efficient at scattering light at this wavelength. So, B-GNPs can be considered a good contrast agent for OCT imaging.

References

[1] C. Yang, “Molecular contrast optical coherence tomography: a review,” Photochemistry and Photobiology, vol. 81, no. 2, pp. 215–237, 2005. doi: http://dx.doi.org/10.1562/2004-08-06-IR-266.1.

[2] C. Xu, J. Ye, D. L. Marks, and S. A. Boppart, “Near-infrared dyes as contrast-enhancing agents for spectroscopic optical coherence tomography,” Optics Letters, vol. 29, no. 14, pp. 1647–1649, 2004. doi: http://dx.doi.org/10.1364/OL.29.001647.

[3] C. Yang, M.A.Choma, L. E. Lamb, J. D. Simon, and J.A. Izatt, “Protein-based molecular contrast optical coherence tomography with phytochrome as the contrast agent,” Optics Letters, vol. 29, no. 12, pp. 1396–1398, 2004. http://dx.doi.org/10.1364/OL.29.001396.

[4] C. Yang, L. E. L. Mc Guckin, J. D. Simon, M. A. Choma, B. E. Applegate, and J. A. Izatt, “Spectral triangulation molecular contrast optical coherence tomography with indocyanine green as the contrast agent,” Optics Letters, vol. 29, no. 17, pp. 2016–2018, 2004. http://dx.doi.org/10.1364/OL.29.002016.

[5] N. Iftimia, A. K. Iyer, D. X. Hammer et al., “Fluorescenceguided optical coherence tomography imaging for colon cancer screening: a preliminary mouse study,” Biomedical Optics Express, vol. 3, no. 1, pp. 178–191, 2012. http://dx.doi.org/10.1364/BOE.3.000178.

[6] M. Pelton, J. Aizpurua, and G. Bryant, “Metal-nanoparticle plasmonics,” Laser and Photonics Reviews, vol. 2, no. 3, pp. 136–159, 2008. http://dx.doi.org/10.1002/lpor.200810003.

[7] M. Rycenga, C.M. Cobley, J. Zeng et al., “Controlling the synthesis and assembly of silver nanostructures for plasmonic applications,” Chemical Reviews, vol. 111, no. 6, pp. 3669–3712, 2011. http://dx.doi.org/10.1021/cr100275d.

[8] N. J. Halas, S. Lal, W. S. Chang, S. Link, and P. Nordlander, “Plasmons in strongly coupled metallic nanostructures,” Chemical Reviews, vol. 111, no. 6, pp. 3913–3961, 2011. http://dx.doi.org/10.1021/cr200061k.

[9] E. V. Zagaynova,M. V. Shirmanova,M. Y. Kirillin et al., “Contrasting properties of gold nanoparticles for optical coherence tomography: phantom, in vivo studies and Monte Carlo simulation,” Physics in Medicine and Biology, vol. 53, no. 18, pp. 4995–5009, 2008. http://dx.doi.org/10.1088/0031-9155/53/18/010.

[10] Y. L. Kim, V. M. Turzhitsky, Y. Liu et al., "Low-coherence enhanced backscattering: a review of principles and applications for colon cancer screening," Journal of Biomedical Optics, vol. 11, no. 4, Article ID 041125, 2006. http://dx.doi.org/10.1117/1.2236292.

[11] T. S. Troutman, J. K. Barton, and M. Romanowski, "Optical coherence tomography with plasmon resonant nanorods of gold," Optics Letters, vol. 32, no. 11, pp. 1438–1440, 2007. http://dx.doi.org/10.1364/OL.32.001438.

[12] H. Cang, T. Sun, Z. Y. Li et al., "Gold nanocages as contrast agents for spectroscopic optical coherence tomography," Optics Letters, vol. 30, no. 22, pp. 3048–3050, 2005. http://dx.doi.org/10.1364/OL.30.003048.

[13] S. A. Boppart, "Advances in contrast enhancement for optical coherence tomography," in Proceedings of the 28th Annual International Conference of the IEEE Engineering in Medicine and Biology Society (EMBS '06), pp. 121–124, New York, NY, USA, September 2006. http://dx.doi.org/10.1109/IEMBS.2006.259366.

[14] M. A. Hahn, A. K. Singh, P. Sharma, S. C. Brown, and B. M. Moudgil, "Nanoparticles as contrast agents for in-vivo bioimaging: current status and future perspectives," Analytical and Bioanalytical Chemistry, vol. 399, no. 1, pp. 3–27, 2011. http://dx.doi.org/10.1007/s00216-010-4207-5.

[15] M. Grzelczak, J. P´erez-Juste, P. Mulvaney, and L. M. Liz-Marz´an, "Shape control in gold nanoparticle synthesis," Chemical Society Reviews, vol. 37, no. 9, pp. 1783–1791, 2008. http://dx.doi.org/10.1039/b711490g.

[16] T. K. Sau and A. L. Rogach, "Nonspherical noble metal nanoparticles: colloid-chemical synthesis and morphology control," Advanced Materials, vol. 22, no. 16, pp. 1781–1804, 2010. http://dx.doi.org/10.1002/adma.200901271.

[17] B. Wiley, T. Herricks, Y. Sun, and Y. Xia, "Polyol synthesis of silver nanoparticles: use of chloride and oxygen to promote the formation of single-crystal, truncated cubes and tetrahedrons," Nano Letters, vol. 4, no. 9, pp. 1733–1739, 2004. http://dx.doi.org/10.1021/nl048912c.

[18] F. Hao, C. L. Nehl, J. H. Hafner, and P. Nordlander, "Plasmon resonances of a gold nanostar," Nano Letters, vol. 7, no. 3, pp. 729–732, 2007. http://dx.doi.org/10.1021/nl062969c.

[19] K. Ozga, T. Kawaharamura, A. Ali Umar et al., "Second order optical effects in Au nanoparticle-deposited ZnO nanocrystallite films," Nanotechnology, vol. 19, no. 18, Article ID 185709, 2008. http://dx.doi.org/10.1088/0957-4484/19/18/185709.

[20] I. V. Kityk, J. Eboth´e, I. Fuks-Janczarek et al., "Nonlinear optical properties of Au nanoparticles on indium-tin oxide substrate," Nanotechnology, vol. 16, no. 9, pp. 1687–1692, 2005. http://dx.doi.org/10.1088/0957-4484/16/9/046.

[21] B. van de Broek, N. Devoogdt, A. D'Hollander et al., "Specific cell targeting with nanobody conjugated branched gold nanoparticles for photothermal therapy," ACS Nano, vol. 5, no. 6, pp. 4319–4328, 2011. http://dx.doi.org/10.1021/nn1023363.

[22] R. Wilson, "The use of gold nanoparticles in diagnostics and detection," Chemical Society Reviews, vol. 37, no. 9, pp. 2028–2045, 2008. http://dx.doi.org/10.1039/b712179m.

[23] C. Ungureanu, R. Kroes,W. Petersen et al., "Light interactions with gold nanorods and cells: implications for photothermal nanotherapeutics," Nano Letters, vol. 11, no. 5, pp. 1887–1894, 2011. http://dx.doi.org/10.1021/nl103884b.

[24] A. Agrawal, S. Huang, A. W. H. Lin et al., "Quantitative evaluation of optical coherence tomography signal enhancement with gold nanoshells," Journal of Biomedical Optics, vol. 11, no. 4, Article ID 041121, 2006. http://dx.doi.org/10.1117/1.2339071.

[25] N. R. Jana, L. Gearheart, and C. J. Murphy, "Seeding growth for size control of 5–40nm diameter gold nanoparticles," Langmuir, vol. 17, no. 22, pp. 6782–6786, 2001. http://dx.doi.org/10.1021/la0104323.

[26] S.Chen, Z. L. Wang, J. Ballato, S.H. Foulger, andD. L. Carroll, "Monopod, bipod, tripod, and tetrapod gold nanocrystals," Journal of the American Chemical Society, vol. 125, no. 52, pp. 16186–16187, 2003. http://dx.doi.org/10.1021/ja038927x.

[27] M. Yamamoto, Y. Kashiwagi, T. Sakata, H. Mori, and M. Nakamoto, "Synthesis and morphology of star-shaped gold nanoplates protected by poly(N-vinyl-2-pyrrolidone)," Chemistry of Materials, vol. 17, no. 22, pp. 5391–5393, 2005. http://dx.doi.org/10.1021/cm0515000.

[28] O. M. Bakr, B. H. Wunsch, and F. Stellacci, "High-yield synthesis of multi-branched urchin-like gold nanoparticles," Chemistry of Materials, vol. 18, no. 14, pp. 3297–3301, 2006. http://dx.doi.org/10.1021/cm060681i.

[29] J. Zhang, M. R. Langille, M. L. Personick, K. Zhang, S. Li, and C. A. Mirkin, "Concave cubic gold nanocrystals with highindex facets," Journal of the American Chemical Society, vol. 132, no. 40, pp. 14012–14014, 2010. http://dx.doi.org/10.1021/ja106394k.

[30] H. Li, Y. Yang, Y.Wang,W. Li, L. Bi, and L.Wu, "In situ fabrication of flower-like gold nanoparticles in surfactant-polyoxometalate-hybrid spherical assemblies," Chemical Communications, vol. 46, no. 21, pp. 3750–3752, 2010. http://dx.doi.org/10.1039/b916797h.

[31] J. Kimling, M. Maier, B. Okenve, V. Kotaidis, H. Ballot, and A. Plech, "Turkevich method for gold nanoparticle synthesis revisited," Journal of Physical Chemistry B, vol. 110, no. 32, pp. 15700–15707, 2006. http://dx.doi.org/10.1021/jp061667w.

[32] N. R. Jana, L. Gearheart, and C. J.Murphy, "Wet chemical synthesis of high aspect ratio cylindrical gold nanorods," Journal of Physical Chemistry B, vol. 105, no. 19, pp. 4065–4067, 2001. http://dx.doi.org/10.1021/jp0107964.

[33] B. Nikoobakht and M. A. El-Sayed, "Preparation and growth mechanism of gold nanorods (NRs) using seed-mediated growth method," Chemistry of Materials, vol. 15, no. 10, pp. 1957–1962, 2003. http://dx.doi.org/10.1021/cm020732l.

[34] P. S. Kumar, I. Pastoriza-Santos, B. Rodríguez-González, F. Javier García de Abajo, and L. M. Liz-Marzán, "High-yield synthesis and optical response of gold nanostars," Nanotechnology, vol. 19, no. 1, Article ID 015606, 2008. http://dx.doi.org/10.1088/0957-4484/19/01/015606.

[35] S. Trigari, A. Rindi, G.Margheri, S. Sottini, G. Dellepiane, and E. Giorgetti, "Synthesis and modelling of gold nanostars with tunable morphology and extinction spectrum," Journal of Materials Chemistry, vol. 21, no. 18, pp. 6531–6540, 2011. http://dx.doi.org/10.1039/c0jm04519e.

CHAPTER 6

General Conclusions

The work presented in this thesis, in general, comprised the use of the optical coherence tomography technique together with NPs with concave surfaces. The two works developed consisted in the following of the NPs growth kinetics by the OCT technique, and in the use of NPs as contrast agent for OCT imaging. Both works are considered pioneers, since we are proposing for the first time the use of the OCT technique to follow NPs growth kinetics; equally, branched NPs are suggested as contrast agent for OCT imaging for the first time.

It was said that in order to use NPs in applications is necessary to have a control over their morphology and size, for which is necessary understand the growth process. The first work done for this thesis provides a new technique to follow NPs growth kinetics; which is analogous to follow the NPs growth kinetics by means of UV-Vis absorption spectroscopy. The results confirm that the OCT system is able to follow NPs growth kinetics with the same accuracy of UV-Vis spectroscopy and DLS techniques. Additionally, OCT can detect a low concentration of NPs since the beginning of the synthesis, and images suggest that individual NPs can be detected. Another advantage is that unlike UV-Vis spectroscopy, OCT is not so sensible to changes due to NP precipitation. Therefore, OCT has proved to be a useful technique to follow NPs growth kinetics; and combined with other techniques complementary results can be obtained without the use of sophisticated and expensive systems.

Due to the properties that NPs with concave surfaces own, they are good candidates for different applications, such as contrast agent for OCT imaging. The experiments carried in this thesis confirm it. The results shown that unlike other NPs shapes, such as rods or spheres, which need to have their plasmon band matched with the central wavelength of the OCT system used to be useful as contrast agent, branched NPs are good contrast agent even when their main plasmon band is far away of the central wavelength of the OCT system used; also, NP size does not need to be as large as other morphologies for being used in the region of 1300 nm. In addition, from the

results of the water samples, it can be observed that a low concentration of NPs is enough to generate a high contrast on the image. In general, the results show that B-GNPs generate high contrast in water samples such as in a highly scattering medium; becoming a good contrast agent for OCT imaging.

With the works presented in this thesis two new lines of investigation have been open, where many works can be done as continuation and other new can be proposed, for instance, analysis of the growth kinetics of other concave cubes sizes can be performed, or a variation of quantity of one or more chemical components in the synthesis of CNCBs can be done and analyzed. In the same way, synthesis of other morphologies of NP could be analyzed; as well as other techniques, different to UV-Vis spectroscopy and DLS, could be coupled with the OCT system to perform more complex analyses of the NPs growth kinetics. In the use of NPs as contrast agent for OCT imaging, branched NPs can be analyzed as contrast agent in real tissue, or can be functionalized to prove their efficiency as marker. Additionally, B-GNPs can be analyzed with OCT systems which central wavelengths are below 1300 nm. Besides, new investigation in the same line can be done by testing others types of NPs with concave surfaces as contrast agents for OCT imaging.

Appendix

Technical Specifications

Thorlabs OCS1300SS Swept Source OCT System

Optical	
Central Wavelength	1325 nm
Spectral Bandwidth	100 nm
Axial Scan Rate	16 kHz
Coherence length	6.0 mm
Average Output Power	10.0 mW
Data Acquisition	
A/D Conversion Rate	100 MS/s
A/D Resolution	14-bit
A/D Channels	2
Analog Output Rate	1 MS/s
Analog Output Resolution	16 bit
Analog Output Channels	4
Imaging	
2D Cross SEctional OCT Imaging Capability	
Imaging Speed (on 512 A-scans Per Frame)	25 fps
Maximum Imaging Size (H x D)	4000 x 512 pixels
Maximun Imaging Width	10 mm
Maximum Imaging Depth	3.0 mm
Transverse Resolution	15 µm
Axial Resolution (Air/Water)	12/9 µm
2D *en-face* Microscope Imaging Capability	
CCD Camera Pixel	3.0 Mega, 24 Bit RGB
Maximum Resolution Pixel	1600 x 1200
Imaging Speed	100fps @ 640 x 480 pixels; 20fps @ 1600 x 1200
3D Volumetric Imaging Capability	
Maximum Valume Size (L x W x D)	10 mm x 10 mm x 3 mm
Maximum Sampling Resolution (L x W x D)	640 x 640 x 512 pixels
Imaging Time	~30 seconds
General	
Supply Voltage for Swept Source Engine	100-240 VAC 50/60 Hz
Supply Voltage for Imaging Module	±15 VDC
Supply Voltage for computer	115/230 VAC 50/60 Hz
Storage/Operating Temperature	10 to 40 °C
Dimensions of probe stand (L x W x H)	206 mm x 305 mm x 240mm
Dimensions of swept source (L x W X H	320 mm x 270 mm x 150mm
Dimensions of imaging module (L x W x H)	320 mm x 270mm x 65mm
Dimensions of computer (L x W x H)	445 mm x 445 mm x 19mm

Thorlabs OCS1300SS Swept Source OCT System Operating Manual page 8